Efficient and accurate extraction of full-wave equivalent circuit for printed circuit structures

Chua, Eng Kee

2007

Chua, E. K. (2007). Efficient and accurate extraction of full-wave equivalent circuit for printed circuit structures. Doctoral thesis, Nanyang Technological University, Singapore.

https://hdl.handle.net/10356/3457

https://doi.org/10.32657/10356/3457

NANYANG TECHNOLOGICAL UNIVERSITY

EFFICIENT AND ACCURATE EXTRACTION OF FULL-WAVE EQUIVALENT CIRCUIT FOR PRINTED CIRCUIT STRUCTURES

CHUA ENG KEE

SCHOOL OF ELECTRICAL AND ELECTRONIC ENGINEERING

2007

Efficient and Accurate Extraction of Full-Wave Equivalent Circuit for Printed Circuit Structures

Chua Eng Kee

School of Electrical and Electronic Engineering

A thesis submitted to the Nanyang Technological University
in fulfilment of the requirement for the degree of
Doctor of Philosophy

2007

ACKNOWLEDGMENTS

The work presented in this thesis has been carried out under the supervision of Dr. See Kye Yak, Associate Professor of Circuits and System Division, School of Electrical and Electronic Engineering, Nanyang Technological University, Singapore. I wish to express my sincere appreciation to him for his guidance and encouragement during the course of the research work.

I would like to thank Mr. Manish Oswal and Mr. Richard Chang Weng Yew for their assistance in the collecting the measurement data. I also like to thank Mr. Tan Keng Hong, Mr. Wee Seng Khoon and Mdm. Koh Guek Hwa, the technical staff of Electronic Lab II, for their laboratory support.

Financial support from Agency for Science, Technology and Research (A*STAR) is gratefully acknowledged. I must also thank Dr. Li Er Ping, Senior Manager of Electronics and Software Applications, Institute of High Performance Computing, for his understanding and patience while I was writing up my thesis.

Last but not least, I would like to express my deepest appreciation to my family for their love and support.

SUMMARY

Due to the ever-increasing clock speeds of electronic devices, PCB layouts of high-speed digital circuits become very challenging due to electromagnetic interference (EMI) and signal integrity (SI) design issues. The purpose of PCB is to provide the necessary signal and power interconnections for the digital integrated circuit mounted on board. Without due diligence in PCB layout, the electronic device could malfunction due to poor SI design and worst still, it could fail the maximum allowable radiated emission limit specified by the mandatory EMI regulation.

The way that the interconnecting traces laid on a PCB plays a crucial role on meeting the SI and EMI design requirements. Hence, accurate electrical models of these traces are needed for pre-design simulation so as to identify potential SI and EMI problems. As the operating frequency reaches GHz range, conventional electrical models for printed circuit interconnects are no longer accurate enough for SI and EMI prediction. Hence, the need for a full-wave electrical model for any arbitrary printed circuit is apparent.

Based on full-wave modelling approach, this thesis presents an accurate and efficient algorithm that is capable of extracting the full-wave electrical model of any arbitrary printed circuit structure. The extracted electrical model is compatible with any SPICE-based simulation tool. The full-wave electrical model allows electronic engineers to

perform SI and EMI analyses of specific PCB layout using the familiar SPICE-based design tools without another set of electromagnetic simulation tool.

Table of Contents

LIST OF FIGURES

LIST OF TABLES

LIST OF ACRONYMS

2D — 2-Dimension

3D — 3-Dimension

Bi-CG — Bi-Conjugate Gradient

Bi-CGSTAB — Bi-Conjugate Gradient Stable

CG — Conjugate Gradient

CGS — Conjugate Gradient Square

CISPR — Comité International Spécial des Perturbations Radioélectriques (French) or International Special Committee on Radio Interference (English)

CM — Common-Mode

DM — Differential-Mode

EDA — Electronic Design Automation

EFIE — Electric Field Integral Equation

EM — Electromagnetic

EMC — Electromagnetic Compatibility

EMI — Electromagnetic Interference

Emax — maximum electric field

FCC — Federal Communications Commission, USA

FDTD — Finite-Difference Time-Domain

FEM — Finite Element Method

FVTD — Finite-Volume Time-Domain

GMRES — Generalized Minimal Residual

HFSS — High Frequency Structural Simulator

IT — Information Technology

MoM — Method of Moments

$O(n^2)$ — Order of n^2

PCB — Printed Circuit Board

PEC — Perfect Electric Conductor

PEEC — Partial Element Equivalent Circuits

RF — Radio Frequency

SI — Signal Integrity

SMA — SubMiniature version A

SMT — Surface Mount Technology

SPD — Symmetric Positive Definite

SPICE — Simulation Program for Integrated Circuit Emulation

TEM — Transverse Electric and Magnetic

USA — United States of America

CHAPTER ONE

1 INTRODUCTION

1.1 Importance of EMI/SI Analysis for PCBs

The electronic industries have grown very rapidly because of the introduction of transistors in the early sixties. Since then, the variety of electronic equipment increases rapidly. With heavy usage of consumer electronics in the home and office, electromagnetic interference (EMI) from one device to another becomes a problem to the user [1]. Nowadays, almost all consumer electronics rely heavily on digital techniques to implement various controls and functions. Unfortunately, without proper design consideration, consumer electronics that adopt digital technique could pose potential EMI threat to other electronic systems [2]–[6]. To achieve electromagnetic compatibility (EMC) amongst these electronic systems, the victim system shall be hardened to withstand a higher level of EMI and the culprit system shall be properly designed such that it emits a low level of EMI. There are two basic routes that EMI can reach the victim equipment. One route is through the conduction via cables and the other route is through the electromagnetic wave propagation through air, or commonly known as radiation in the EMC community.

To ensure that radiated emissions from an electronic product are kept under control, the international regulatory bodies have enforced mandatory radiated EMI limits for

different categories of electronic products. For example, information technology (IT) products, such as notebook computer or PDA, shall meet FCC Part 15 Subpart B Class B limits for USA market and EN55022 Class B limits for European market [7]–[8]. The maximum allowable radiated EMI limits are very stringent and pose design challenges to the electronic product designers.

In almost all electronic and telecommunications' products, the electronic circuits are laid on the printed circuit boards (PCBs). For the past decade, a lot of research efforts have been put in to study the impacts of PCB layouts on radiated EMI. A few literatures have shown that a poor layout of high-speed digital circuits on a PCB results in significant level of radiated EMI [2]–[6]. In most cases, an electronic product could hardly comply with the regulatory EMI limits if the PCB layout is not taken into consideration at the product design and development stages. Therefore, good PCB layout practice is essential to control the level of radiated EMI from an electronic product.

In general, the radiation mechanism of a PCB is either differential-mode (DM) [9]–[10] or common-mode (CM) in nature [10]–[25]. The major sources of the DM radiation are the circuit loops formed by the power-ground paths and the signal-ground paths routed on the PCB. Since the circuit loops formed by these power-ground and signal-ground paths are well defined, careful layout to minimize the loop areas could easily reduce DM radiation [4]. One of the major sources of CM radiation is the CM current on the interfacing cables attached to the PCB. Although the ground noise voltages on the PCB are thought to be the major source of the CM current [9], two fundamental source

mechanisms are identified and are denoted as voltage-driven and current-driven mechanisms [11]–[13].

As radiated EMI problems at the PCB level are usually dominated by radiation from interfacing cables and printed circuit interconnections, an in-depth study of the mechanism and characteristics of radiation becomes necessary so that effective EMI corrective measures could be implemented during the design stage.

Signal integrity (SI) is another issue associated with high-speed digital design, which is also sensitive to the layout of interconnecting tracks on PCB. Although design techniques to meet SI and EMC objectives are often the same, the magnitude levels can be vastly different. EMC often deals with magnitude level of microvolt/microampere, and SI often deals with magnitude level of millivolt/milliampere. Even a few microamperes are sufficient to cause EMI failures. Furthermore, EMC addresses problems as a whole system while SI focuses problems on the PCB [26]–[29].

SI on PCB primarily involves the electrical performance of the conducting traces on the PCB for propagating digital signals between integrated circuits. SI problem arises whenever the signal begins to lose its integrity. The main sources of signal distortion are:

- ringing – an unwanted oscillation of a voltage or current due to impedance mismatch;

- crosstalk – undesired coupling, either inductively or capacitively from one circuit to another; usually occurs when two closely laid parallel conducting traces cause two cross-coupled magnetic fields to interact with each other;
- ground bounce – phenomenon occurs when a transistor switches from one state to another (it causes the ground voltage to bounce up and down) [30]–[40].

Most SI problems can be avoided through good layout techniques, these techniques will ensure the circuits to work within the design specifications. In the past when board size is not a constraint, impedance control with large ground plane is easily achievable. Nowadays, the consumer electronics market has driven the engineers to package all electronics components on much smaller PCB. Due to board size constraint, large patch of ground plane is often impossible for very compact design. To make thing worse, interconnects are often routed from one circuit to another through via to another layer of the PCB, to via again and then back to the original layer. Such a complicated routing will reduce the signal quality further. These PCB design constraints pose greater challenges for electronics engineers to design product with good SI performance. Hence, thorough SI analysis for high-speed circuit is often done for critical signal path to ensure signal quality is acceptable. Hence, SI analysis before actual PCB layout serves to identify potential signal degradation problem for high-speed PCBs.

1.2 Motivation

The latest generation of microprocessors operate at clock speeds well exceeding 3 GHz. The bus speeds of these latest ranges of microprocessors can be as high as 1 GHz. To

communicate with external peripherals, the address and data buses are used as the media to connect the microprocessor to the peripherals on a motherboard. These address and data buses, which will contribute to the so-called differential-mode (DM) radiation, are finally terminated near the edge of the motherboard in the forms of sockets or connectors. External data cables are then connected to different peripherals through these sockets or connectors. These attached data cables serve as unintentional antennas and generate the so-called common-mode (CM) radiation. With bus speed hitting 1 GHz, the digital circuit interconnects [41]–[43] have become the bottleneck of high-speed digital design. Without proper design consideration, electrically long interconnect deteriorates the signal quality and restricts the maximum operating frequency of the digital circuits. Furthermore, the signal quality for address and data buses for electrically long interconnect suffers further due to trace-to-trace crosstalk.

Conventionally, circuit designers modelled interconnects as simple lumped RC model for low frequency and extended to distributed RLCG circuit model for high frequency [44]–[46]. The RLCG transmission line model has been used extensively for long and straight interconnects. For interconnects with bends or uneven separations, they can be modelled as cascade multi-port networks, and usually characterized in terms of scattering parameter (s-parameter) at the input and output ports [47]–[48]. The multi-port model can be obtained through full-wave modelling or by measurement approach [49]–[50]. Two-port network usually provides the voltages (or currents) at both ends of the port. For simplicity, the electrical model based on two-port network assumes the reference conductor (or usually referred to as ground) to be ideally with zero potential and lumped all the non-ideal effects on the signal conductor for modelling and analysis purposes. However, in reality, both signal and reference conductors are non-ideal and

how the behaviour of reference or ground conductor affects EMI and SI could provide useful insight how the printed circuit interconnects should be routed on a PCB. Commercial EM simulation tools could easily extract the s-parameters of interconnects, but useful information on the effects of the ground conductor is usually not readily available. For example, for a pair of long interconnecting traces (one for signal and the other for reference), in two-port analysis, the voltage drop on the signal delivery path (including both signal and ground conductors) is usually lumped into the signal conductor and the return conductor is assumed to be ideal conductor with zero voltage drop. If only the voltages and currents at both ends of interconnects are of interest, the two-port network is perfectly fine from the modelling point of view. However, in SI and EMI analyses, ground bounce (high-speed switching noise voltage across the ground conductor) provides insightful information from the circuit design perspective. Hence, an electrical model that has the ability to predict ground bounce of any printed circuit interconnects is very useful as it allows the designers to avoid SI and EMI problems before the actual PCB fabrication. Such an electrical model has to be "full-wave" in nature so that all the coupling effects between traces could be included to provide prediction result with reasonable accuracy.

Most commercially available full-wave electromagnetic simulation codes are using either finite element method (FEM) [51]–[52], , finite-difference time-domain (FDTD) method [53]–[54], finite-volume time-domain (FVTD) method [55]–[56] or method of moments (MoM) [57]–[58]. These tools usually perform full-wave simulation for interconnects and finally exporting interconnects as a two-port network and characterizes them in terms of s-matrix. As mentioned earlier, the two-port model was unable to provide the ground bounce information. Hence, a full-wave equivalent circuit

extraction algorithm for any arbitrary printed circuit interconnects will be useful. Unlike RF designers, electronics circuit designers still prefer circuit-based simulation tool. Therefore, the extracted full-wave equivalent circuit model must be SPICE-compatible so that it could be imported to any SPICE-based simulation tool for ground bounce, SI and radiated emission analyses.

Circuit modelling based on full-wave approach is not new and has a long history. The partial element equivalent circuit (PEEC) method was first introduced by Ruehli [59] based on the quasi-static approach. It was later improved further using the full-wave approach and renamed as retarded partial element equivalent circuit (rPEEC) method [60], where the effect of retardation was included in the model as delay source. Further developments on PEEC were documented in [61]–[68]. However, the number of circuit elements to model a large structure using PEEC can be computational prohibitive.

Hence, the motivation of this thesis is to extract SPICE-compatible equivalent circuit that is full-wave in nature, easy to implement and reasonably computational efficient. There are a couple of differences between the proposed approach and the PEEC. Firstly, the PEEC uses step approximation for the currents and the charges, i.e. the basis functions for both currents and charges are pulse functions. As the current distribution is based on step-approximation, much finer grid size (usually $< \lambda/20$, where λ is the wavelength concerned) is needed to achieve convergence and good accuracy. The proposed approach has already included continuity equation between the currents and charges in its electric field integral formulation. Because of the differential operator in the continuity equation, the current basis function must be a piecewise linear functions in order to achieve continuous and smooth current distribution on the printed circuit

structure. The triangular basis functions are selected for this purpose, results in very good numerical convergence and solution accuracy even the grid size is as large as λ/5. Secondly, the PEEC will always have self-capacitance at every circuit node with respect to a fictitious observation point of zero potential, which usually refers to infinite distance from the circuit node. The proposed approach eliminates the need of these self-capacitances in the circuit model. Only node-to-node mutual capacitances exist in the model and it eliminates the need of the fictitious zero potential point. With some manipulation to the circuit model, a reduced equivalent circuit model is resulted, which retains the "full-wave" accuracy with much lesser circuit elements.

1.3 Objective and Contributions of the Thesis

The objective of this thesis is to develop an algorithm that allows extraction of full-wave equivalent circuit for any printed circuit structure with well-defined geometry. The extracted model can be easily integrated to any SPICE-based simulation platform so that any EMI and SI related design issues due to the PCB layout can be simulated and investigated before the actual board fabrication.

The major contributions of this thesis are as follows:

- Successful development of an extraction algorithm based on Method of Moments (MoM) full-wave modelling approach capable of extracting full-wave equivalent circuit of any arbitrary printed circuit interconnects with defined geometry and dimensions.

- Accurate and fast computation of the matrix elements in the MoM formulation based on approximated analytical expressions for the selected basis functions used in the full-wave formulation, which makes the extraction process highly efficient even for large equivalent circuit.

- Demonstration of the extracted full-wave equivalent circuit in predicting ground bounce as well as CM radiation for any printed circuit structure, which allows the designers to gain useful insights on the rationales behind some good PCB layout design practices.

1.4 Organisation of the Thesis

The thesis is organised into the following chapters:

This chapter has explained the importance of EMI/SI study for PCBs in high-speed applications. The motivation, objective and contributions of the thesis are also discussed.

Chapter 2 describes in details the methodology on the circuit parameters extraction algorithm. It starts with the field equivalence theorem, where printed circuit structure can be replaced with the currents on conductor and within the substrate. Enforcing the necessary boundary conditions, Electric Field Integral Equations (EFIEs) are established. Based on the MoM technique, an impedance matrix is formed. The matrix consists of impedances due to the vector magnetic field and scalar electric field

components. An algorithm is derived to extract the partial inductances from the vector magnetic field component and node-to-node capacitances from the scalar electric field component. The capacitance extraction procedure is further improved so that the number of capacitances needed for a full-wave equivalent model is reduced to its minimum and yet retain the model accuracy.

Chapter 3 presents an efficient and accurate method to evaluate the impedance elements in the MoM matrix. By expanding the Green's function into Taylor's series, an approximated analytical expression of the integration of the Green's function can be obtained. Four different kinds of integrations are necessary to compute the elements of in the MoM matrix; the surface integration of 2D pulse basis function, triple integration of 2D triangular basis function, volume integration of 3D pulse basis function and quadruple integration of 3D triangular basis function. Different expressions are derived for each kind of integration, depending on the distance between the source and observation points.

Chapter 4 validates the extracted full-wave electrical model and demonstrates its applications in SI and EMI analyses.

Chapter 5 concludes the thesis and recommends future work to further improve the extraction algorithm.

CHAPTER TWO

2 FULL-WAVE EQUIVALENT CIRCUIT EXTRACTION

The most common approaches in electromagnetic simulation codes for solving PCB problems are FEM, FDTD, FVTD or MoM. Each of these methods has its own strengths and weaknesses. Hence, the selection of a particular method is very much problem-dependent. Since the problems to be solved in this thesis include radiated EMI from the PCB, the MoM is a good choice as it requires no further treatment for open boundary problems, such as EMI radiation from PCB. Also, most EMI problems are analysed in the frequency-domain, which is also another reason for choosing the MoM approach for our extraction algorithm.

Traditionally, the needs of the microwave and the RF design communities have driven the development of PCB full-wave modelling for filter and antenna designs. Usually, the MoM full-wave formulations for printed circuit structures are based on an infinite stratified media approach. Such an approach uses the exact version of Green's function for an infinite layered media and solves for the currents on the printed circuit conductors only [69]–[75]. Although it is computational efficient, it has the inherent inability to model realistic 3D finite-size printed circuit structures, where the common-mode phenomenon due to asymmetry of printed circuit structure cannot be included. The proposed MoM formulation in the thesis has the flexibility to model both finite-

size substrate and conductor of a 3D printed circuit [76]–[77]. Of course, it pays a price for additional equations to be formulated and extra computational effort. However, such a formulation is necessary if a truly "full-wave" equivalent circuit model for a printed circuit structure is needed. The additional effort results in direct extraction of a full-wave and SPICE-compatible equivalent circuit model for any arbitrary printed circuit structure with a given geometry and defined dimension.

This Chapter will discuss on the method to extract SPICE-compatible full-wave equivalent circuit model for any arbitrary printed circuit structure. Firstly, it starts with a full-wave formulation of a PCB, which results in a set of electric field integral equations (EFIEs) that described all the full-wave couplings of the PCB. Based on the EFIEs, the procedure to extract a comprehensive full-wave equivalent circuit model of any arbitrary printed circuit structure is described in details. For practicality issue, a simplified full-wave circuit model that retains the accuracy of the comprehensive model is introduced. Next, the procedure to compute the RF voltage drop between any two points on the conductor is explained. Finally, this chapter ends with a conclusion.

2.1 The Formulation of EFIEs

For a typical PCB, the thickness of the conductor is in the order of 0.025 to 0.05 mm where the substrate's thickness is around 0.8 to 1.6 mm. Hence, the thickness of conductor is much smaller than that of substrate. Therefore, the conductor will be approximated as perfect electric conductor (PEC) with zero thickness as compared to the substrate. Also, the substrate used in PCB is homogeneous with a defined dielectric constant.

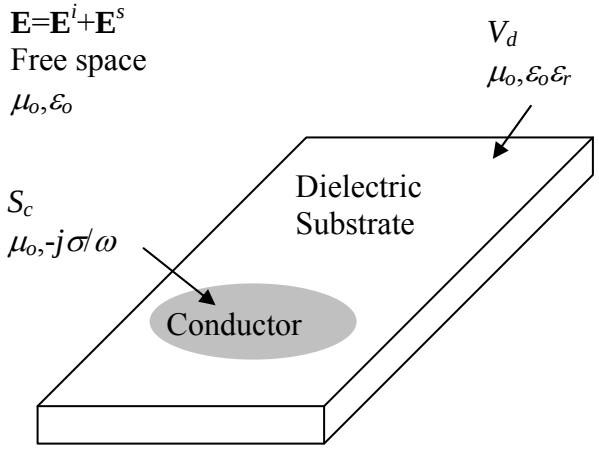

Fig. 2.1 Finite-size printed circuit structure

Under the influence of an incident electric field $\mathbf{E}^i$, a PCB as shown in Fig. 2.1, causes a scattered electric field $\mathbf{E}^s$. Then, the resultant electric field $\mathbf{E}$ in free-space will be given as:

$$\mathbf{E} = \mathbf{E}^i + \mathbf{E}^s \tag{2.1}$$

By applying field equivalence theorem [78]–[79] , the conductor could be replaced by two-dimensional (2D) conduction current density radiating in free-space and the substrate could be replaced by three-dimensional (3D) polarisation current density also radiating in free-space. By taking the curl of the scattered field ($\mathbf{E}^s$,$\mathbf{H}^s$), it leads to:

$$\nabla \times \mathbf{E}^s = -\mathbf{K}_{eq} - j\omega\mu_o \mathbf{H}^s \tag{2.2}$$

$$\nabla \times \mathbf{H}^s = \mathbf{J}_{eq} + j\omega\varepsilon_o \mathbf{E}^s \tag{2.3}$$

where

$$\mathbf{K}_{eq} = j\omega\mu_o(\mu_r - 1)\mathbf{H} \tag{2.4}$$

$$\mathbf{J}_{eq} = j\omega\varepsilon_o(\varepsilon_r - 1)\mathbf{E} \tag{2.5}$$

Since PEC ($\sigma_c = \infty$) is assumed in the formulation, the tangential electric field E_{tan} on the 2D conductor will be zero. At the conductor/substrate boundary, the 2D surface charge density ρ_s is equal to the 3D normal electric flux density D_{norm} at the boundary. A typical conductor/substrate boundary of the PCB is shown in Fig. 2.2.

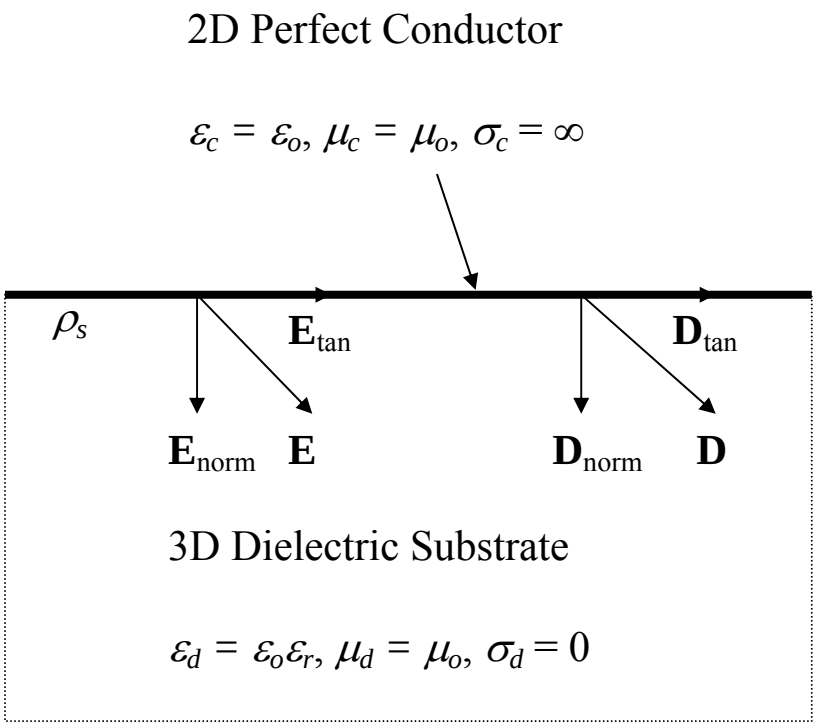

Fig. 2.2 Boundary of the conductor/substrate

Applying the boundary conditions at the conductor/substrate interface, the tangential electric field E_{tan} and normal electric fields E_{norm} are:

$$E_{tan} = 0 \tag{2.6}$$

$$E_{norm} = \frac{\rho_s}{\varepsilon_o \varepsilon_r} \tag{2.7}$$

The bound surface charge density ρ_b due to the polarisation effect is given by:

$$\rho_b = \varepsilon_o (\varepsilon_r - 1) E_{norm} \tag{2.8}$$

Through equation (2.8), the bound surface charge density ρ_b can be expressed as:

$$\rho_b = \frac{\mathbf{J}_{d,norm}}{j\omega} \tag{2.9}$$

Since the dielectric substrate is assumed to be homogeneous and lossless, the electric field **E** is related to the equivalence volume polarisation current $\mathbf{J}_d$ within the dielectric substrate, and from equation (2.5) it is given as:

$$\mathbf{J}_d = j\omega\varepsilon_o(\varepsilon_r - 1)\mathbf{E} \tag{2.10}$$

Applying equations (2.6)–(2.10) into equation (2.1), the incident electric field $\mathbf{E}^i$ can be expressed in terms of the scattered electric fields $\mathbf{E}_c^s(\mathbf{r})$ and $\mathbf{E}_d^s(\mathbf{r})$ as in equations (2.11) –(2.13) [77]:

$$\mathbf{E}^i(\mathbf{r})_{tan} = -\left[\mathbf{E}_c^s(\mathbf{r}) + \mathbf{E}_d^s(\mathbf{r})\right]_{tan}, \qquad \mathbf{r} \in S_c \tag{2.11}$$

$$\mathbf{E}^i(\mathbf{r}) = \frac{\mathbf{J}_d(\mathbf{r})}{j\omega\varepsilon_o(\varepsilon_r - 1)} - \left[\mathbf{E}_c^s(\mathbf{r}) + \mathbf{E}_d^s(\mathbf{r})\right], \qquad \mathbf{r} \in V_d \tag{2.12}$$

$$\mathbf{E}^i(\mathbf{r})_{norm} = \frac{\mathbf{J}_d(\mathbf{r})_{norm}}{j\omega\varepsilon_o(\varepsilon_r - 1)} - \left[\mathbf{E}_c^s(\mathbf{r}) + \mathbf{E}_d^s(\mathbf{r})\right]_{norm}, \qquad \mathbf{r} \in S_c \cap V_d \tag{2.13}$$

where

r – position vector of the observation point

$\mathbf{E}^i(\mathbf{r})_{tan}$ – incident tangential electric field on the 2D conducting surface

$\mathbf{E}^i(\mathbf{r})$ – incident electric field within the 3D substrate

$\mathbf{E}^i(\mathbf{r})_{norm}$ – incident normal electric field at the conductor/substrate boundary

$\mathbf{J}_d(\mathbf{r})$ – 3D normal polarisation current density within the substrate

$\mathbf{J}_d(\mathbf{r})_{norm}$ – 3D normal polarisation current density at the conductor/substrate boundary

E_{tan} – scalar tangential electric field at the conductor/substrate boundary

E_{norm} – scalar normal electric field at the conductor/substrate boundary

S_c – 2D area occupied by the conductor

V_d – 3D volume occupied by the substrate

$S_c \cap V_d$ – area common to conductor/substrate boundary

ω – angular frequency

ε_o – permittivity of free space

ε_r – relative permittivity of substrate

ρ_s – 2D surface charge density at the conductor/substrate boundary

The scattered electric fields $\mathbf{E}_c^s(\mathbf{r})$ and $\mathbf{E}_d^s(\mathbf{r})$ due to the conductor and the substrate, respectively, can be expressed in terms of their respective magnetic vector potentials and electric scalar potentials as follows:

$$\mathbf{E}_c^s(\mathbf{r}) = -j\omega\mathbf{A}_c(\mathbf{r}) - \nabla\phi_c(\mathbf{r}) \tag{2.14}$$

$$\mathbf{E}_d^s(\mathbf{r}) = -j\omega\mathbf{A}_d(\mathbf{r}) - \nabla\phi_d(\mathbf{r}) \tag{2.15}$$

The magnetic vector potentials and electric scalar potentials are given as:

$$\mathbf{A}_c(\mathbf{r}) = \mu_o \iint_{S_c} \mathbf{J}_c(\mathbf{r}')G(\mathbf{r};\mathbf{r}')ds' \tag{2.16}$$

$$\phi_c(\mathbf{r}) = \frac{1}{\varepsilon_o}\iint_{S_c} \rho_c(\mathbf{r}')G(\mathbf{r};\mathbf{r}')ds' \tag{2.17}$$

$$\mathbf{A}_d(\mathbf{r}) = \mu_o \iiint_{V_d} \mathbf{J}_d(\mathbf{r}')G(\mathbf{r};\mathbf{r}')dv' \tag{2.18}$$

$$\phi_d(\mathbf{r}) = \frac{1}{\varepsilon_o}\iiint_{V_d} \rho_d(\mathbf{r}')G(\mathbf{r};\mathbf{r}')dv' + \frac{1}{\varepsilon_o}\iint_{S_c \cap V_d} \rho_b(\mathbf{r}')G(\mathbf{r};\mathbf{r}')ds' \tag{2.19}$$

where

$\mathbf{J}_c(\mathbf{r}')$ – 2D conduction current density on the 2D conductor surface

$\mathbf{J}_d(\mathbf{r}')$ – 3D normal polarisation current density within the substrate

$\rho_c(\mathbf{r}')$ – 2D surface charge density associated with $\mathbf{J}_c(\mathbf{r}')$

$\rho_d(\mathbf{r}')$ – 3D volume charge density associated with $\mathbf{J}_d(\mathbf{r}')$

$\rho_b(\mathbf{r}')$ – bound charge density

Using the equation of continuity, the surface charge density at the conducting surface $\rho_c(\mathbf{r}')$ and volume charge density within the substrate $\rho_d(\mathbf{r}')$ can be expressed in terms of $\mathbf{J}_c(\mathbf{r}')$ and $\mathbf{J}_d(\mathbf{r}')$, respectively:

$$\rho_c(\mathbf{r}') = -\frac{\nabla' \cdot \mathbf{J}_c(\mathbf{r}')}{j\omega} \tag{2.20}$$

$$\rho_d(\mathbf{r}') = -\frac{\nabla' \cdot \mathbf{J}_d(\mathbf{r}')}{j\omega} \tag{2.21}$$

By combining equations (2.14), (2.16), (2.17) and (2.20), the scattered electric field $\mathbf{E}_c^s(\mathbf{r})$ due to the conductor can be expressed in terms of $\mathbf{J}_c(\mathbf{r}')$, and by combining equations (2.9), (2.15), (2.18), (2.19) and (2.21), the scattered electric field $\mathbf{E}_d^s(\mathbf{r})$ due to the substrate can be expressed in terms of $\mathbf{J}_d(\mathbf{r}')$ and $\mathbf{J}_d(\mathbf{r}')_{norm}$.

$$\mathbf{E}_c^s(\mathbf{r}) = -j\omega\mu_o \iint_{S_c} \mathbf{J}_c(\mathbf{r}')G(\mathbf{r};\mathbf{r}')ds' + \frac{\nabla}{j\omega\varepsilon_o}\iint_{S_c} \nabla'\cdot\mathbf{J}_c(\mathbf{r}')G(\mathbf{r};\mathbf{r}')ds' \tag{2.22}$$

$$\mathbf{E}_d^s(\mathbf{r}) = -j\omega\mu_o \iiint_{V_d} \mathbf{J}_d(\mathbf{r}')G(\mathbf{r};\mathbf{r}')dv' + \frac{\nabla}{j\omega\varepsilon_o}\iiint_{V_d} \nabla'\cdot\mathbf{J}_d(\mathbf{r}')G(\mathbf{r};\mathbf{r}')dv' + \frac{\nabla}{j\omega\varepsilon_o}\iint_{S_c\cap V_d} \mathbf{J}_d(\mathbf{r}')_{norm}G(\mathbf{r};\mathbf{r}')ds' \tag{2.23}$$

where

r' – position vector of the source point

$\mathbf{J}_c(\mathbf{r}')$ – 2D conduction current density on the 2D conductor surface

$\mathbf{J}_d(\mathbf{r}')$ – 3D polarisation current density within the substrate

μ_o – permeability of free space

μ_r – relative permeability of substrate

$G(\mathbf{r};\mathbf{r}')$ is the free-space Green's function and is given by:

$$G(\mathbf{r};\mathbf{r}') = \frac{e^{-jk_o|\mathbf{r}-\mathbf{r}'|}}{4\pi|\mathbf{r}-\mathbf{r}'|} \tag{2.24}$$

and the free-space wave number is given as

$$k_o = \omega\sqrt{\mu_o\varepsilon_o} \tag{2.25}$$

To simplify the mathematical expressions that follow, the linear operators $L[\ ]$ in terms of the current densities are defined as follows:

$$L\left[\mathbf{J}_c(\mathbf{r}')\right] = -j\omega\mu_o \iint_{S_c} \mathbf{J}_c(\mathbf{r}')G(\mathbf{r};\mathbf{r}')ds' + \frac{\nabla}{j\omega\varepsilon_o}\iint_{S_c} \nabla'\cdot\mathbf{J}_c(\mathbf{r}')G(\mathbf{r};\mathbf{r}')ds' \tag{2.26}$$

$$L\left[\mathbf{J}_d\left(\mathbf{r}'\right)\right] = -j\omega\mu_o \iiint_{V_d} \mathbf{J}_d\left(\mathbf{r}'\right) G\left(\mathbf{r};\mathbf{r}'\right) dv' + \frac{\nabla}{j\omega\varepsilon_o} \iiint_{V_d} \nabla' \cdot \mathbf{J}_d\left(\mathbf{r}'\right) G\left(\mathbf{r};\mathbf{r}'\right) dv' \tag{2.27}$$

$$L\left[\mathbf{J}_d\left(\mathbf{r}'\right)_{norm}\right] = \frac{\nabla}{j\omega\varepsilon_o} \iint_{S_c \cap V_d} \mathbf{J}_d\left(\mathbf{r}'\right)_{norm} G\left(\mathbf{r};\mathbf{r}'\right) ds' \tag{2.28}$$

where

L – linear operator

∇ – gradient operator

$\nabla' \cdot$ – divergence operator on the source function

Substitute equations (2.26)–(2.28) together with equations (2.22)–(2.23) into equations (2.11)–(2.13) results in:

$$\mathbf{E}^i(\mathbf{r})_{\tan} = -L\left[\mathbf{J}_c\left(\mathbf{r}'\right)\right] - L\left[\mathbf{J}_d\left(\mathbf{r}'\right)\right] - L\left[\mathbf{J}_d\left(\mathbf{r}'\right)_{norm}\right], \qquad \mathbf{r} \in S_c \tag{2.29}$$

$$\mathbf{E}^i(\mathbf{r}) = \frac{\mathbf{J}_d(\mathbf{r})}{j\omega\varepsilon_o\left(\varepsilon_r - 1\right)} - L\left[\mathbf{J}_c\left(\mathbf{r}'\right)\right] - L\left[\mathbf{J}_d\left(\mathbf{r}'\right)\right] - L\left[\mathbf{J}_d\left(\mathbf{r}'\right)_{norm}\right], \qquad \mathbf{r} \in V_d \tag{2.30}$$

$$\mathbf{E}^i(\mathbf{r})_{norm} = \frac{\mathbf{J}_d(\mathbf{r})_{norm}}{j\omega\varepsilon_o\left(\varepsilon_r - 1\right)} - L\left[\mathbf{J}_c\left(\mathbf{r}'\right)\right] - L\left[\mathbf{J}_d\left(\mathbf{r}'\right)\right] - L\left[\mathbf{J}_d\left(\mathbf{r}'\right)_{norm}\right], \quad \mathbf{r} \in S_c \cap V_d \tag{2.31}$$

Equations (2.29)–(2.31) are the so-called electrical field integral equations (EFIEs). These equations will be used to extract the full-wave equivalent circuit of PCB, which will be explained in subsequent sections.

2.2 Full-Wave Modelling Method

Depending the number of electrical elements to be extracted, the printed circuit structure is subdivided into smaller of subsections, as shown in Fig. 2.3. The size of each subsection is usually in the range of λ/5 to λ/20, where λ is the frequency of interest for the electrical model. By introducing a generalised *u*-*v*-*w* Cartesian coordinate system, the 2D conductor is subdivided into rectangular patches and the 3D substrate is sub-divided into rectangular cells, as shown in Fig. 2.3.

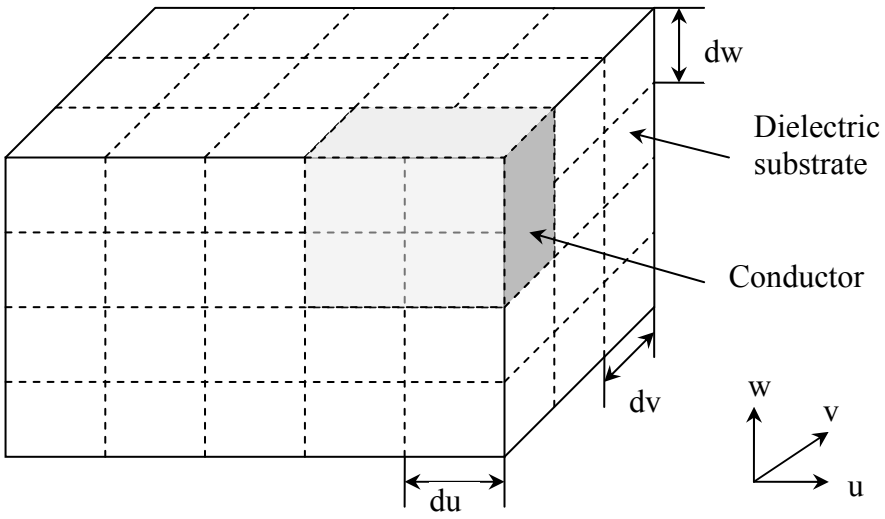

Fig. 2.3 Sub-divisions of a PCB

Once the structure is subdivided, some suitable basis functions have to be chosen to represent the current distributions on the conductor and within the substrate. In the extraction algorithm, 2D triangular functions and 3D triangular functions are chosen as the current basis functions for the current densities on the conductor and in the substrate, respectively. These functions are chosen to allow for the divergence operation of the

current density so that the current continuity between any two subsections could be maintained.

Two orthogonal vector components are required to describe the current density on a 2D conductor, e.g., a 2D conducting surface in the *u*-*v* plane requires *u*-directed as well as *v*-directed 2D triangular basis functions to fully describe the current density on that surface, as illustrated in Fig. 2.4 and Fig. 2.5, respectively.

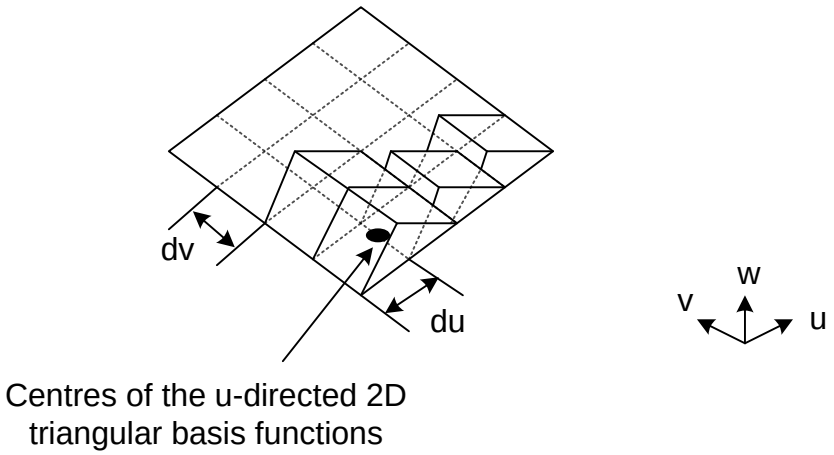

Fig. 2.4 *u*-directed 2D triangular functions lie on *u*-*v* plane

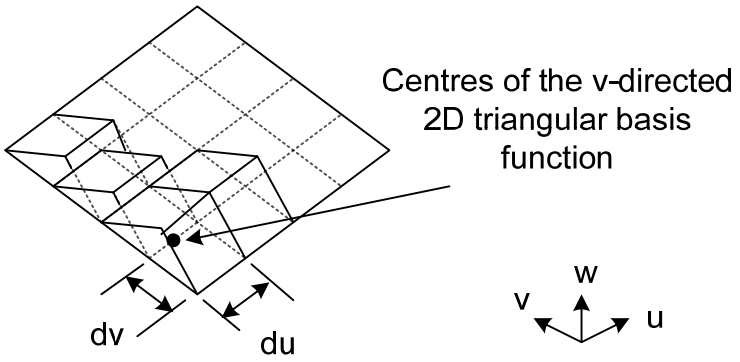

Fig. 2.5 *v*-directed 2D triangular functions lie on *u*-*v* plane

The full current expansion of the conductor surface current density on the *u*-*v* conducting plane is given by:

$$\mathbf{J}_c\left(\mathbf{r}'\right)_{u-v\,\text{plane}} = \frac{I^u_{\alpha_1}}{\Delta v}\Lambda^u_{\alpha_1}\left(\mathbf{r}'_{\alpha_1}\right)\hat{\mathbf{u}} + \frac{I^v_{\alpha_2}}{\Delta u}\Lambda^v_{\alpha_2}\left(\mathbf{r}'_{\alpha_2}\right)\hat{\mathbf{v}}, \qquad \mathbf{r}'_{\alpha_1}, \mathbf{r}'_{\alpha_2} \in S_c \tag{2.32}$$

where $I^u_{\alpha_1}$ and $I^v_{\alpha_2}$ are the unknown complex coefficients of the *u*-directed and *v*-directed 2D triangular current basis functions on the *u*-*v* plane, respectively; $\Lambda^u_{\alpha_1}\left(\mathbf{r}'_{\alpha_1}\right)$ and $\Lambda^v_{\alpha_2}\left(\mathbf{r}'_{\alpha_2}\right)$ are the *u*-directed and the *v*-directed 2D triangular current basis functions on the *u*-*v* conducting plane; (*u*',*v*',*w*') is the generalised Cartesian coordinate system for the source point. The mathematical expressions of these basis functions are as follows:

$$\Lambda^u_{\alpha_1}\left(\mathbf{r}'_{\alpha_1}\right) = \begin{cases} 1 - \dfrac{\left|u' - u'_{\alpha_1}\right|}{\Delta u}, & -\Delta u \le u' - u'_{\alpha_1} \le \Delta u, -\dfrac{\Delta v}{2} \le v' - v'_{\alpha_1} \le \dfrac{\Delta v}{2}, w' = w'_{\alpha_1} \\ 0, & \text{otherwise} \end{cases} \tag{2.33}$$

$$\Lambda^v_{\alpha_2}\left(\mathbf{r}'_{\alpha_2}\right) = \begin{cases} 1 - \dfrac{\left|v' - v'_{\alpha_2}\right|}{\Delta v}, & -\dfrac{\Delta u}{2} \le u' - u'_{\alpha_2} \le \dfrac{\Delta u}{2}, -\Delta v \le v' - v'_{\alpha_2} \le \Delta v, w' = w'_{\alpha_2} \\ 0, & \text{otherwise} \end{cases} \tag{2.34}$$

Each of these basis functions covers two rectangular patches, where $\mathbf{r}_{\alpha 1}$' and $\mathbf{r}_{\alpha 2}$' are the centres of the *u*-directed and *v*-directed 2D triangular current basis functions on the *u*-*v* plane, respectively.

To describe the current distribution within the 3D substrate, three vector components, *u*-directed, *v*-directed and *w*-directed 3D full-triangular functions, are required, as shown in Fig. 2.6. To handle the conductor/substrate boundary numerically, 3D half-

triangular functions (either rising or falling 3D half-triangular functions) will be used so that the normal component of polarization current in the substrate will be terminated with a surface charge density at the conductor/substrate boundary.

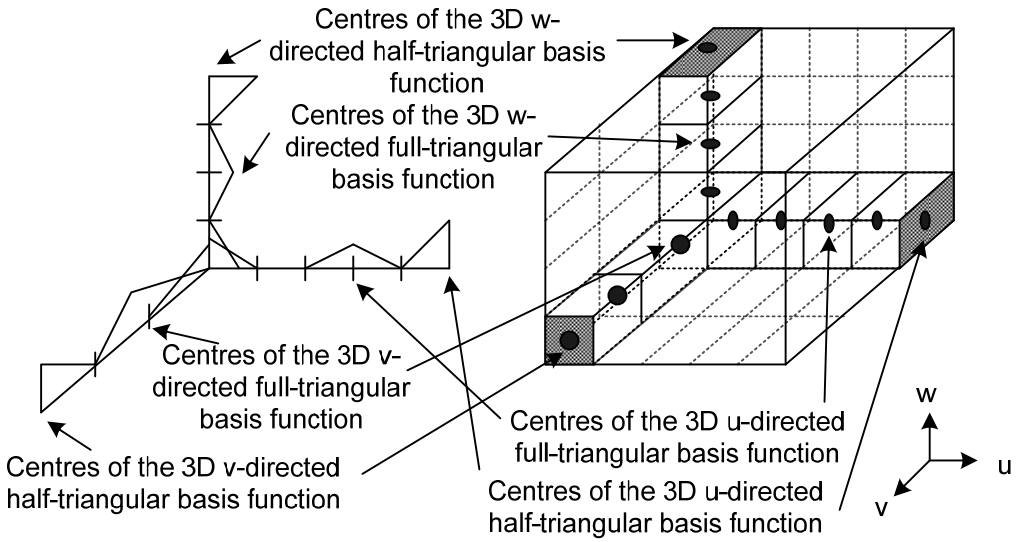

Fig. 2.6 3D full-triangular and half-triangular functions

The full current expansion of the volume polarisation current density within the dielectric substrate is given by:

$$\mathbf{J}_d\left(\mathbf{r}'\right)=\frac{I^u_{\beta_1}}{\Delta v\Delta w}\tau^u_{\beta_1}\left(\mathbf{r}'_{\beta_1}\right)\hat{\mathbf{u}}+\frac{I^v_{\beta_2}}{\Delta u\Delta w}\tau^v_{\beta_2}\left(\mathbf{r}'_{\beta_2}\right)\hat{\mathbf{v}}+\frac{I^w_{\beta_3}}{\Delta u\Delta v}\tau^w_{\beta_3}\left(\mathbf{r}'_{\beta_3}\right)\hat{\mathbf{w}},\qquad \mathbf{r}'_{\beta_1},\mathbf{r}'_{\beta_2},\mathbf{r}'_{\beta_3}\in V_d \quad (2.35)$$

where $\tau^u_{\beta_1}\left(\mathbf{r}'_{\beta_1}\right)$, $\tau^v_{\beta_2}\left(\mathbf{r}'_{\beta_2}\right)$ and $\tau^w_{\beta_3}\left(\mathbf{r}'_{\beta_3}\right)$ are the *u*-directed, *v*-directed and *w*-directed 3D triangular current basis function. The mathematical expressions of these functions are given as follows.

$$\tau_{\beta_1}^{u}\left(\mathbf{r}_{\beta_1}^{'}\right)=\begin{cases}1-\dfrac{\left|u^{'}-u_{\beta_1}^{'}\right|}{\Delta u}, & -\Delta u\le u^{'}-u_{\beta_1}^{'}\le\Delta u,-\dfrac{\Delta v}{2}\le v^{'}-v_{\beta_1}^{'}\le\dfrac{\Delta v}{2},\\ & -\dfrac{\Delta w}{2}\le w^{'}-w_{\beta_1}^{'}\le\dfrac{\Delta w}{2}\\ 0, & \text{otherwise}\end{cases} \tag{2.36}$$

$$\tau_{\beta_2}^{v}\left(\mathbf{r}_{\beta_2}^{'}\right)=\begin{cases}1-\dfrac{\left|v^{'}-v_{\beta_2}^{'}\right|}{\Delta v}, & -\dfrac{\Delta u}{2}\le u^{'}-u_{\beta_2}^{'}\le\dfrac{\Delta u}{2},-\Delta v\le v^{'}-v_{\beta_2}^{'}\le\Delta v,\\ & -\dfrac{\Delta w}{2}\le w^{'}-w_{\beta_2}^{'}\le\dfrac{\Delta w}{2}\\ 0, & \text{otherwise}\end{cases} \tag{2.37}$$

$$\tau_{\beta_3}^{w}\left(\mathbf{r}_{\beta_3}^{'}\right)=\begin{cases}1-\dfrac{\left|w^{'}-w_{\beta_3}^{'}\right|}{\Delta w}, & -\dfrac{\Delta u}{2}\le u^{'}-u_{\beta_3}^{'}\le\dfrac{\Delta u}{2},-\dfrac{\Delta v}{2}\le v^{'}-v_{\beta_3}^{'}\le\dfrac{\Delta v}{2},\\ & -\Delta w\le w^{'}-w_{\beta_3}^{'}\le\Delta w\\ 0, & \text{otherwise}\end{cases} \tag{2.38}$$

$\mathbf{r}_{\beta 1}'$, $\mathbf{r}_{\beta 2}'$ and $\mathbf{r}_{\beta 3}'$ are the centres of the *u*-directed, *v*-directed and *w*-directed 3D triangular current basis functions within the dielectric substrate, respectively. $I_{\beta 1}'$, $I_{\beta 2}'$ and $I_{\beta 3}'$ are the unknown complex coefficients of the *u*-directed, *v*-directed and *w*-directed 3D triangular current basis functions within the dielectric substrate, respectively

The full current expansion of the normal component of the volume polarisation current density at the conductor/dielectric boundary is given by:

$$\mathbf{J}_d\left(\mathbf{r}^{'}\right)_{norm}=\frac{I_{\gamma}^{u}}{\Delta v\Delta w}\eta_{\gamma}^{u}\left(\mathbf{r}_{\gamma}^{'}\right)\hat{\mathbf{u}}, \qquad \mathbf{r}_{\gamma}^{'}\in S_c\cap V_d \tag{2.39}$$

where $\eta_\gamma^u\left(\mathbf{r}_\gamma^{'}\right)$ is the u-directed 3D half-triangular current basis function

$$\eta_\gamma^u\left(\mathbf{r}_\gamma^{'}\right)=\begin{cases}1-\dfrac{\left|u^{'}-u_\gamma^{'}\right|}{\Delta u}, & -\Delta u\le u^{'}-u_\gamma^{'}\le 0,-\dfrac{\Delta v}{2}\le v^{'}-v_\gamma^{'}\le\dfrac{\Delta v}{2},\\ & -\dfrac{\Delta w}{2}\le w^{'}-w_\gamma^{'}\le\dfrac{\Delta w}{2}\\ 0, & \text{otherwise}\end{cases} \tag{2.40}$$

$\mathbf{r}_\gamma^{'}$ is the centre of the u-directed 3D half-triangular current basis functions at the conductor/dielectric boundary. $I_\gamma^{'}$ is the unknown complex coefficients of the u-directed 3D half-triangular current basis functions at the conductor/dielectric boundary.

The centres of all theses subdivided conducting patches and dielectric volume cells will be used as the circuit nodes of the extracted circuit elements as shown in Fig. 2.7.

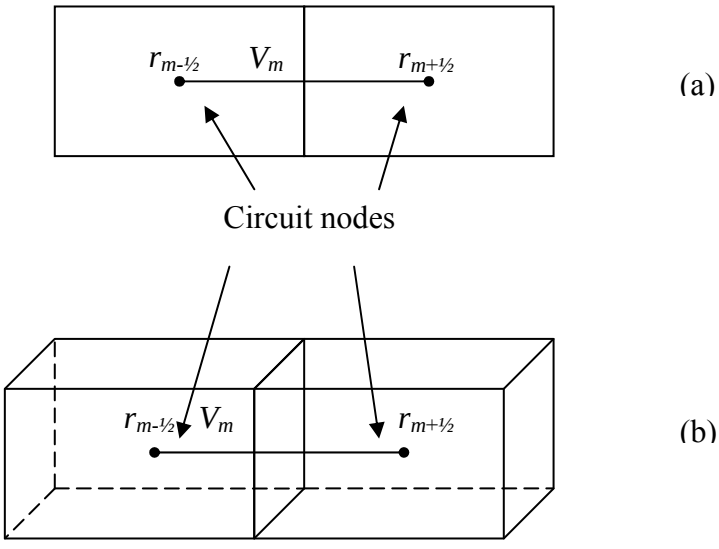

Fig. 2.7 (a) Two adjacent conducting patches
(b) Two adjacent dielectric volume cells

Based on the EFIEs derived previously, the voltage V_m between any two adjacent nodes due to a known incident electric field $\mathbf{E}^i$ can be determined by

$$V_m = -\int_{\mathbf{r}_{m-1/2}}^{\mathbf{r}_{m+1/2}} \mathbf{E}^i \cdot d\mathbf{l} \tag{2.41}$$

Substituting equations (2.11)–(2.13) into equation (2.41), the resulting equations can finally be expressed into the following matrix format.

$$[V] = \left(j\omega[L] - \frac{1}{j\omega}[Q] \right)[I] \tag{2.42}$$

where $[V]$ is an excitation voltage vector obtained from equation (2.41) and $[I]$ is the unknown current vector to be solved for. The matrix $[L]$ is resulted from the magnetic vector potential term in the EFIEs. It consists of partial self and mutual inductances $L_{m,\alpha}$ due to conductor current; and partial self and mutual inductances $L_{m,\beta}$ due substrate polarization current. These inductances can be calculated directly from:

$$L_{m,\alpha} = \frac{\mu_o}{\Delta v} \int_{\mathbf{r}_{m-1/2}}^{\mathbf{r}_{m+1/2}} \left[\iint_{S_c} \Lambda_\alpha^u(\mathbf{r}'_\alpha) G(\mathbf{r};\mathbf{r}'_\alpha) dS' \right] du \tag{2.43}$$

$$L_{m,\beta} = \frac{\mu_o}{\Delta v \Delta w} \int_{\mathbf{r}_{m-1/2}}^{\mathbf{r}_{m+1/2}} \left[\iiint_{V_d} \Omega_\beta^u(\mathbf{r}'_\beta) G(\mathbf{r};\mathbf{r}'_\beta) dV' \right] du \tag{2.44}$$

The matrix $[Q]$ is resulted from the electric scalar potential term in the EFIEs. For a given triangular current basis function, it results in a charge doublet because of the different operator in the current continuity equation.

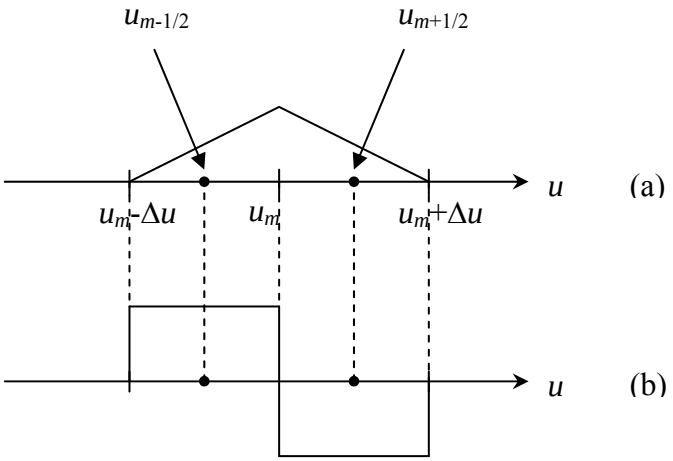

Fig. 2.8 (a) A u-directed triangular current basis function
(b) An associated charge pulse doublet

Hence, $Q_{m,\alpha}$ causes the electric scalar potential between adjacent nodes due to surface charge doublet on the conductor and $Q_{m,\beta}$ contributes to the electric scalar potential between adjacent nodes due to volume charge doublet within the substrate. They are given by

$$Q_{m,\alpha} = \frac{1}{\varepsilon_o \Delta u \Delta v} \int_{\mathbf{r}_{m-1/2}}^{\mathbf{r}_{m+1/2}} \nabla \left[\iint_{S_c} \nabla \cdot \Lambda_\alpha^u \left(\mathbf{r}_\alpha^{'}\right) G\left(\mathbf{r};\mathbf{r}_\alpha^{'}\right) dS^{'} \right] du \tag{2.45}$$

$$\begin{aligned} Q_{m,\beta} = & \frac{1}{\varepsilon_o \Delta u \Delta v \Delta w} \int_{\mathbf{r}_{m-1/2}}^{\mathbf{r}_{m+1/2}} \nabla \left[\iiint_{V_d} \nabla \cdot \Omega_\beta^u \left(\mathbf{r}_\beta^{'}\right) G\left(\mathbf{r};\mathbf{r}_\beta^{'}\right) dV^{'} \right] du \\ & + \frac{\nabla}{\varepsilon_o \Delta v \Delta w} \int_{\mathbf{r}_{m-1/2}}^{\mathbf{r}_{m+1/2}} \left[\iint_{S_c \cap V_d} \Omega_\beta^u \left(\mathbf{r}_\beta^{'}\right) G\left(\mathbf{r};\mathbf{r}_\beta^{'}\right) dS^{'} \right] du \end{aligned} \tag{2.46}$$

Unlike extracting the inductances, extracting the capacitances between any two circuit nodes, be they adjacent or non-adjacent, is not as straight forward and requires some further manipulation to the matrix [Q].

To illustrate the procedure to extract these inductances and capacitance, a simple structure consists of two parallel conductors, each of them 20 mm by 10 mm with a separation distance of 1 mm, as shown in Fig. 2.9, will be used for the explanation. The two parallel conductors are subdivided with equal rectangular patches of 10 mm by 10 mm. The centres of these four patches are circuit nodes labelled as 1, 2, 3, and 4; as indicated in Fig. 2.9. The self and mutual partial inductances of the two conductors are extracted directly from equation (2.43). The two self inductances are labelled as L_{11} and L_{22} and the mutual inductance is represented in terms of a coupling coefficient K_{12} (mutual coupling between L_{11} and L_{22}). For four circuit nodes, there are altogether six possible node-to-node capacitances, indicated as C_1, C_2, C_3, C_4, C_5 and C_6. These capacitances are due to the charges on the four patches resulting from the current flow.

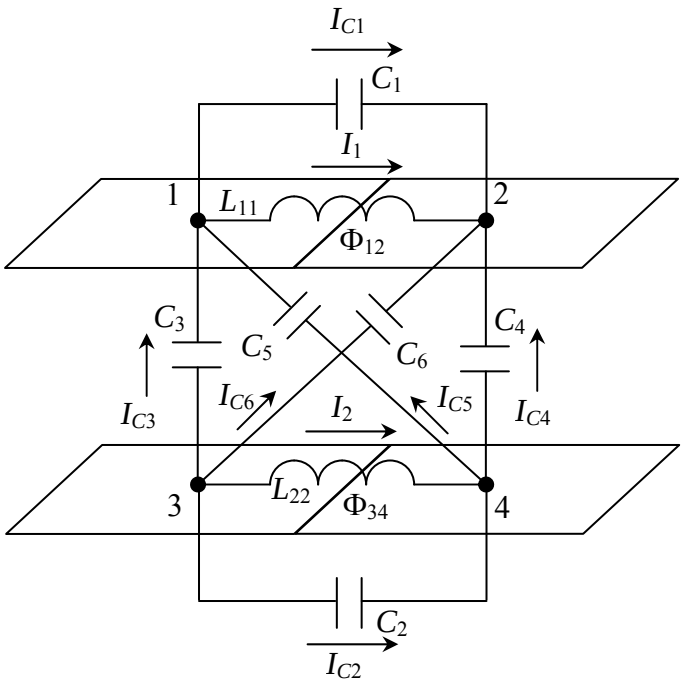

Fig. 2.9 A circuit model of parallel-plate

The two conductors in Fig. 2.9 have two unknown current I_1 and I_2. With known excitation voltage, they can be found by:

$$[I]=\left(j\omega[L]-\frac{1}{j\omega}[Q]\right)^{-1}[V] \tag{2.47}$$

Once the I_1 and I_2 are found, the charges due to I_1 and I_2 on the four patches can be easily obtained. Then, the electric scalar potentials between any two circuit nodes [Φ] can be computed from the known charges. The relationship between the capacitive currents and the electrical scalar potential are governed by:

$$[I_C]=[X_C][\Phi] \tag{2.48}$$

where

$$[I_C]=\begin{pmatrix} I_{C1} & I_{C2} & I_{C3} & I_{C4} & I_{C5} & I_{C6}\end{pmatrix}^T \tag{2.49}$$

$$[\Phi]=\begin{pmatrix} \Phi_{12} & \Phi_{34} & \Phi_{31} & \Phi_{42} & \Phi_{41} & \Phi_{32}\end{pmatrix}^T \tag{2.50}$$

$$[X_C]=\frac{1}{j\omega}\mathrm{Diag}\left(C_1,C_2,C_3,C_4,C_5,C_6\right) \tag{2.51}$$

and Diag(C_1,C_2,C_3,C_4,C_5,C_6) is the diagonal matrix that consists of the six node-to-node capacitances.

By applying Kirchhoff's current law at every node, it results in four equations. Rearranging these equations leads to:

$$[\alpha][I_C]=[\beta][I] \tag{2.52}$$

where matrices $[\alpha]$ and $[\beta]$, consist either 0, –1 or +1, depending on the directions of the currents in the inductances and capacitances at a specific node. For the case in Fig. 2.9,

$$[\alpha]=\begin{pmatrix} -1 & 0 & 1 & 0 & 1 & 0 \\ 1 & 0 & 0 & 1 & 0 & 1 \\ 0 & -1 & -1 & 0 & 0 & -1 \\ 0 & 1 & 0 & -1 & -1 & 0 \end{pmatrix} \tag{2.53}$$

$$[\beta]=\begin{pmatrix} -1 & 0 \\ 1 & 0 \\ 0 & -1 \\ 0 & 1 \end{pmatrix} \tag{2.54}$$

Since matrices $[\alpha]$, $[\beta]$ and $[I]$ are known, $[I_C]$ can be found easily through equation (2.52). Finally, $[X_C]$ is obtained by equation (2.48), which provides all the six node-to-node capacitances.

If now a 20 mm × 10 mm × 1 mm substrate with dielectric constant of 4.5 is added between the parallel conductors, as shown in Fig. 2.9, additional self inductances L_{d1} and L_{d2} due to the substrate polarization currents, and the mutual inductance between L_{d1} and L_{d2} can be calculated directly from equation (2.44). The mutual inductance can be represented with a coupling coefficient K_{d12}. In addition, the bound charges on the conductor due to the polarization current results in excess capacitances [61]–[62]. The bound charges can be found by the second term of equation (2.46). Once the bound charges are known, the excess capacitance due to substrate can be easily obtained. With the substrate, additional circuit elements are resulted. L_{d1} in series with C_{d1} and is added

between nodes 1 and 3; and L_{d2} in series with C_{d2} and is added between nodes 2 and 4, as shown in Fig. 2.10.

Table 2.1 lists all the circuit elements that constitute the full-wave equivalent model of Fig. 2.10. As the structure is symmetrical, $L_{11} = L_{22}$, $L_{d1} = L_{d2}$, $C_{d1} = C_{d2}$, $C_1 = C_2$, $C_3 = C_4$ and $C_5 = C_6$.

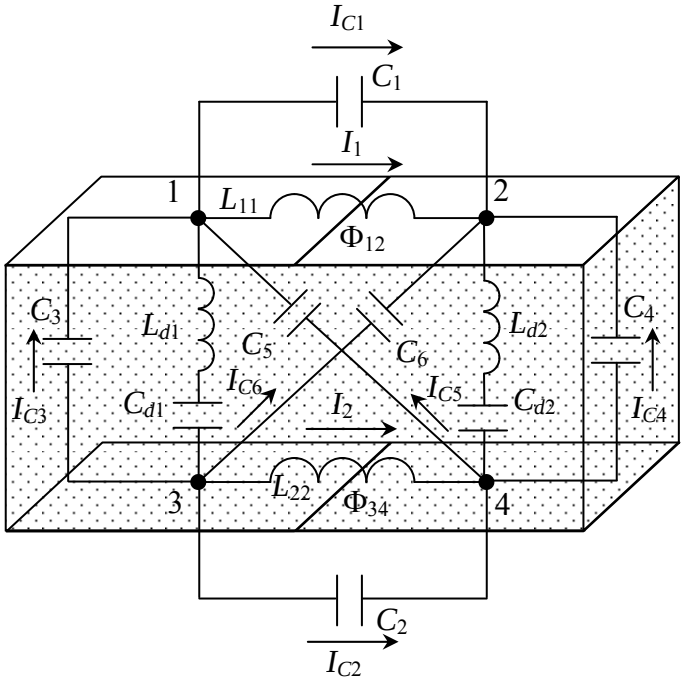

Fig. 2.10 A circuit model of parallel-plate PCB

Table 2.1 Full-wave circuit elements of Fig. 2.10

Circuit Element	Value
L_{11}	2.88479 nH
L_{22}	2.88479 nH
K_{12}	0.85238
L_{d1}	33.20902 pH
L_{d2}	33.20902 pH
K_{d12}	0.306361
C_1	54.3554 fF
C_2	54.3554 fF
C_3	930.078 fF
C_4	930.078 fF
C_5	30.2119 fF
C_6	30.2119 fF
C_{d1}	4.131865 pF
C_{d2}	4.131865 pF

As expected, the excess capacitances due to bound charges are much larger than the capacitances due to free charges (structure without substrate). Also, the inductances due to conductors are much higher than those resulted from the substrate. In conclusion, this section has shown the detailed algorithm to extract a comprehensive full-wave equivalent circuit model for any arbitrary printed circuit structure from the EFIEs derived from the previous section.

2.3 Simplified Full-Wave Circuit Model

To include all the circuit elements described in the previous section, it will run into the same problem faced by many existing full-wave extraction methods, where the model becomes computational prohibitive to solve for even for a moderate-sized structure. The major bottleneck is the involvement of a large number of capacitive elements in the comprehensive model. If the number of circuit nodes is N, it results in $N(N\text{-}1)/2$ capacitive elements. For example, 100 circuit nodes result in as many as 4950 capacitances. Hence, the full-wave equivalent model, though able to capture the "full-wave" effects, is impractical to be simulated in circuit simulation tool, such as SPICE. To overcome such a problem, this section will propose a simplified circuit model that still retains the full-wave accuracy, so that to make the proposed approach an attractive and viable option for SPICE-based modelling.

To simplify the equivalent circuit model, the easier way is to remove all the capacitances with insignificant values. The major shortcoming of this approach is that the comprehensive full-wave circuit model still has to be extracted first, which means that there is no computational advantage at all. Another approach is to retain those capacitances of significant values and then include full-wave coupling effects of the removed capacitances into the retained capacitances. This approach essentially simplifies the model and still preserves the accuracy of the comprehensive model. The procedure to extract such a simplified model is described as follows.

Using Fig. 2.9 again as an example, capacitances between nodes 1 and 3 and nodes 2 and 4 are to retain because of their values are most significant (their values are around

930 fF and the rest are less than 55 fF as given in Table 2.1). The larger values of the two capacitors C_3 and C_4 are expected as the separation distance between the parallel-plate is small. By removing C_1, C_2, C_5 and C_6, equation (2.48) can be modified into the following equation, where the subscript "*R*" denotes the reduced circuit model.

$$[I_{CR}] = [X_{CR}][\Phi_R] \tag{2.55}$$

where

$$[\Phi_R] = \begin{pmatrix} \Phi_{31} \\ \Phi_{42} \end{pmatrix} \qquad [I_{CR}] = \begin{pmatrix} I_{CR3} \\ I_{CR4} \end{pmatrix} \qquad [X_{CR}] = j\omega \begin{pmatrix} C_{R3} & 0 \\ 0 & C_{R4} \end{pmatrix}$$

Similarly, by applying Kirchhoff's current law at every node, it results in

$$[\alpha_R][I_{CR}] = [\beta][I] \tag{2.56}$$

where

$$[\alpha_R] = \begin{pmatrix} 1 & 0 & -1 & 0 \\ 0 & 1 & 0 & -1 \end{pmatrix}^T$$

Again, $[I_{CR}]$ can be obtained from equation (2.56) and $[X_{CR}]$ could be determined from equation (2.55).

Again, the printed circuit structure shown in Fig. 2.10 is used as an example. The resulting simplified model is given in Fig. 2.11. All the partial inductances remained and capacitances C_1, C_2, C_5 and C_6 are removed with their coupling effects included in C_3 and C_4, resulting in only two capacitances C_{R3} and C_{R4} in the simplified model. The values of all the elements in the simplified model are given in Table 2.2.

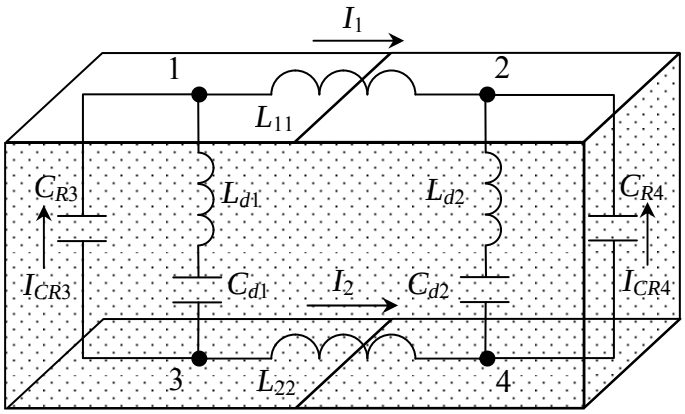

Fig. 2.11 A simplified circuit model of parallel-plate PCB

Table 2.2 Simplified full-wave circuit model

Circuit Element	Value
L_{11}	2.88479 nH
L_{22}	2.88479 nH
K_{12}	0.85238
L_{d1}	33.20902 pH
L_{d2}	33.20902 pH
K_{d12}	0.306361
C_{R3}	978.169 fF
C_{R4}	978.169 fF
C_{d1}	4.131865 pF
C_{d2}	4.131865 pF

Table 2.2 shows that C_{R3} and C_{R4} are larger than C_3 and C_4 in Table 2.2 as the coupling effects due to C_1, C_2, C_5 and C_6 have been distributed to C_{R3} and C_{R4}.

2.4 Calculation of RF Voltage Drop

The full-wave electrical model of a PCB has been described. This section illustrates how the RF voltage drop between any two points on the conductor can be predicted with good accuracy. Most designers have the misconception of voltage drop is due mainly to the resistance of the conductor. In fact, in high-speed operation, the voltage drop on conductor is contributed significantly by the inductance instead of resistance. In our formulation, since PEC is assumed, the voltage drop between any two adjacent nodes is simply the effect of inductive coupling. Under a know incident field (or know excitation voltage), the current on the conductor can be found based of procedure explained in the earlier section. Once the current is found, the voltage drops [Φ] between any two adjacent nodes on the conductor due to current [I] can be computed by:

$$[\Phi] = j\omega[L][I] \tag{2.57}$$

Once [Φ] are evaluated, the voltage drops between any two arbitrary nodes can be determined by using Kirchhoff's voltage law.

2.5 Conclusion

Based on full-wave treatment, the EFIEs for a printed circuit structure are formulated. The field quantities in the EFIEs are converted to circuit quantities so that a comprehensive full-wave circuit model for any arbitrary printed circuit structure can be extracted. With further modification, the comprehensive model is reduced to a simplified model. The simplified model allows simulation of EMI and SI problems in SPICE platform without excessive computational effort. The accuracy of the comprehensive model will be discussed in Chapter 4. By making full use of the extracted partial inductance matrix, the voltage drop between any two adjacent nodes on the conductor due to an excitation voltage can be evaluated, which will be very useful from the EMI and SI design perspective.

CHAPTER THREE

3 EFFICIENT AND ACCURATE EVALUATION OF INTEGRALS

In the previous chapter, the extraction algorithm of the full-wave equivalent circuit model of any printed circuit structure, based on the EFIEs, has been described. The accuracy of the extracted partial circuit elements, such as inductances and capacitances, to a large extent, is decided by how accurately the integrals of the various basis functions are evaluated. Also, the evaluation of these integrals must be computational efficient for obvious reason.

In any method of moments (MoM) full-wave formulation, depending on the selection of the basis functions and the test functions, the impedance matrix that consists of the circuit elements can be ill-conditioned [80]–[82]. As such, the overall accuracy of the extracted circuit elements depends very much on the accurate evaluation the integrals, especially the diagonal elements of the matrix. One common approach is to employ interpolation method [83]–[86]. It evaluates impedance matrices at a few selected frequencies and interpolates impedance matrices for the rest of frequencies. The improvement on the overall matrix-fill time depends on the number of simulation frequencies, which can be a several decades. However, the matrix-fill time for a single frequency still takes up substantial amount of time. Another approach is to apply the artificial neural networks (ANN) based model [87]–[88]. Its computational efficiency is

superior but suffers in solution's accuracy. Subsequently, a hybrid approach that combines neural networks and method of moments (NN-MoM) [89] is used to optimise both matrix-fill time and solution accuracy. It employs two trained radial basis function-neural networks (RBF-NN) to calculate majority of elements in the coupling matrix, the rest of elements are calculated using the conventional method. This approach provides better accuracy but has not improved matrix-fill time significantly. Some researchers use analytical simplification method [90]–[92] to reduce the impedance equation format from double integral to single integral. This approach effectively reduces the matrix-fill time but it is still not as efficient as the analytical approach for the evaluation of the impedance matrix elements [93]–[94]. The analytical approach eliminates the usage of numerical integrations. Hence, the matrix-fill time is greatly reduced.

In this thesis, a semi-analytical approach is adopted for the evaluation of the impedance matrix elements with the objectives of achieving both computational efficiency and sufficient solution's accuracy. To obtain semi-analytical expressions for matrix elements, one needs to know the specific basis and test functions. The choice of basis and test functions in the formulation of MoM matrix is very much dependent on the required accuracy and the ease of numerical implementation. Among all the commonly used basis and test functions, the triangular basis function and the pulse test function (line matching) are widely used because of their relative ease of implementation with reasonable solution's accuracy [95]–[98].

In the EFIEs formulated in Chapter 2, the 2D and 3D triangular basis functions with line matching are adopted for the calculation of the matrix elements. These basis functions and test functions lead to the needs of triple as well as quadruple integrations.

Firstly, either a double integration (surface integration) on the 2D source basis function or a triple integration (volume integration) on the 3D source basis function is carried out and then followed by a final integration along the test path between two circuit nodes. If all these integrations are carried out numerically, it will take up a substantial portion of the matrix-fill time. Also, the solution's accuracy depends very much on the resolution of the numerical integration. The double integration using analytical expression for triangular basis function has been reported [93]–[94]. However, the final integration along a test path is still carried out numerically using some well-establish integration algorithms. This chapter has proposed a semi-analytical expression that includes both the double/triple integration on the source basis function and the final integration along the test path. With this analytical expression, the calculation of matrix elements becomes highly efficient with superior accuracy.

In Chapter 2, it can be observed from equations (2.43)–(2.46) that the evaluations of the matrix elements require the following four kinds of integrations:

- Surface integration of the 2D pulse function that represents the charge on conductor;
- Surface integration of the 2D triangular basis function that represents the current on the conductor and followed by line integration along circuit nodes;

- Volume integration of the 3D pulse basis function that represents the volume charge within the substrate; and
- Volume integration of the 3D triangular basis function that represents the polarization current within the substrate and followed by line integration along circuit nodes.

The subsequent sections cover the derivations of semi-analytical expressions to evaluate the above-mentioned integrals.

3.1 Expansion of Free-Space Green's Function

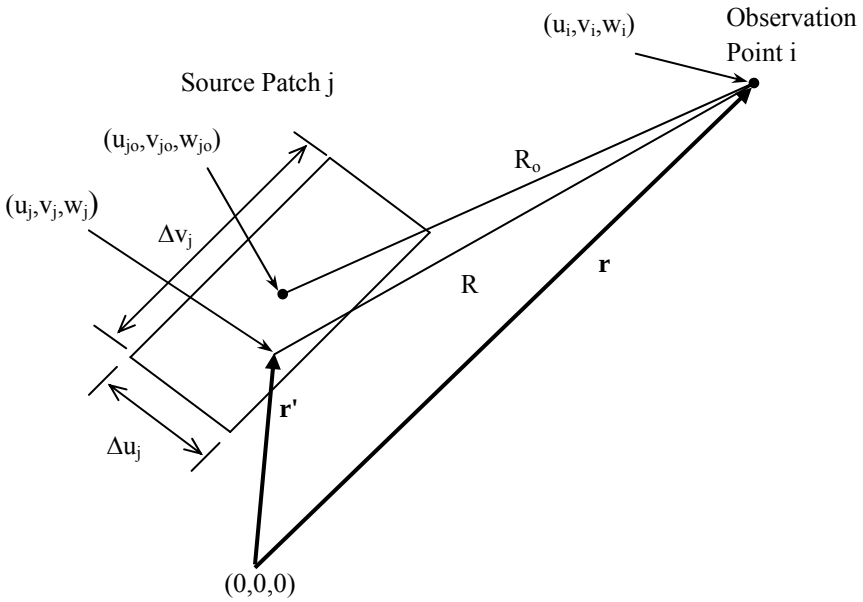

Fig. 3.1 Source region and test point

Fig. 3.1 shows a source patch where the current basis function is situated and an observation point, where $\mathbf{r}'$ and $\mathbf{r}$ are the position vectors for the source and observation points, respectively. The distance between the observation point (u_i,v_i,w_i) and source

point (u_j,v_j,w_j) is R, where $R = |\mathbf{r} - \mathbf{r}'|$. The distance between the observation point (u_i,v_i,w_i) and the centre of the source patch (u_{jo},v_{jo},w_{jo}) is R_o. Typically, the maximum grid size is less than 0.1λ, where λ is the wavelength of the frequency of interest. It can be observed from Fig. 3.1 that the maximum distance between the R and R_o occurs when (u_j,v_j,w_j) is at the far end corner of the source patch and both R and R_o lie on the same straight line. It can be calculated as follows:

$$\max|R - R_o| = \sqrt{(\Delta u_j/2)^2 + (\Delta v_j/2)^2} = 0.1/\sqrt{2}\,\lambda \tag{3.1}$$

where $\Delta u_j = \Delta v_j = 0.1\lambda$.

Now if the source region shown in Fig. 3.1 changes from source patch (2D) to source cell (3D) with additional sub-sectional variable Δw_j defining the thickness of the cell, the maximum distance between the R and R_o also occurs when (u_j,v_j,w_j) is at the far end corner of the source cell and both R and R_o lie on the same straight line. The maximum distance can be calculated using:

$$\max|R - R_o| = \sqrt{(\Delta u_j/2)^2 + (\Delta v_j/2)^2 + (\Delta w_j/2)^2} = 0.05\sqrt{3}\lambda \tag{3.2}$$

where $\Delta u_j = \Delta v_j = \Delta w_j = 0.1\lambda$.

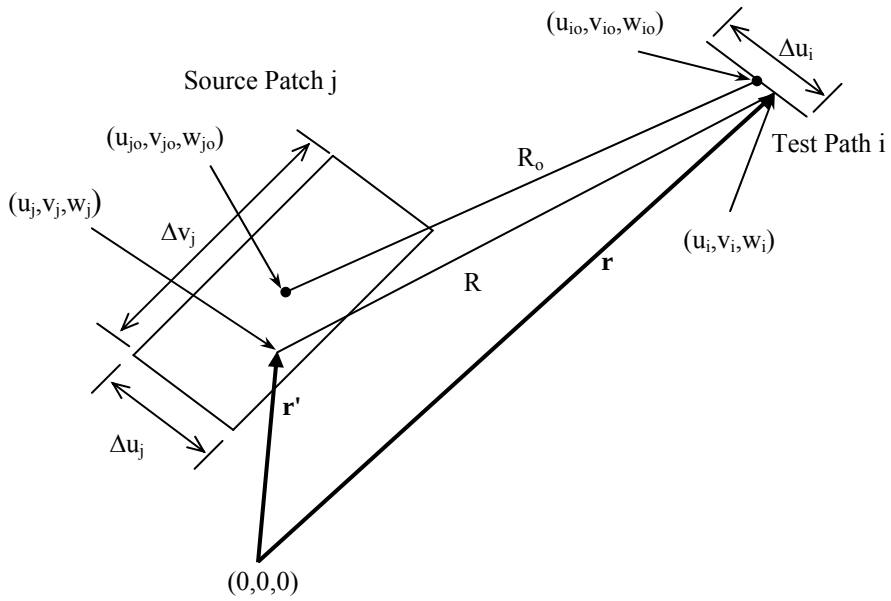

Fig. 3.2 Source region and test interval

Fig. 3.2 shows a source patch where the basis function is situated and an observation line path between two adjacent circuit nodes, where $\mathbf{r}'$ and $\mathbf{r}$ are the position vectors for the source and observation points, respectively. The distance between the observation point (u_i,v_i,w_i) and source point (u_j,v_j,w_j) is R, where $R = |\mathbf{r} - \mathbf{r}'|$. The distance between midpoint of the line path (u_{io},v_{io},w_{io}) and the centre of the source patch (u_{jo},v_{jo},w_{jo}) is R_o. It can be observed from Fig. 3.2 that the maximum distance between R and R_o occurs when both (u_{io},v_{io},w_{io}) and (u_{jo},v_{jo},w_{jo}) lie on the same point. This distance can be calculated by:

$$\max|R - R_o| = \sqrt{(\Delta u_j)^2 + (\Delta v_j/2)^2} = 0.05\sqrt{5}\lambda \tag{3.3}$$

where $\Delta u_i = \Delta u_j = \Delta v_j = 0.1\lambda$.

Similarly, if the source region shown in Fig. 3.2 changes from source patch (2D) to source cell (3D) with additional sub-sectional variable Δw_j defining the thickness of the

cell, the maximum distance between the R and R_o also occurs when (u_j,v_j,w_j) is at the centre of the source cell, calculated by:

$$\max|R - R_o| = \sqrt{(\Delta u_j)^2 + (\Delta v_j/2)^2 + (\Delta w_j/2)^2} = 0.1\sqrt{3/2}\lambda \tag{3.4}$$

where $\Delta u_j = \Delta v_j = \Delta w_j = 0.1\lambda$.

The radiated field due to the source basis function is governed by the free-space Green's function, $G(\mathbf{r};\mathbf{r}')$, given by:

$$G(\mathbf{r};\mathbf{r}') = \frac{e^{-jk_o R}}{4\pi R} \tag{3.5}$$

The free-space wave number is $k_o = \omega\sqrt{\mu_o\varepsilon_o}$. Direct integration of $G(\mathbf{r};\mathbf{r}')$ is not readily available. To obtain an analytical expression for the integration of $G(\mathbf{r};\mathbf{r}')$, the exponential term must be expanded in Taylor's series as follow.

$$\frac{e^{-jk_oR}}{R} = \frac{e^{-jk_oR_o}}{R}\left[1 - jk_o(R-R_o) - \frac{k_o^2(R-R_o)^2}{2!} + j\frac{k_o^3(R-R_o)^3}{3!} + \cdots\right] \tag{3.6}$$

The error bound of the series depends on the number of terms to be included in the calculation. The error bound of equation (3.6) up to n^{th} order can be obtained by $\text{error} \le k_o^{n+1}(R-R_o)^{n+1}/(n+1)!$. By assuming the maximum grid size for the structure in the modelling to be 0.1λ, Table 3.1 shows the error bound of equation (3.6) for the four different kind of integrations – surface integration of the 2D pulse basis function (2DΠ), triple integration of the 2D triangular basis function (2DΛ), volume integration of the 3D pulse basis function (3DΠ) and quadruple integration of the 3D triangular basis function (3DΛ) with various order, n.

Table 3.1 Error bound of equation (3.6)

Order *n*	Error of 2DΠ	Error of 3DΠ	Error of 2DΛ	Error of 3DΛ
0	44.4%	54.4%	70.2%	77.0%
1	9.87%	14.8%	24.7%	29.6%
2	1.46%	2.69%	5.78%	7.60%
3	0.162%	0.365%	1.01%	1.46%
4	0.0144%	0.0398%	0.143%	0.225%
5	0.00107%	0.00361%	0.0167%	0.0288%
6	0.0000678%	0.00028%	0.00167%	0.00317%

From Table 3.1, the worst error bound of equation (3.6) up to 5th order is 0.0288%. It is sufficiently accurate for most engineering problems and it is not worthwhile to include higher order terms beyond 5th. Hence, the series in equation (3.6) can now be truncated with good accuracy using:

$$\frac{e^{-jk_oR}}{R} \approx e^{-jk_oR_o}\left(\frac{\beta_0}{R} + \beta_1 + \beta_2 R + \beta_3 R^2 + \beta_4 R^3 + \beta_5 R^4\right) \tag{3.7}$$

The full expressions of the coefficients β_0 to β_5 are given below.

$$\begin{aligned}
\beta_0 &= 1 + jk_oR_o - \frac{k_o^2R_o^2}{2} - j\frac{k_o^3R_o^3}{6} + \frac{k_o^4R_o^4}{24} + j\frac{k_o^5R_o^5}{120} \\
\beta_1 &= -jk_o + k_o^2R_o + j\frac{k_o^3R_o^2}{2} - \frac{k_o^4R_o^3}{6} - j\frac{k_o^5R_o^4}{24} \\
\beta_2 &= -\frac{k_o^2}{2} - j\frac{k_o^3R_o}{2} + \frac{k_o^4R_o^2}{4} + j\frac{k_o^5R_o^3}{12} \\
\beta_3 &= j\frac{k_o^3}{6} - \frac{k_o^4R_o}{6} - j\frac{k_o^5R_o^2}{12} \\
\beta_4 &= \frac{k_o^4}{24} + j\frac{k_o^5R_o}{24} \\
\beta_5 &= -j\frac{k_o^5}{120}
\end{aligned} \tag{3.8}$$

With equation (3.7), analytical expression for the integration of $G(\mathbf{r};\mathbf{r}')$ is now possible since all the terms in equation (3.7) have closed form integrals.

3.2 Semi-Analytical Expressions for Integrals

For the four different kind of integrations mentioned earlier, six different integrals are needed. These are surface integration of 2D pulse function ($I_{2D\Pi}$), volume integration of 3D pulse function ($I_{3D\Pi}$), triple integration of rising 2D triangular function ($I_{2D\Lambda r}$), triple integration of falling 2D triangular function ($I_{2D\Lambda f}$), quadruple integration of rising 3D triangular function ($I_{3D\Lambda r}$) and quadruple integration of falling 3D triangular function ($I_{3D\Lambda f}$). Their mathematical expressions are given by:

$$I_{2D\Pi} = \frac{1}{4\pi}\int_{-\frac{\Delta v_j}{2}}^{\frac{\Delta v_j}{2}}\int_{-\frac{\Delta u_j}{2}}^{\frac{\Delta u_j}{2}}\frac{e^{-jk_oR}}{R}du_jdv_j \tag{3.9}$$

$$I_{3D\Pi} = \frac{1}{4\pi}\int_{-\frac{\Delta w_j}{2}}^{\frac{\Delta w_j}{2}}\int_{-\frac{\Delta v_j}{2}}^{\frac{\Delta v_j}{2}}\int_{-\frac{\Delta u_j}{2}}^{\frac{\Delta u_j}{2}}\frac{e^{-jk_oR}}{R}du_jdv_jdw_j \tag{3.10}$$

$$I_{2D\Lambda r} = \frac{1}{4\pi}\int_{-\frac{\Delta u_i}{2}}^{\frac{\Delta u_i}{2}}\int_{-\frac{\Delta v_j}{2}}^{\frac{\Delta v_j}{2}}\int_{-\frac{\Delta u_j}{2}}^{\frac{\Delta u_j}{2}}\frac{e^{-jk_oR}}{R}\left(\frac{1}{2}+\frac{u_j}{\Delta u_j}\right)du_jdv_jdu_i \tag{3.11}$$

$$I_{2D\Lambda f} = \frac{1}{4\pi}\int_{-\frac{\Delta u_i}{2}}^{\frac{\Delta u_i}{2}}\int_{-\frac{\Delta v_j}{2}}^{\frac{\Delta v_j}{2}}\int_{-\frac{\Delta u_j}{2}}^{\frac{\Delta u_j}{2}}\frac{e^{-jk_oR}}{R}\left(\frac{1}{2}-\frac{u_j}{\Delta u_j}\right)du_jdv_jdu_i \tag{3.12}$$

$$I_{3D\Lambda r} = \frac{1}{4\pi}\int_{-\frac{\Delta u_i}{2}}^{\frac{\Delta u_i}{2}}\int_{-\frac{\Delta w_j}{2}}^{\frac{\Delta w_j}{2}}\int_{-\frac{\Delta v_j}{2}}^{\frac{\Delta v_j}{2}}\int_{-\frac{\Delta u_j}{2}}^{\frac{\Delta u_j}{2}}\frac{e^{-jk_oR}}{R}\left(\frac{1}{2}+\frac{u_j}{\Delta u_j}\right)du_jdv_jdw_jdu_i \tag{3.13}$$

$$I_{3D\Lambda f} = \frac{1}{4\pi}\int_{-\frac{\Delta u_i}{2}}^{\frac{\Delta u_i}{2}}\int_{-\frac{\Delta w_j}{2}}^{\frac{\Delta w_j}{2}}\int_{-\frac{\Delta v_j}{2}}^{\frac{\Delta v_j}{2}}\int_{-\frac{\Delta u_j}{2}}^{\frac{\Delta u_j}{2}}\frac{e^{-jk_oR}}{R}\left(\frac{1}{2}-\frac{u_j}{\Delta u_j}\right)du_jdv_jdw_jdu_i \tag{3.14}$$

The semi-analytical expressions for the six integrals can be obtained by substituting equation (3.7) into equations (3.9)–(3.14):

$$I_{2D\Pi} \approx \frac{e^{-jk_oR_o}}{4\pi}\left(M_{2D\Pi,0}+M_{2D\Pi,1}+M_{2D\Pi,2}+M_{2D\Pi,3}+M_{2D\Pi,4}+M_{2D\Pi,5}\right) \tag{3.15}$$

$$I_{3D\Pi} \approx \frac{e^{-jk_oR_o}}{4\pi}\left(M_{3D\Pi,0}+M_{3D\Pi,1}+M_{3D\Pi,2}+M_{3D\Pi,3}+M_{3D\Pi,4}+M_{3D\Pi,5}\right) \tag{3.16}$$

$$I_{2D\Lambda r} \approx \frac{e^{-jk_oR_o}}{4\pi}\left(M_{2D\Lambda r,0}+M_{2D\Lambda r,1}+M_{2D\Lambda r,2}+M_{2D\Lambda r,3}+M_{2D\Lambda r,4}+M_{2D\Lambda r,5}\right) \tag{3.17}$$

$$I_{2D\Lambda f} \approx \frac{e^{-jk_oR_o}}{4\pi}\left(M_{2D\Lambda f,0}+M_{2D\Lambda f,1}+M_{2D\Lambda f,2}+M_{2D\Lambda f,3}+M_{2D\Lambda f,4}+M_{2D\Lambda f,5}\right) \tag{3.18}$$

$$I_{3D\Lambda r} \approx \frac{e^{-jk_oR_o}}{4\pi}\left(M_{3D\Lambda r,0}+M_{3D\Lambda r,1}+M_{3D\Lambda r,2}+M_{3D\Lambda r,3}+M_{3D\Lambda r,4}+M_{3D\Lambda r,5}\right) \tag{3.19}$$

$$I_{3D\Lambda f} \approx \frac{e^{-jk_oR_o}}{4\pi}\left(M_{3D\Lambda f,0}+M_{3D\Lambda f,1}+M_{3D\Lambda f,2}+M_{3D\Lambda f,3}+M_{3D\Lambda f,4}+M_{3D\Lambda f,5}\right) \tag{3.20}$$

where the various terms in equations (3.15)–(3.20) are defined as:

$$M_{2D\Pi,n} = \beta_n \int_{-\frac{\Delta v_j}{2}}^{\frac{\Delta v_j}{2}} \int_{-\frac{\Delta u_j}{2}}^{\frac{\Delta u_j}{2}} R^{n-1} du_j dv_j \tag{3.21}$$

$$M_{3D\Pi,n} = \beta_n \int_{-\frac{\Delta w_j}{2}}^{\frac{\Delta w_j}{2}} \int_{-\frac{\Delta v_j}{2}}^{\frac{\Delta v_j}{2}} \int_{-\frac{\Delta u_j}{2}}^{\frac{\Delta u_j}{2}} R^{n-1} du_j dv_j dw_j \tag{3.22}$$

$$M_{2D\Lambda r,n} = \beta_n \int_{-\frac{\Delta u_i}{2}}^{\frac{\Delta u_i}{2}} \int_{-\frac{\Delta v_j}{2}}^{\frac{\Delta v_j}{2}} \int_{-\frac{\Delta u_j}{2}}^{\frac{\Delta u_j}{2}} R^{n-1} \left(\frac{1}{2}+\frac{u_j}{\Delta u_j}\right) du_j dv_j du_i \tag{3.23}$$

$$M_{2D\Lambda f,n} = \beta_n \int_{-\frac{\Delta u_i}{2}}^{\frac{\Delta u_i}{2}} \int_{-\frac{\Delta v_j}{2}}^{\frac{\Delta v_j}{2}} \int_{-\frac{\Delta u_j}{2}}^{\frac{\Delta u_j}{2}} R^{n-1} \left(\frac{1}{2}-\frac{u_j}{\Delta u_j}\right) du_j dv_j du_i \tag{3.24}$$

$$M_{3D\Lambda r,n} = \beta_n \int_{-\frac{\Delta u_i}{2}}^{\frac{\Delta u_i}{2}} \int_{-\frac{\Delta w_j}{2}}^{\frac{\Delta w_j}{2}} \int_{-\frac{\Delta v_j}{2}}^{\frac{\Delta v_j}{2}} \int_{-\frac{\Delta u_j}{2}}^{\frac{\Delta u_j}{2}} R^{n-1} \left(\frac{1}{2}+\frac{u_j}{\Delta u_j}\right) du_j dv_j dw_j du_i \tag{3.25}$$

$$M_{3D\Lambda f,n} = \beta_n \int_{-\frac{\Delta u_i}{2}}^{\frac{\Delta u_i}{2}} \int_{-\frac{\Delta w_j}{2}}^{\frac{\Delta w_j}{2}} \int_{-\frac{\Delta v_j}{2}}^{\frac{\Delta v_j}{2}} \int_{-\frac{\Delta u_j}{2}}^{\frac{\Delta u_j}{2}} R^{n-1} \left(\frac{1}{2} - \frac{u_j}{\Delta u_j} \right) du_j dv_j dw_j du_i \tag{3.26}$$

The expressions for integrals up to 5th order for equations (3.21)–(3.26) are listed in Table 3.2–3.7, respectively.

Table 3.2 Integral expressions of equation (3.21)

Integral	Expression
$M_{2D\Pi,0}$	$\beta_0 g_{2D\Pi,0}$
$M_{2D\Pi,1}$	$\beta_1 \Delta u_j \Delta v_j$
$M_{2D\Pi,2}$	$\beta_2 g_{2D\Pi,1}$
$M_{2D\Pi,3}$	$\beta_3 \Delta u_j \Delta v_j \left[R_o^2 + \frac{(\Delta u_j)^2 + (\Delta v_j)^2}{12} \right]$
$M_{2D\Pi,4}$	$\beta_4 g_{2D\Pi,2}$
$M_{2D\Pi,5}$	$\beta_5 \Delta u_j \Delta v_j \left[R_o^4 + \frac{\Delta u_j^4 + \Delta v_j^4}{80} + \frac{\Delta u_j^2 \Delta v_j^2}{72} + \frac{R_o^2}{6}(\Delta u_j^2 + \Delta v_j^2) + \frac{u_o^2 \Delta u_j^2 + v_o^2 \Delta v_j^2}{3} \right]$

Table 3.3 Integral expressions of equation (3.22)

Integral	Expression
$M_{3D\Pi,0}$	$\beta_0 g_{3D\Pi,0}$
$M_{3D\Pi,1}$	$\beta_1 \Delta u_j \Delta v_j \Delta w_j$
$M_{3D\Pi,2}$	$\beta_2 g_{3D\Pi,1}$
$M_{3D\Pi,3}$	$\beta_3 \Delta u_j \Delta v_j \Delta w_j \left[R_o^2 + \frac{(\Delta u_j)^2 + (\Delta v_j)^2 + (\Delta w_j)^2}{12} \right]$
$M_{3D\Pi,4}$	$\beta_4 g_{3D\Pi,3}$
$M_{3D\Pi,5}$	$\beta_5 \Delta u_j \Delta v_j \Delta w_j \left[R_o^4 + \frac{R_o^2}{6}\left(\Delta u_j^2 + \Delta v_j^2 + \Delta w_j^2\right) + \frac{1}{3}\left(u_o^2 \Delta u_j^2 + v_o^2 \Delta v_j^2 + w_o^2 \Delta w_j^2\right) + \frac{1}{80}\left(\Delta u_j^4 + \Delta v_j^4 + \Delta w_j^4\right) + \frac{1}{72}\left(\Delta u_j^2 \Delta v_j^2 + \Delta u_j^2 \Delta w_j^2 + \Delta v_j^2 \Delta w_j^2\right) \right]$

Table 3.4 Integral expressions of equation (3.23)

Integral	Expression
$M_{2D\Lambda r,0}$	$\beta_0 g_{2D\Lambda r,0}$
$M_{2D\Lambda r,1}$	$\frac{\beta_1 \Delta u_i \Delta u_j \Delta v_j}{2}$
$M_{2D\Lambda r,2}$	$\beta_2 g_{2D\Lambda r,1}$
$M_{2D\Lambda r,3}$	$\frac{\beta_3 \Delta u_i \Delta u_j \Delta v_j}{2}\left[R_o^2+\frac{(\Delta u_i)^2+(\Delta u_j)^2+(\Delta v_j)^2}{12}-\frac{u_o \Delta u_j}{3}\right]$
$M_{2D\Lambda r,4}$	$\beta_4 g_{2D\Lambda r,2}$
$M_{2D\Lambda r,5}$	$\frac{\beta_5 \Delta u_i \Delta u_j \Delta v_j}{2}\left\{R_o^4+\frac{R_o^2}{6}\left(\Delta u_i^2+\Delta u_j^2+\Delta v_j^2\right)+\frac{\Delta u_i^4+\Delta u_j^4+\Delta v_j^4}{80}\right.$ $+\frac{1}{3}\left[u_o^2\left(\Delta u_i^2+\Delta u_j^2\right)+v_o^2 \Delta v_j^2\right]+\frac{1}{72}\left[3\Delta u_i^2 \Delta u_j^2+\Delta v_j^2\left(\Delta u_i^2+\Delta u_j^2\right)\right]$ $\left.-u_o \Delta u_j\left(\frac{2}{3}R_o^2+\frac{\Delta u_i^2}{6}+\frac{\Delta u_j^2}{10}+\frac{\Delta v_j^2}{18}\right)\right\}$

Table 3.5 Integral expressions of equation (3.24)

Integral	Expression
$M_{2D\Lambda f,0}$	$\beta_0 g_{2D\Lambda f,0}$
$M_{2D\Lambda f,1}$	$\dfrac{\beta_1 \Delta u_i \Delta u_j \Delta v_j}{2}$
$M_{2D\Lambda f,2}$	$\beta_2 g_{2D\Lambda f,1}$
$M_{2D\Lambda f,3}$	$\dfrac{\beta_3 \Delta u_i \Delta u_j \Delta v_j}{2}\left[R_o^2+\dfrac{(\Delta u_i)^2+(\Delta u_j)^2+(\Delta v_j)^2}{12}+\dfrac{u_o \Delta u_j}{3}\right]$
$M_{2D\Lambda f,4}$	$\beta_4 g_{2D\Lambda f,2}$
$M_{2D\Lambda f,5}$	$\dfrac{\beta_5 \Delta u_i \Delta u_j \Delta v_j}{2}\left\{R_o^4+\dfrac{R_o^2}{6}\left(\Delta u_i^2+\Delta u_j^2+\Delta v_j^2\right)+\dfrac{\Delta u_i^4+\Delta u_j^4+\Delta v_j^4}{80}\right.$ $+\dfrac{1}{3}\left[u_o^2\left(\Delta u_i^2+\Delta u_j^2\right)+v_o^2\Delta v_j^2\right]+\dfrac{1}{72}\left[3\Delta u_i^2\Delta u_j^2+\Delta v_j^2\left(\Delta u_i^2+\Delta u_j^2\right)\right]$ $\left.+u_o \Delta u_j\left(\dfrac{2}{3}R_o^2+\dfrac{\Delta u_i^2}{6}+\dfrac{\Delta u_j^2}{10}+\dfrac{\Delta v_j^2}{18}\right)\right\}$

Table 3.6 Integral expressions of equation (3.25)

Integral	Expression
$M_{3D\Delta r,0}$	$\beta_0 g_{3D\Delta r,0}$
$M_{3D\Delta r,1}$	$\dfrac{\beta_1 \Delta u_i \Delta u_j \Delta v_j \Delta w_j}{2}$
$M_{3D\Delta r,2}$	$\beta_2 g_{3D\Delta r,1}$
$M_{3D\Delta r,3}$	$\dfrac{\beta_3 \Delta u_i \Delta u_j \Delta v_j \Delta w_j}{2}\left[R_o^2+\dfrac{(\Delta u_i)^2+(\Delta u_j)^2+(\Delta v_j)^2+(\Delta w_j)^2}{12}-\dfrac{u_o \Delta u_j}{3}\right]$
$M_{3D\Delta r,4}$	$\beta_4 g_{3D\Delta r,2}$
$M_{3D\Delta r,5}$	$\dfrac{\beta_5 \Delta u_i \Delta u_j \Delta v_j \Delta w_j}{2}\left\{R_o^4+\dfrac{1}{80}\left(\Delta u_i^4+\Delta u_j^4+\Delta v_j^4+\Delta w_j^4\right)\right.$ $+\dfrac{R_o^2}{6}\left(\Delta u_i^2+\Delta u_j^2+\Delta v_j^2+\Delta w_j^2\right)+\dfrac{1}{3}\left[u_o^2\left(\Delta u_i^2+\Delta u_j^2\right)+v_o^2\Delta v_j^2+w_o^2\Delta w_j^2\right]$ $+\dfrac{1}{72}\left[\Delta u_i^2\left(3\Delta u_j^2+\Delta v_j^2+\Delta w_j^2\right)+\Delta u_j^2\left(\Delta v_j^2+\Delta w_j^2\right)+\Delta v_j^2\Delta w_j^2\right]$ $\left.-u_o \Delta u_j\left(\dfrac{2}{3}R_o^2+\dfrac{\Delta u_i^2}{6}+\dfrac{\Delta u_j^2}{10}+\dfrac{\Delta v_j^2+\Delta w_j^2}{18}\right)\right\}$

Table 3.7 Integral expressions of equation (3.26)

Integral	Expression
$M_{3D\Lambda f,0}$	$\beta_0 g_{3D\Lambda f,0}$
$M_{3D\Lambda f,1}$	$\frac{\beta_1 \Delta u_i \Delta u_j \Delta v_j \Delta w_j}{2}$
$M_{3D\Lambda f,2}$	$\beta_2 g_{3D\Lambda f,1}$
$M_{3D\Lambda f,3}$	$\frac{\beta_3 \Delta u_i \Delta u_j \Delta v_j \Delta w_j}{2}\left[R_o^2+\frac{(\Delta u_i)^2+(\Delta u_j)^2+(\Delta v_j)^2+(\Delta w_j)^2}{12}+\frac{u_o \Delta u_j}{3}\right]$
$M_{3D\Lambda f,4}$	$\beta_4 g_{3D\Lambda f,2}$
$M_{3D\Lambda f,5}$	$\frac{\beta_5 \Delta u_i \Delta u_j \Delta v_j \Delta w_j}{2}\left\{R_o^4+\frac{1}{80}\left(\Delta u_i^4+\Delta u_j^4+\Delta v_j^4+\Delta w_j^4\right)\right.$ $+\frac{R_o^2}{6}\left(\Delta u_i^2+\Delta u_j^2+\Delta v_j^2+\Delta w_j^2\right)+\frac{1}{3}\left[u_o^2\left(\Delta u_i^2+\Delta u_j^2\right)+v_o^2\Delta v_j^2+w_o^2\Delta w_j^2\right]$ $+\frac{1}{72}\left[\Delta u_i^2\left(3\Delta u_j^2+\Delta v_j^2+\Delta w_j^2\right)+\Delta u_j^2\left(\Delta v_j^2+\Delta w_j^2\right)+\Delta v_j^2\Delta w_j^2\right]$ $\left.+u_o\Delta u_j\left(\frac{2}{3}R_o^2+\frac{\Delta u_i^2}{6}+\frac{\Delta u_j^2}{10}+\frac{\Delta v_j^2+\Delta w_j^2}{18}\right)\right\}$

The full mathematical expressions of all the integral expressions listed in Table 3.2–Table 3.7 can be found in Appendix A.1.

3.3 Efficient Evaluation of Integrals Contained Subroutine Functions

A close observation reveals that the integral expressions of $M_{2D\Pi,0}$, $M_{2D\Pi,2}$, $M_{2D\Pi,4}$, $M_{3D\Pi,0}$, $M_{3D\Pi,2}$, $M_{3D\Pi,4}$, $M_{2D\Lambda r,0}$, $M_{2D\Lambda r,2}$, $M_{2D\Lambda r,4}$, $M_{2D\Lambda f,0}$, $M_{2D\Lambda f,2}$, $M_{2D\Lambda f,4}$, $M_{3D\Lambda r,0}$, $M_{3D\Lambda r,2}$, $M_{3D\Lambda r,4}$, $M_{3D\Lambda f,0}$, $M_{3D\Lambda f,2}$ and $M_{3D\Lambda f,4}$ consist of arctangent and logarithmic functions (full expressions are given in Appendix A.1). From the computational efficiency perspective, these functions should be avoided as much as possible, as they are subroutines in the computer program which require time to compute. As matrix size increases, the total time taken to compute all the matrix elements involving these functions can be substantial. To avoid the use of these functions, *1/R*, *R* and R^3 terms in $M_{2D\Pi,0}$, $M_{2D\Pi,2}$, $M_{2D\Pi,4}$, $M_{2D\Lambda r,0}$, $M_{2D\Lambda r,2}$, $M_{2D\Lambda r,4}$, $M_{2D\Lambda f,0}$, $M_{2D\Lambda f,2}$ and $M_{2D\Lambda f,4}$ are further expanded in terms of Taylor's series around R_o up to the 5th order:

$$a(u,v)=\frac{1}{R}\approx\sum_{m=0}^{5}\sum_{n=0}^{5-m}A_{mn}u^m v^n=\frac{1}{R_o}-\frac{u_o}{R_o^3}u-\frac{v_o}{R_o^3}v+\frac{3u_o v_o}{R_o^5}uv+\cdots \tag{3.27}$$

$$b(u,v)=R\approx\sum_{m=0}^{5}\sum_{n=0}^{5-m}B_{mn}u^m v^n=R_o+\frac{u_o}{R_o}u+\frac{v_o}{R_o}v-\frac{u_o v_o}{R_o^3}uv+\cdots \tag{3.28}$$

$$c(u,v)=R^3\approx\sum_{m=0}^{5}\sum_{n=0}^{5-m}C_{mn}u^m v^n=R_o^3+3u_o R_o u+3v_o R_o v+\frac{3u_o v_o}{R_o}uv+\cdots \tag{3.29}$$

where $R=\sqrt{(u_o+u)^2+(v_o+v)^2+w_o^2}$.

The coefficients A_{mn}, B_{mn} and C_{mn} are defined as follows:

$$A_{mn}=\frac{a^{(m,n)}(u_o,v_o)}{m!n!}\quad B_{mn}=\frac{b^{(m,n)}(u_o,v_o)}{m!n!}\quad C_{mn}=\frac{c^{(m,n)}(u_o,v_o)}{m!n!} \tag{3.30}$$

With equations (3.27)–(3.29), *1/R*, *R* and R^3 can now be easily integrated in using simple mathematical operation without involving the arctangent and logarithmic subroutines.

The only drawback of equations (3.27)–(3.29) is that they cannot be used when the distance between observation point and source point is approaching zero due to the singularity natures of equations (3.27)–(3.29). Through experiment, it is found that large error occurs when $R_o<\max(\Delta u_j,\Delta v_j)$. The error is nearly negligible when $R_o\geq 2\max(\Delta u_j,\Delta v_j)$ for integrals of 2DΠ ($M_{2D\Pi,0}$, $M_{2D\Pi,2}$ and $M_{2D\Pi,4}$), and $R_o\geq 2\max(\Delta u_j,\Delta v_j)+\Delta u_i$ for integrals of 2DΛ ($M_{2D\Lambda r,0}$, $M_{2D\Lambda r,2}$, $M_{2D\Lambda r,4}$, $M_{2D\Lambda f,0}$, $M_{2D\Lambda f,2}$ and $M_{2D\Lambda f,4}$). Hence, the use of Taylor's series expansions in equations (3.27)–(3.29) is restricted to $R_o\geq 2\max(\Delta u_j,\Delta v_j)$ for integrals of 2DΠ and $R_o\geq 2\max(\Delta u_j,\Delta v_j)+\Delta u_i$ for integrals of 2DΛ.

The limits of the two regions for 2DΠ and 2DΛ are defined in Table 3.8. For region I, the integration of *1/R*, *R* and R^3 function will have to be carried out with the usual arctangent and logarithmic functions. However, most of the matrix elements have satisfied the criterion of region II except the diagonal and near-diagonal matrix elements. For example if $\Delta u_i = \Delta u_j = \Delta v_j$ for integrals of 2DΛ, only the self-element, the adjacent elements and elements next to the adjacent elements (total nine elements) fall in region I, the rest of the elements fall in region II.

Table 3.8 Region definitions for 2DΠ and 2DΛ

	Region I	Region II
2DΠ	$R_o<2\max(\Delta u_j,\Delta v_j)$	$R_o\geq 2\max(\Delta u_j,\Delta v_j)$
2DΛ	$R_o<2\max(\Delta u_j,\Delta v_j)+\Delta u_i$	$R_o\geq 2\max(\Delta u_j,\Delta v_j)+\Delta u_i$

The expressions for $M_{2D\Pi,1}$, $M_{2D\Pi,3}$ and $M_{2D\Pi,5}$ are exactly the same for regions I and II. As for $M_{2D\Pi,0}$, $M_{2D\Pi,2}$ and $M_{2D\Pi,4}$, the expressions in region II are different. Since the expressions for $M_{2D\Pi,0}$, $M_{2D\Pi,2}$ and $M_{2D\Pi,4}$ are rather similar, only the expression for $M_{2D\Pi,0}$ is given in equation (3.31). The expression for $M_{2D\Pi,2}$ can be obtained by replacing all the coefficients of $M_{2D\Pi,0}$ from A_{mn} to B_{mn} and β_0 to β_2. Similarly, the expression for $M_{2D\Pi,4}$ can be obtained by replacing all the coefficients of $M_{2D\Pi,0}$ from A_{mn} to C_{mn} and β_0 to β_4.

$$M_{2D\Pi,0}=\beta_0\Delta u_j\Delta v_j\left[A_{00}+A_{20}\frac{(\Delta u_j)^2}{12}+A_{02}\frac{(\Delta v_j)^2}{12}+A_{22}\frac{(\Delta u_j)^2(\Delta v_j)^2}{144}+A_{40}\frac{(\Delta u_j)^4}{80}+A_{04}\frac{(\Delta v_j)^4}{80}\right] \tag{3.31}$$

Again, the expressions for $M_{2D\Lambda r,1}$, $M_{2D\Lambda r,3}$, $M_{2D\Lambda r,5}$, $M_{2D\Lambda f,1}$, $M_{2D\Lambda f,3}$ and $M_{2D\Lambda f,5}$ are exactly the same for regions I and II. As for $M_{2D\Lambda r,0}$, $M_{2D\Lambda r,2}$, $M_{2D\Lambda r,4}$, $M_{2D\Lambda f,0}$, $M_{2D\Lambda f,2}$ and $M_{2D\Lambda f,4}$ the expressions in region II are different. Since the expressions for $M_{2D\Lambda r,0}$, $M_{2D\Lambda r,2}$ and $M_{2D\Lambda r,4}$ are rather similar, only the expression for $M_{2D\Lambda r,0}$ is given in equation (3.32); the expressions for $M_{2D\Lambda f,0}$, $M_{2D\Lambda f,2}$ and $M_{2D\Lambda f,4}$ are also similar, only the expression for $M_{2D\Lambda f,0}$ is given in equation (3.33). The expressions for $M_{2D\Lambda r,2}$ and $M_{2D\Lambda f,2}$ can be obtained by replacing all the coefficients of $M_{2D\Lambda r,0}$ and $M_{2D\Lambda f,0}$, respectively, from A_{mn} to B_{mn} and β_0 to β_2. Similarly, the expression for $M_{2D\Lambda r,4}$ and

$M_{2D\Lambda f,4}$ can be obtained by replacing all the coefficients of $M_{2D\Lambda r,0}$ and $M_{2D\Lambda f,0}$, respectively, from A_{mn} to C_{mn} and β_0 to β_4.

$$\begin{aligned} M_{2D\Lambda r,0} &= \frac{\beta_0 \Delta u_i \Delta u_j \Delta v_j}{2}\left\{A_{00} + \left[A_{20} + A_{22}\frac{(\Delta v_j)^2}{12}\right]\frac{(\Delta u_i)^2 + (\Delta u_j)^2}{12} + A_{02}\frac{(\Delta v_j)^2}{12}\right. \\ &\left. + A_{40}\left[\frac{(\Delta u_i)^4 + (\Delta u_j)^4}{80} + \frac{(\Delta u_i)^2(\Delta u_j)^2}{24}\right] + A_{04}\frac{(\Delta v_j)^4}{80}\right\} \\ &- \frac{\beta_0 \Delta u_i (\Delta u_j)^2 \Delta v_j}{4}\left\{\frac{A_{10}}{3} + \left[A_{30} + A_{32}\frac{(\Delta v_j)^2}{12}\right]\left[\frac{(\Delta u_i)^2}{12} + \frac{(\Delta u_j)^2}{20}\right] + A_{12}\frac{(\Delta v_j)^2}{36}\right. \\ &\left. + A_{14}\frac{(\Delta v_j)^4}{240} + A_{50}\left[\frac{(\Delta u_i)^4}{48} + \frac{(\Delta u_j)^4}{112} + \frac{(\Delta u_i)^2(\Delta u_j)^2}{24}\right]\right\} \end{aligned} \tag{3.32}$$

$$\begin{aligned} M_{2D\Lambda f,0} &= \frac{\beta_0 \Delta u_i \Delta u_j \Delta v_j}{2}\left\{A_{00} + \left[A_{20} + A_{22}\frac{(\Delta v_j)^2}{12}\right]\frac{(\Delta u_i)^2 + (\Delta u_j)^2}{12} + A_{02}\frac{(\Delta v_j)^2}{12}\right. \\ &\left. + A_{40}\left[\frac{(\Delta u_i)^4 + (\Delta u_j)^4}{80} + \frac{(\Delta u_i)^2(\Delta u_j)^2}{24}\right] + A_{04}\frac{(\Delta v_j)^4}{80}\right\} \\ &+ \frac{\beta_0 \Delta u_i (\Delta u_j)^2 \Delta v_j}{4}\left\{\frac{A_{10}}{3} + \left[A_{30} + A_{32}\frac{(\Delta v_j)^2}{12}\right]\left[\frac{(\Delta u_i)^2}{12} + \frac{(\Delta u_j)^2}{20}\right] + A_{12}\frac{(\Delta v_j)^2}{36}\right. \\ &\left. + A_{14}\frac{(\Delta v_j)^4}{240} + A_{50}\left[\frac{(\Delta u_i)^4}{48} + \frac{(\Delta u_j)^4}{112} + \frac{(\Delta u_i)^2(\Delta u_j)^2}{24}\right]\right\} \end{aligned} \tag{3.33}$$

To avoid arctangent and logarithmic functions, $1/R$, R and R^3 in $M_{3D\Pi,0}$, $M_{3D\Pi,2}$, $M_{3D\Pi,4}$, $M_{3D\Lambda r,0}$, $M_{3D\Lambda r,2}$, $M_{3D\Lambda r,4}$, $M_{3D\Lambda f,0}$, $M_{3D\Lambda f,2}$ and $M_{3D\Lambda f,4}$, respectively, are further expanded in terms of Taylor's series around R_o up to the 5th order:

$$\begin{aligned} a(u,v,w) = \frac{1}{R} &\approx \sum_{m=0}^{5}\sum_{n=0}^{5-m}\sum_{p=0}^{5-m-n} A_{mnp} u^m v^n w^p = \frac{1}{R_o} - \frac{u_o}{R_o^3}u - \frac{v_o}{R_o^3}v - \frac{w_o}{R_o^3}w \\ &+ \frac{3u_o v_o}{R_o^5}uv + \frac{3u_o w_o}{R_o^5}uw + \frac{3v_o w_o}{R_o^5}vw - \frac{15u_o v_o w_o}{R_o^7}uvw + \cdots \end{aligned} \tag{3.34}$$

$$b(u,v,w) = R \approx \sum_{m=0}^{5}\sum_{n=0}^{5-m}\sum_{p=0}^{5-m-n} B_{mnp}u^m v^n w^p = R_o + \frac{u_o}{R_o}u + \frac{v_o}{R_o}v + \frac{w_o}{R_o}w - \frac{u_o v_o}{R_o^3}uv - \frac{u_o w_o}{R_o^3}uw - \frac{v_o w_o}{R_o^3}vw + \frac{3u_o v_o w_o}{R_o^5}uvw + \cdots \quad (3.35)$$

$$c(u,v,w) = R^3 \approx \sum_{m=0}^{5}\sum_{n=0}^{5-m}\sum_{p=0}^{5-m-n} C_{mnp}u^m v^n w^p = R_o^3 + 3u_o R_o u + 3v_o R_o v + 3w_o R_o w + \frac{3u_o v_o}{R_o}uv + \frac{3u_o w_o}{R_o}uw + \frac{3v_o w_o}{R_o}vw - \frac{3u_o v_o w_o}{R_o^3}uvw + \cdots \quad (3.36)$$

where $R = \sqrt{(u_o+u)^2 + (v_o+v)^2 + (w_o+w)^2}$.

The coefficients A_{mnp}, B_{mnp} and C_{mnp} are defined as follows:

$$A_{mnp} = \frac{a^{(m,n,p)}(u_o, v_o, w_o)}{m!\,n!\,p!} \quad B_{mnp} = \frac{b^{(m,n,p)}(u_o, v_o, w_o)}{m!\,n!\,p!} \quad C_{mnp} = \frac{c^{(m,n,p)}(u_o, v_o, w_o)}{m!\,n!\,p!} \quad (3.37)$$

With equations (3.34)–(3.36), *1/R*, *R* and R^3 can now be easily integrated efficiently. The limits of the two regions for 3DΠ and 3DΛ are defined in Table 3.9.

Table 3.9 Region definitions for 3DΠ and 3DΛ

	Region I	Region II
3DΠ	R_o<2max(Δu_j,Δv_j,Δw_j)	R_o≥2max(Δu_j,Δv_j,Δw_j)
3DΛ	R_o<2max(Δu_j,Δv_j,Δw_j)+Δu_i	R_o≥2max(Δu_j,Δv_j,Δw_j)+Δu_i

$M_{3D\Pi,1}$, $M_{3D\Pi,3}$ and $M_{3D\Pi,5}$ are exactly the same for regions I and II. As for $M_{3D\Pi,0}$, $M_{3D\Pi,2}$ and $M_{3D\Pi,4}$, the expressions in region II are different. Since the expressions for $M_{3D\Pi,0}$, $M_{3D\Pi,2}$ and $M_{3D\Pi,4}$ are rather similar, only the expression for $M_{3D\Pi,0}$ is given in equation (3.38). The expression for $M_{3D\Pi,2}$ can be obtained by replacing all the

coefficients of $M_{3D\Pi,0}$ from A_{mn} to B_{mn} and β_0 to β_2. Similarly, the expression for $M_{3D\Pi,4}$ can be obtained by replacing all the coefficients of $M_{3D\Pi,0}$ from A_{mn} to C_{mn} and β_0 to β_4.

$$\begin{aligned} M_{3D\Pi,0} = \beta_0 \Delta u_j \Delta v_j \Delta w_j \Bigg[& A_{000} + A_{200}\frac{(\Delta u_j)^2}{12} + A_{020}\frac{(\Delta v_j)^2}{12} + A_{002}\frac{(\Delta w_j)^2}{12} \\ & + A_{400}\frac{(\Delta u_j)^4}{80} + A_{040}\frac{(\Delta v_j)^4}{80} + A_{004}\frac{(\Delta w_j)^4}{80} \\ & + A_{220}\frac{(\Delta u_j)^2(\Delta v_j)^2}{144} + A_{202}\frac{(\Delta u_j)^2(\Delta w_j)^2}{144} + A_{022}\frac{(\Delta v_j)^2(\Delta w_j)^2}{144} \Bigg] \end{aligned} \tag{3.38}$$

Similarly, the expressions for $M_{3D\Lambda r,1}$, $M_{3D\Lambda r,3}$, $M_{3D\Lambda r,5}$, $M_{3D\Lambda f,1}$, $M_{3D\Lambda f,3}$ and $M_{3D\Lambda f,5}$ are exactly the same for regions I and II. As for $M_{3D\Lambda r,0}$, $M_{3D\Lambda r,2}$, $M_{3D\Lambda r,4}$, $M_{3D\Lambda f,0}$, $M_{3D\Lambda f,2}$ and $M_{3D\Lambda f,4}$, the expressions in region II are different. Since the expressions for $M_{3D\Lambda r,0}$, $M_{3D\Lambda r,2}$ and $M_{3D\Lambda r,4}$ are rather similar, only the expression for $M_{3D\Lambda r,0}$ is given in equation (3.39); the expressions for $M_{3D\Lambda f,0}$, $M_{3D\Lambda f,2}$ and $M_{3D\Lambda f,4}$ are also similar, only the expression for $M_{3D\Lambda f,0}$ is given in equation (3.40). The expression for $M_{3D\Lambda r,2}$ and $M_{3D\Lambda f,2}$ can be obtained by replacing all the coefficients of $M_{3D\Lambda r,0}$ and $M_{3D\Lambda f,0}$, respectively from A_{mn} to B_{mn} and β_0 to β_2. Similarly, the expression for $M_{3D\Lambda r,4}$ and $M_{3D\Lambda f,4}$ can be obtained by replacing all the coefficients of $M_{3D\Lambda r,0}$ and $M_{3D\Lambda f,0}$, respectively from A_{mn} to C_{mn} and β_0 to β_4.

$$
\begin{aligned}
M_{3D\Delta r,0} = {} & \frac{\beta_0 \Delta u_i \Delta u_j \Delta v_j \Delta w_j}{2} \Bigg\{ A_{000} + A_{200} \frac{(\Delta u_i)^2 + (\Delta u_j)^2}{12} + A_{020} \frac{(\Delta v_j)^2}{12} \\
& + A_{002} \frac{(\Delta w_j)^2}{12} + A_{400} \left[\frac{(\Delta u_i)^4 + (\Delta u_j)^4}{80} + \frac{(\Delta u_i)^2 (\Delta u_j)^2}{24} \right] + A_{040} \frac{(\Delta v_j)^4}{80} \\
& + A_{004} \frac{(\Delta w_j)^4}{80} + \frac{(\Delta u_i)^2 + (\Delta u_j)^2}{144} \left[A_{220} (\Delta v_j)^2 + A_{202} (\Delta w_j)^2 \right] \\
& + A_{022} \frac{(\Delta v_j)^2 (\Delta w_j)^2}{144} \Bigg\} - \beta_0 \Delta u_i (\Delta u_j)^2 \Delta v_j \Delta w_j \Bigg\{ \frac{A_{100}}{12} \\
& + A_{300} \left[\frac{(\Delta u_i)^2}{48} + \frac{(\Delta u_j)^2}{80} \right] + A_{120} \frac{(\Delta v_j)^2}{144} + A_{102} \frac{(\Delta w_j)^2}{144} \\
& + A_{500} \left[\frac{(\Delta u_i)^4}{192} + \frac{(\Delta u_j)^4}{448} + \frac{(\Delta u_i)^2 (\Delta u_j)^2}{96} \right] + A_{140} \frac{(\Delta v_j)^4}{960} + A_{104} \frac{(\Delta w_j)^4}{960} \\
& + \left[A_{320} (\Delta v_j)^2 + A_{302} (\Delta w_j)^2 \right] \left[\frac{(\Delta u_i)^2}{576} + \frac{(\Delta u_j)^2}{960} \right] + A_{122} \frac{(\Delta v_j)^2 (\Delta w_j)^2}{1728} \Bigg\}
\end{aligned} \tag{3.39}
$$

$$
\begin{aligned}
M_{3D\Delta f,0} = {} & \frac{\beta_0 \Delta u_i \Delta u_j \Delta v_j \Delta w_j}{2} \Bigg\{ A_{000} + A_{200} \frac{(\Delta u_i)^2 + (\Delta u_j)^2}{12} + A_{020} \frac{(\Delta v_j)^2}{12} \\
& + A_{002} \frac{(\Delta w_j)^2}{12} + A_{400} \left[\frac{(\Delta u_i)^4 + (\Delta u_j)^4}{80} + \frac{(\Delta u_i)^2 (\Delta u_j)^2}{24} \right] + A_{040} \frac{(\Delta v_j)^4}{80} \\
& + A_{004} \frac{(\Delta w_j)^4}{80} + \frac{(\Delta u_i)^2 + (\Delta u_j)^2}{144} \left[A_{220} (\Delta v_j)^2 + A_{202} (\Delta w_j)^2 \right] \\
& + A_{022} \frac{(\Delta v_j)^2 (\Delta w_j)^2}{144} \Bigg\} + \beta_0 \Delta u_i (\Delta u_j)^2 \Delta v_j \Delta w_j \Bigg\{ \frac{A_{100}}{12} \\
& + A_{300} \left[\frac{(\Delta u_i)^2}{48} + \frac{(\Delta u_j)^2}{80} \right] + A_{120} \frac{(\Delta v_j)^2}{144} + A_{102} \frac{(\Delta w_j)^2}{144} \\
& + A_{500} \left[\frac{(\Delta u_i)^4}{192} + \frac{(\Delta u_j)^4}{448} + \frac{(\Delta u_i)^2 (\Delta u_j)^2}{96} \right] + A_{140} \frac{(\Delta v_j)^4}{960} + A_{104} \frac{(\Delta w_j)^4}{960} \\
& + \left[A_{320} (\Delta v_j)^2 + A_{302} (\Delta w_j)^2 \right] \left[\frac{(\Delta u_i)^2}{576} + \frac{(\Delta u_j)^2}{960} \right] + A_{122} \frac{(\Delta v_j)^2 (\Delta w_j)^2}{1728} \Bigg\}
\end{aligned} \tag{3.40}
$$

3.4 Efficiency and Accuracy of the Semi-Analytical Method

To demonstrate the computational efficiency of the proposed semi-analytical method, computation times for a matrix element using 16-point quadrature integration, 128-point quadrature integration, semi-analytical expression for region I and semi-analytical expression for region II are compared and tabulated in Table 3.10. All results provided in Table 3.10 are obtained using a Pentium D 820 CPU (2.8 GHz). Taking the 16-point quadrature integration as the reference, relative speed improvement factors for computing integrations of four basis functions: 2D pulse, 2D triangular, 3D pulse and 3D triangular, respectively, are nearly 40, 250, 210, 1200 for region I and 100, 1000, 1300, 14000 for region II, respectively.

Table 3.10 CPU times for one matrix element using different methods

	16-point quadrature	128-point quadrature	Region I	Region II
2D pulse	0.0422 ms	2.66 ms	0.937 μs	0.422 μs
2D triangular	0.6844 ms	349.69 ms	2.734 μs	0.672 μs
3D pulse	0.6515 ms	333.6 ms	3.032 μs	0.5 μs
3D triangular	10.5813 ms	43.575 s	8.61 μs	0.718 μs

A microstrip line structure with load end short-circuited, as shown in Fig. 3.3, is used as a test case. The dimensions of the microstrip line: length = 100 mm, width = 10 mm, thickness = 2 mm and ground plane width = 50 mm. The microstrip line structure is subdivided with equal rectangular cells 10 mm by 10 mm by 2 mm. The matrix size of the microstrip line structure is 245 by 245. Table 3.11 shows that matrix-fill time is reduced by nearly 440 times with respect to the 16-points quadrature approach or 1,300,000 times with respect to the 128-points quadrature approach.

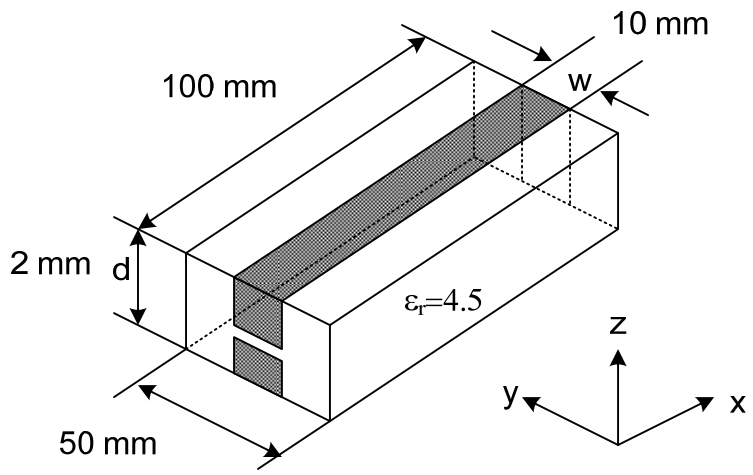

Fig. 3.3 A short-circuited microstrip line

Table 3.11 Matrix-fill times for microstrip structure using different methods

	16-point quadrature	128-point quadrature	Approximated method
Microstrip structure	302.57 s	911,842 s	0.685 s

To check for solution accuracy, the current distributions along the short-circuited microstrip line at 350 MHz (the resonant frequency) and 1 GHz with 1 V excitation source, using the semi-analytical method, the 16-point quadrature integration and the 128-point quadrature integration are shown in Fig. 3.4 and Fig. 3.5, respectively.

The comparisons show that the semi-analytical method is in very good agreement with the 128-point quadrature integration method. The 16-point quadrature integration method produces significantly higher current than the other two methods. The discrepancy is expected because the 16-point quadrature integration is expected to incur larger error in the integration.

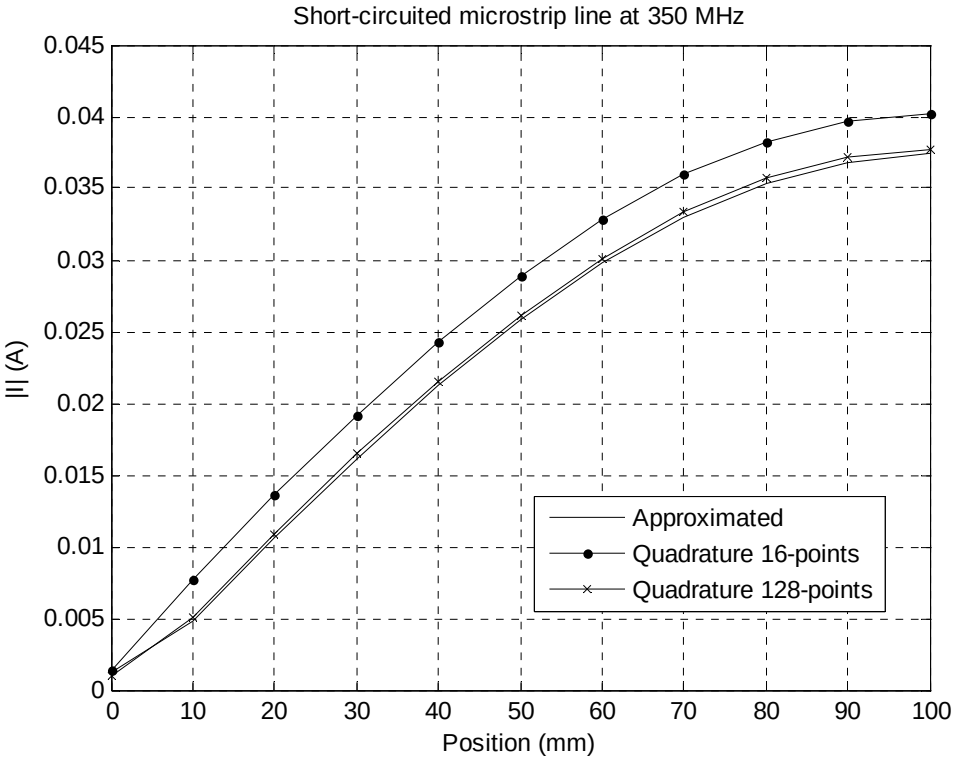

Fig. 3.4 Current distributions of the short-circuited microstrip line at 350 MHz

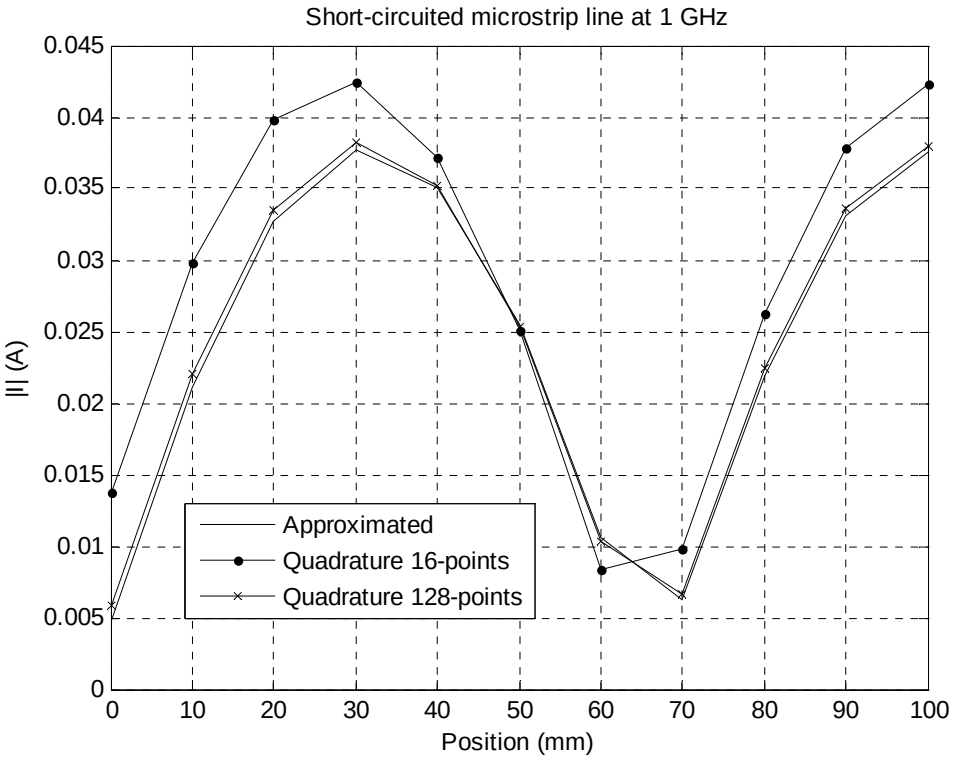

Fig. 3.5 Current distributions of the short-circuited microstrip line at 1 GHz

The plots of real and imaginary parts of input impedance versus frequency of the short-circuited microstrip line using the three approaches are shown in Fig. 3.6 and Fig. 3.7, respectively. Again, the semi-analytical method is in close agreement with the 128-point quadrature integration method. The 16-points quadrature integration method matches quite well with the other two methods but significant discrepancies show up at the resonant frequency.

With the above comparison in both computational speed and accuracy, the semi-analytical method proposed in this thesis has been proven to be as accurate as the 128-point quadrature integration method but with very much reduced CPU time.

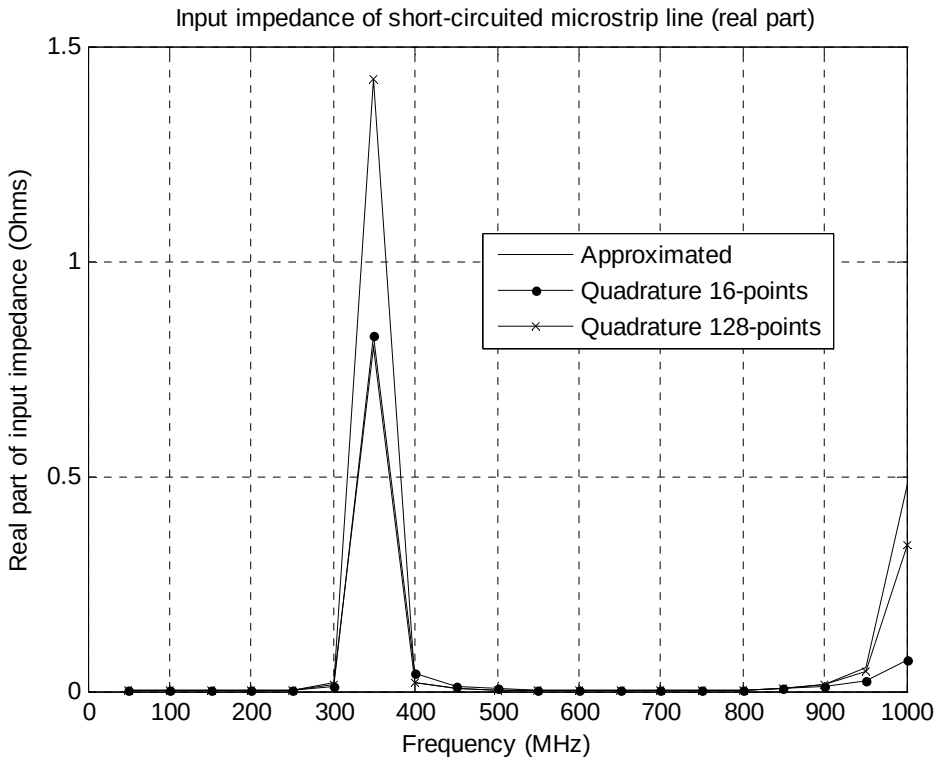

Fig. 3.6 Input impedance of the short-circuited microstrip line (real part)

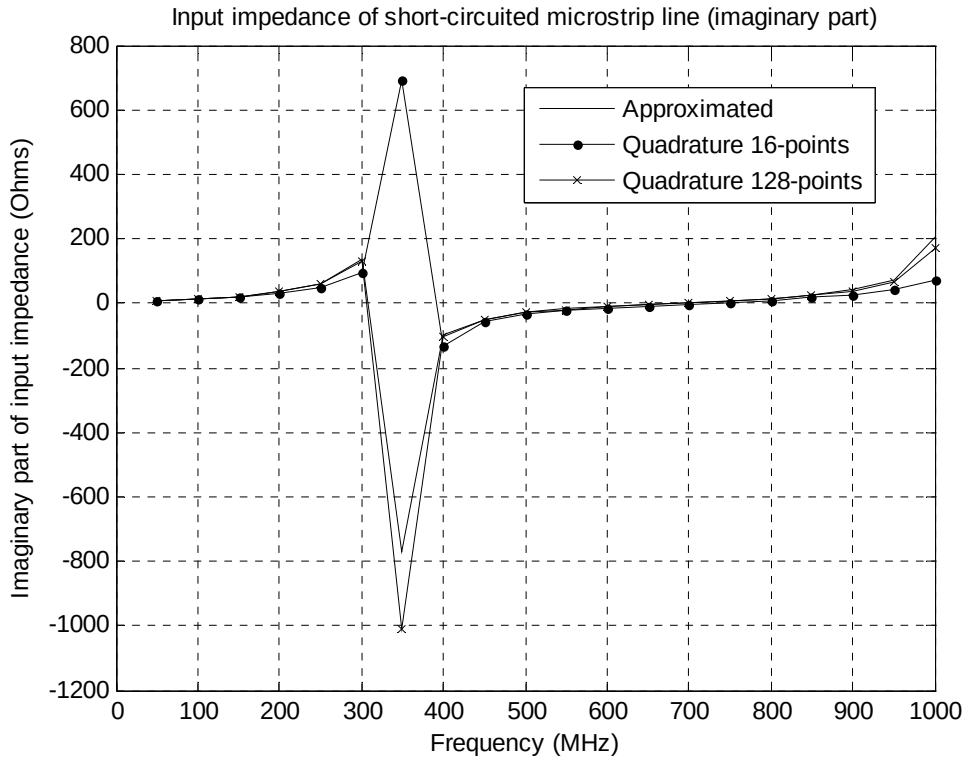

Fig. 3.7 Input impedance of the short-circuited microstrip line (imaginary part)

3.5 Implementation of Matrix Solution

As mentioned before, the total solution time consists of both the matrix-fill time and matrix-solve time. As discussed in the previous sections, using semi-analytical method has reduced the matrix-fill time significantly. The next improvement is to find an efficient and accurate algorithm to minimise the matrix-solve time.

In general, solution of a matrix can be classified into two categories – the direct method and the iteration method. For the direct method, there are two main solutions – the matrix inversion method and the Gaussian elimination method [99]. The complexity of the matrix inversion method is $4n^3/3 + O(n^2)$, whereas the complexity of the Gaussian elimination method is $n^3/3 + O(n^2)$ [100]. Therefore, the Gaussian elimination method

has been popular for solving matrices in most cases. Since most computers use a finite-size representation of a numeric value, there will be round-off error [99]. The round-off errors will be accumulated and becomes large after some arithmetic operations. Hence, the LU (lower-upper) factorisation method for asymmetrical matrix and the LDL^t (lower-diagonal-lower transpose) factorisation method for symmetrical matrix are used to solve the matrix [99]. For matrix that is asymmetrical, the LU factorisation method is preferred.

As the matrix size increases, the error accumulated by the direct method is expected to be large. Hence, the iteration method is preferred for large matrix. However, iteration method may not guarantee convergence, which means, in some cases, the error may diverge to larger value instead of converge to smaller value. Therefore, selecting a suitable iteration schemes due to the specific condition of the matrix is important. There are several iteration schemes in literature, such as Jacobi iterative algorithm, Gauss-Seidel iterative algorithm, conjugate gradient algorithm (CG), squaring the conjugate gradient algorithm (CGS), bi-conjugate gradient algorithm (Bi-CG), bi-conjugate gradient stable algorithm (Bi-CGSTAB) and generalized minimal residual algorithm (GMRES) [99]–[104]. Among these algorithms, the Jacobi iterative algorithm and Gauss-Seidel iterative algorithm are the simplest but in order to guarantee convergence, the matrix need to be diagonally dominant. The impedance matrix generated is normally ill-conditioned. Hence, both algorithms are not suitable in this case. The CG method is suitable for a real symmetric positive definite (SPD) coefficient matrix, but the impedance matrix is asymmetrical. Although CGS, Bi-CG, Bi-CGSTAB and GMRES are used to solve asymmetric matrix, the algorithms are developed based on solving real asymmetric matrix. Due to the fact that the impedance matrix is a complex

asymmetric matrix, these algorithms may not work well. After some careful studies, although the GMRES requires more memory, it is found to be suitable to solve the matrix for our problem.

CHAPTER FOUR

4 VALIDATION AND APPLICATIONS IN EMI/SI ANALYSIS

Based on the full-wave equivalent circuit extraction algorithm described in Chapter 2 and the computational efficient technique proposed in Chapter 3, an efficient and accurate circuit extraction code has been successfully developed using C++ programming language. To ensure the developed code functions properly, the code will be validated. Firstly, the simulated results using the code are compared with well-established commercial EM software HFSS [105] . Secondly, the simulated results are verified with experimental results.

The ability to extract the full-wave equivalent circuit of any printed circuit structure enables one to investigate a specific interconnect layout on PCB, in terms of EMI and SI performances, such as ground bounce, radiated emission and common-mode current issue, etc. Three examples are demonstrated in this chapter to show how the extracted equivalent circuit could be applied for EMI or SI analyses.

The first example illustrates how the different grounding arrangements in PCB layout affect the ground voltage drop. Such analysis allows one to understand the underlying principles of good grounding practices. The second example investigates the relationship between ground bounce and CM radiation from a PCB. The last example

translates the radiated emission limit into a maximum allowable ground bounce limit for any specific signal path on the PCB, which serves as a good indication of EMI compliance.

4.1 Validation of extracted full-wave equivalent circuit model

To validate the extracted full-wave circuit model using the developed code, a large conducting loop supported by a 50 mm × 50 mm × 1.6 mm substrate with dielectric constant of 4.5 is fabricated, as shown in Fig. 4.1. The width of the conducting trace is 0.35 mm and the perimeter of the loop is 149 mm. The purpose of choosing this large loop for connection between signal source and load is to demonstrate the ability of the proposed model in predicting the voltage drop along the loop. The large circuit loop is expected to exhibit high inductance and therefore results in significant voltage drop on the signal conductors. The structure is subdivided with variable cell sizes to reduce the computational effort. Smaller cells are used where finer details (such as bends) are to be modelled properly and larger cells are used for non-critical area such as substrate further away from the conductor. The largest cell is 9.825 mm by 7.325 mm by 1.6 mm and the smallest cell is 0.35 mm by 0.35 mm by 1.6 mm. With the variable subdivisions, a total of 36 circuit nodes on the conductor are resulted. The simplified full-wave model of the given loop is extracted and imported to a SPICE-based tool for simulation.

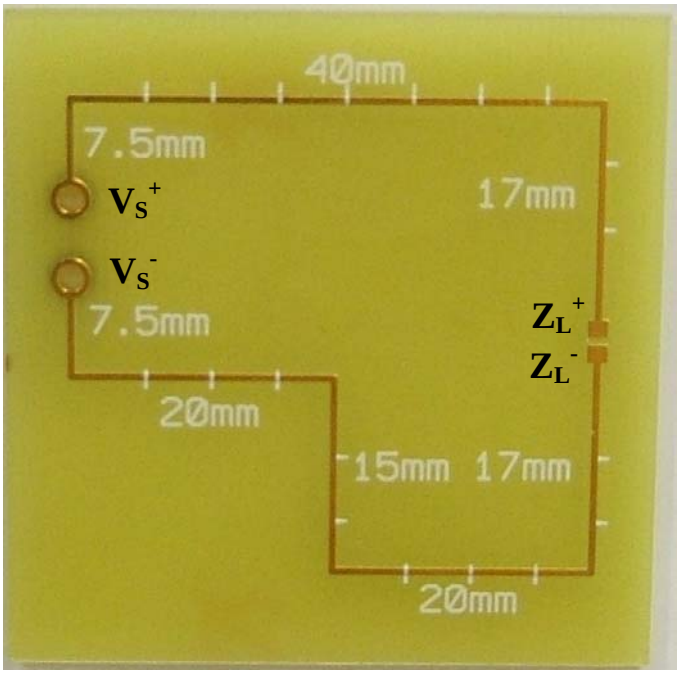

Fig. 4.1 Fabricated closed conducting loop

To verify the extracted full-wave model, the input impedance of the loop (between V_s^+ and V_s^-) is determined using the full-wave model and compared with that obtained through a commercial EM solver HFSS. In the simulation, the load end (between Z_L^+ and Z_L^-) is a shorted, i.e. $Z_L = 0\ \Omega$. The real and imaginary parts of the input impedance of the loop, up to 1.5 GHz, are plotted in Fig. 4.2 and Fig. 4.3, respectively. Both simulated results obtained using the proposed full-wave model and the HFSS are in good agreements. The half-wavelength resonance around 750 MHz is clearly observed in both simulated results. Hence, extracted full-wave model has been verified to be correct.

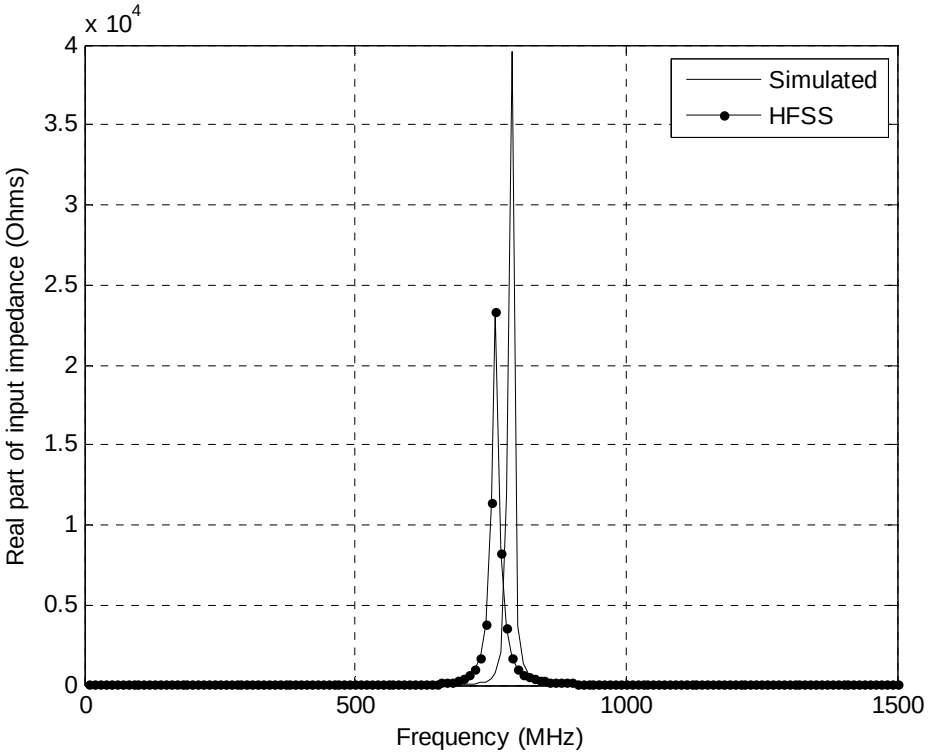

Fig. 4.2 Real part of the input impedance versus frequency with the load end short-circuited

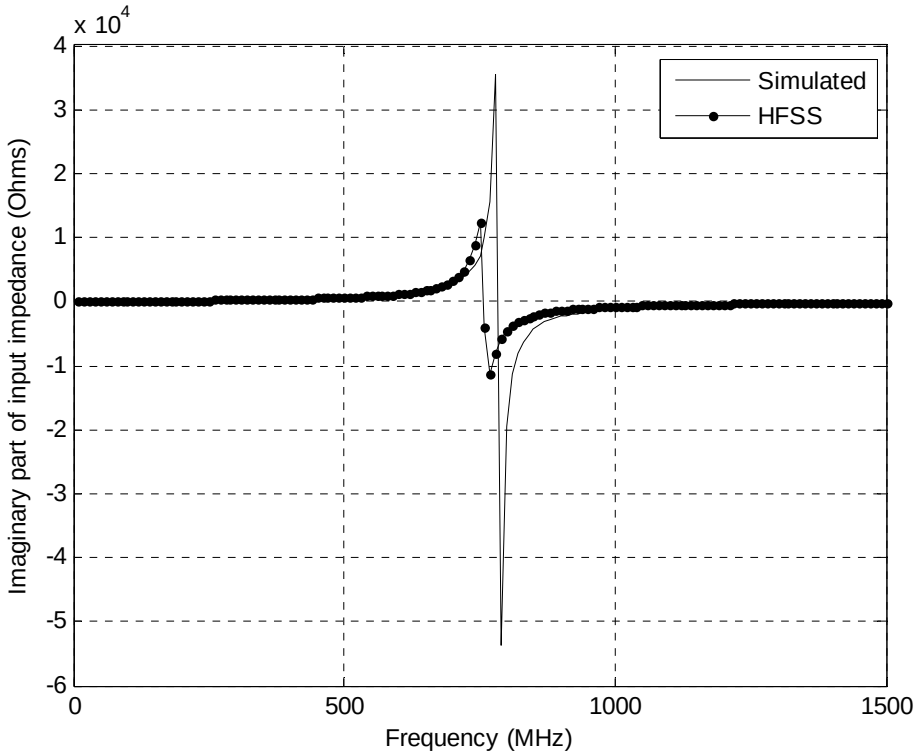

Fig. 4.3 Imaginary part of input impedance versus frequency with the load end short-circuited

The same loop structure will be used again for experimental validation. With the extracted full-wave model, it is possible to predict the voltage drop along the conductor, which is not readily obtainable from the commercial EM simulation tools. An HP 8648C signal generator is employed to provide the input signal across V_s^+ and V_s^- through an SMA connector. The source voltage is maintained constant at 1V for all measurement frequencies. Terminals Z_L^+ and Z_L^- are connected with a 51 Ω SMT resistor. For ease of reference in the simulated and measured results, V_s^+ and V_s^- are identified as the starting and ending points of the loop. Hence the position of V_s^+ is denoted as 0 mm and the position of V_s^- is denoted as 149 mm. An HP 8593E spectrum analyzer and an HP 85024A high impedance RF voltage probe (with a bandwidth of 3 GHz) are used to measure the RF voltage drop along the conductor with respect to V_s^-. The HP 85024A probe has an input capacitance of only 0.7 pF in parallel with 1 MΩ allows high frequency probing without adversely loading the circuit under test.

Fig. 4.4 shows the comparison of simulated and measured voltage drop along the loop at 50 MHz. The "0 mm" position refers to V_s^+. As expected, the voltage at "0 mm" is 1 V and the voltage at "149 mm" is 0 V, which is where the signal source is connected. As the position increases from "0 mm", voltage reduces linearly due to the voltage drop on the conductor because of excessive loop inductance. Between the points of Z_L^+ and Z_L^-, there is an abrupt voltage drop because of the 51 Ω load. After the Z_L^- point, similar linear reduction in voltage drop is observed again due to the loop inductance. Very good agreement between the simulated and the measured results are demonstrated in Fig. 4.4.

Fig. 4.5 shows the similar comparison of simulated and measured voltage drop along the loop at a higher frequency at 500 MHz. At this frequency, no abrupt voltage drop between Z_L^+ and Z_L^- , where the 51 Ω load is connected, is observed this time. It indicates that the inductive reactance of the loop has become so large that practically the signal voltage is dropped on the loop instead of the load. Again, the simulated result shows exactly the same behaviour as the measured result with good agreement.

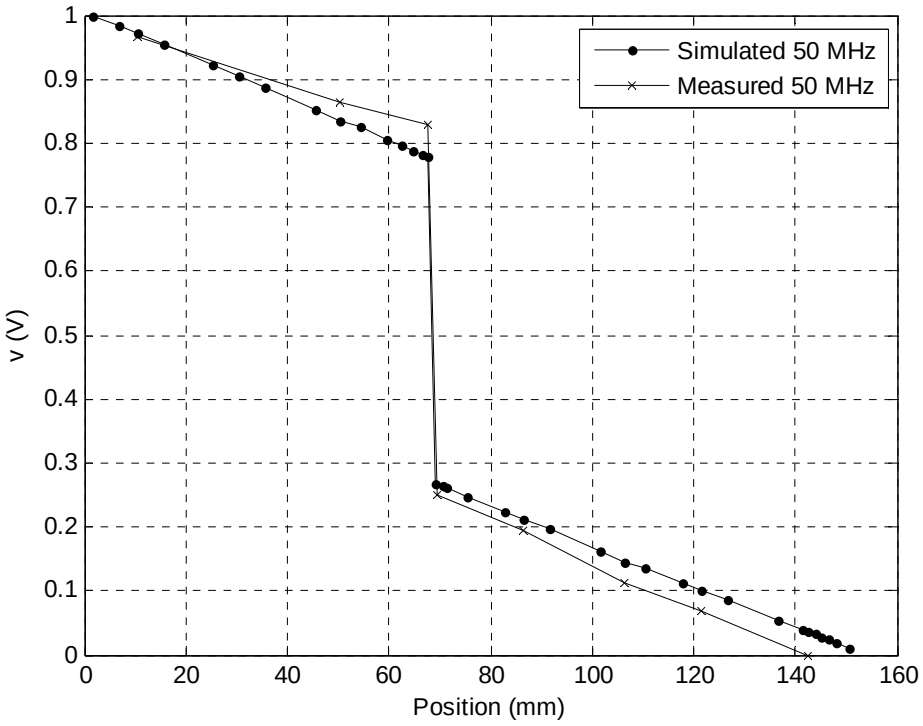

Fig. 4.4 Voltage along the closed conducting loop with a 51 Ω load at 50 MHz

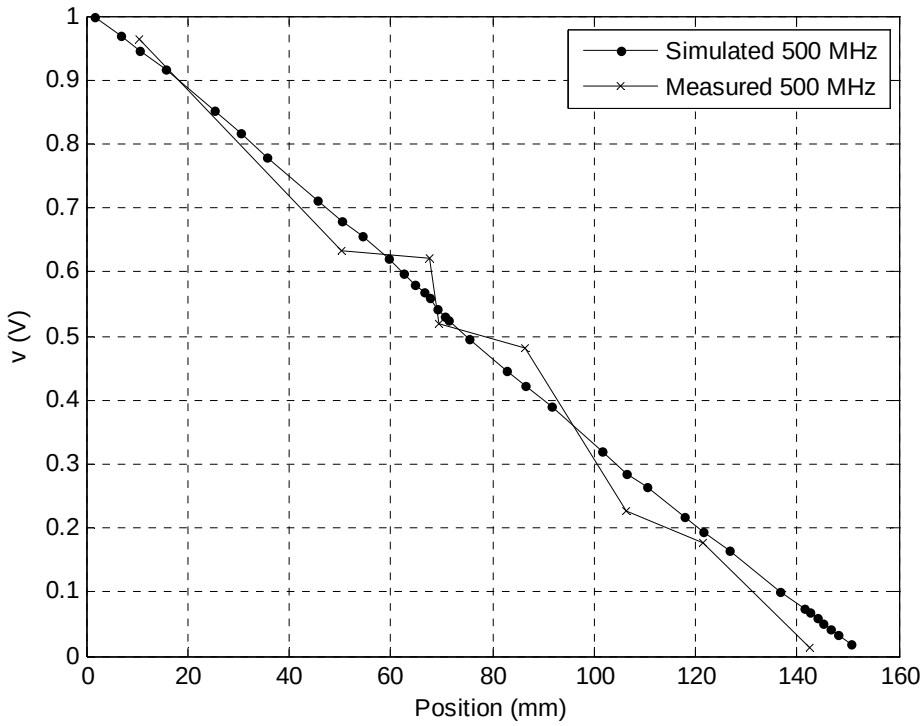

Fig. 4.5 Voltage along the closed conducting loop with a 51 Ω load at 500 MHz

To explain such voltage drop behaviour, the real and imaginary components of the input impedance are simulated and plotted in Fig. 4.6. It shows that at low frequency, the input impedance is primarily resistive in nature due to the load resistance of 51 Ω. At 500 MHz, the inductive reactance of the loop (≈ 800 Ω) dominates and the input impedance is now determined mainly by the inductive reactance. Therefore, at 500 MHz, all the voltage from the signal source is dropped on the conducting loop and the load Z_L essentially receives negligible voltage from the signal source. To illustrate the point, the voltage drops across the ground conductor (between V_s^- and Z_L^-) and the signal conductor (between V_s^+ and Z_L^+) are simulated and plotted in Fig. 4.7. It shows that voltage drops on signal and ground conductors at 50 MHz are 0.32 V and 0.36 V, respectively. Hence, the voltage across the load is about 0.32 V. When frequency increases to 500 MHz, the total voltage drop on the interconnecting conductors is

nearly 0.97 V, with 0.52 V on the ground conductor and another 0.45 V on the signal conductor. Hence, the voltage across the load reduces to 0.03 V.

The section has validated the extracted full-wave model through comparisons with HFSS and with experimental results. The subsequent sections will demonstrate the versatility of full-wave circuit model in many EMI/SI analyses.

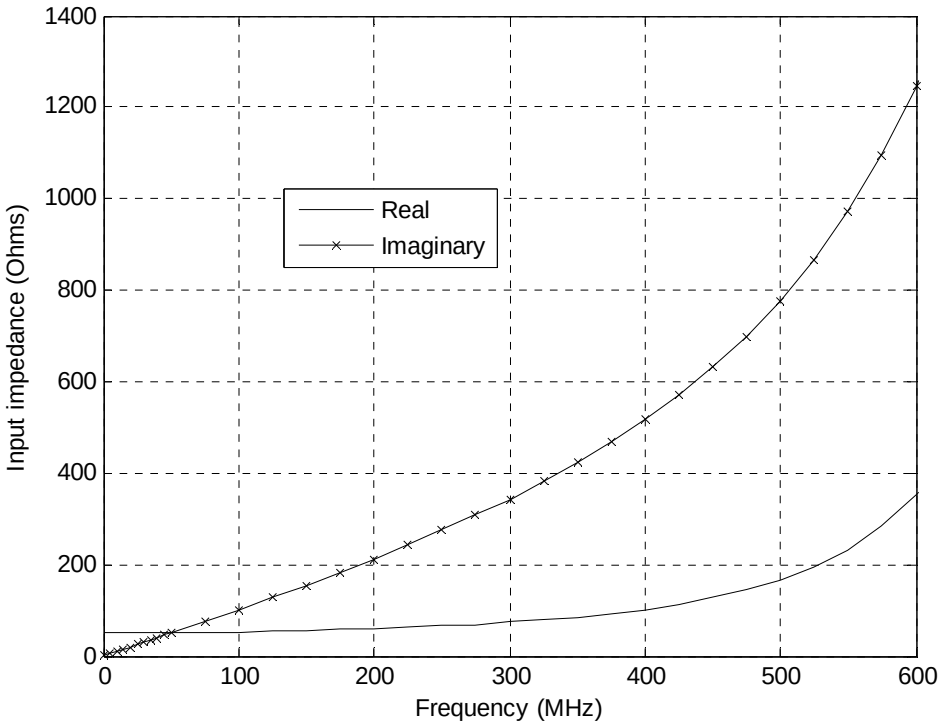

Fig. 4.6 Input impedance for a closed conducting loop PCB with a 51 Ω load

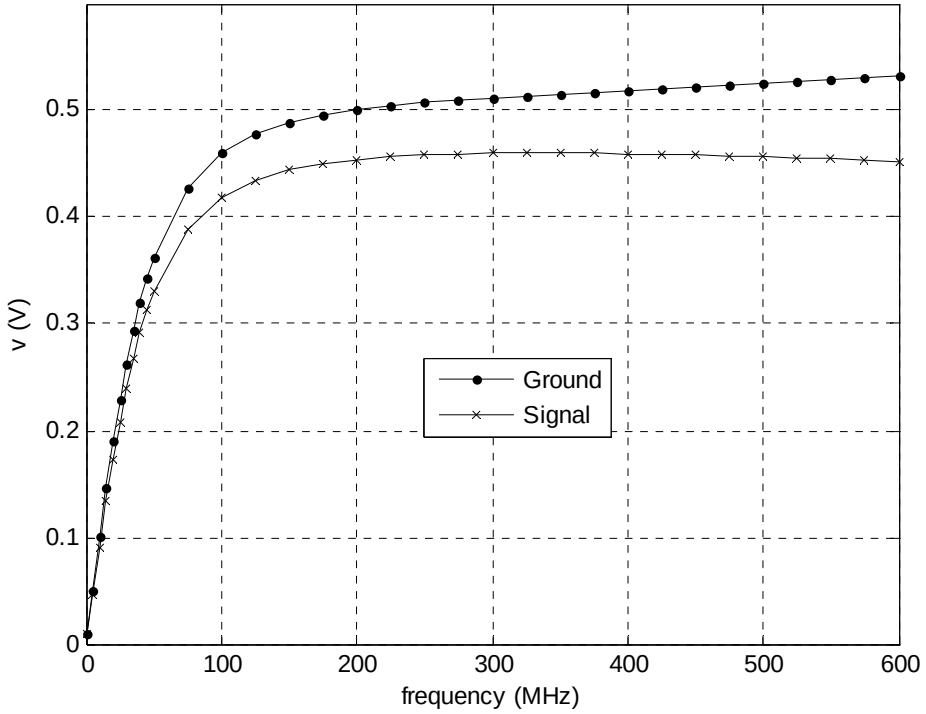

Fig. 4.7 Ground voltage and signal voltage for a closed conducting loop PCB with a 51 Ω load

4.2 Application Examples for EMI/SI Analyses

4.2.1 Assessment of Different Grounding Arrangement in PCB Layout

The first application example illustrates the useful feature of the proposed full-wave model in assessing different grounding arrangement in PCB layout through prediction of ground voltage drop. Using the closed conducting loop structure in Fig. 4.1 as an example again, two different grounding arrangements are studied here. The first layout arrangement has a full ground plane below the loop but there is no connection between the loop and the ground plane. Using this image plane arrangement, the voltage drop

across the ground conductor of the loop versus frequency is calculated and plotted from 1 MHz to 600 MHz, as shown in Fig. 4.8. Using the ground conductor voltage drop of the loop without image plane as a reference, the voltage drop on the ground conductor with the image plane shows some variation but does not differ by very much. Hence, adding an image plane underneath the signal loop has little influence on the voltage drop of the ground conductor of the loop.

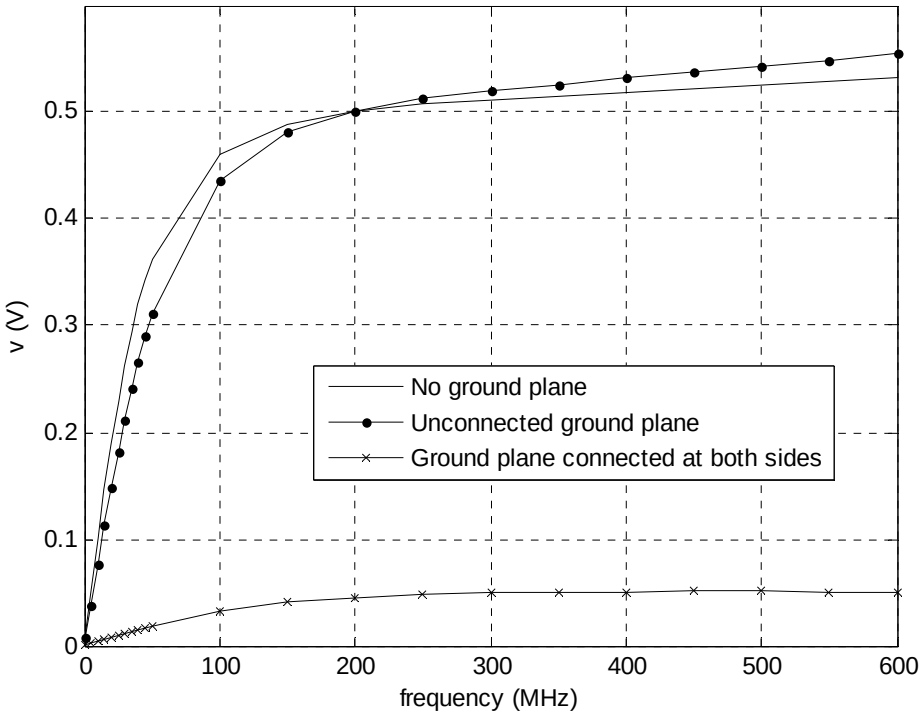

Fig. 4.8 Ground voltage for a closed conducting loop PCB without ground plane with a 51 Ω load and ground voltage for a closed conducting loop PCB with ground plane with a 51 Ω load

The second arrangement is similar to the first one. There is still a full ground plane underneath the signal loop but the ground plane is now connected to V_s^- and Z_L^- of the signal return path. The connection to ground plane facilitates an alternative return path for the signal conductor between V_s^+ and Z_L^+. The ground voltage drop versus

frequency is now simulated and plotted in Fig. 4.8 to compare with the previous arrangement. Now the ground voltage drop is significantly lower than the case where the image plane is not connected to V_s^- and Z_L^-. Fig. 4.9 shows a close-up plot of the ground voltage drop versus frequency with the new grounding arrangement. The ground voltage drop increases with frequency but finally stabilized at around 50 mV as the inductive reactance become dominant. The magnitude of the ground voltage drop (about 50 mV) is significantly lower than the previous arrangement (nearly 500 mV), which is a reduction of almost 10 times (or 20 dB). This result is expected, as the alternative return path in the ground plane tends to mirror the upper signal conductor so that the resultant signal loop area becomes the smallest. With this behaviour, the loop inductance is greatly reduced and hence, the ground voltage drop also reduces significantly. Fig. 4.10 and Fig. 4.11 show the real and imaginary components of the input impedance with different grounding arrangement. The real part is essentially the load resistance of 51 Ω. As frequency increases beyond 300 MHz, the resonance due to half-wavelength begins to show up. For the imaginary part, the inductive reactance is significantly lower when the connections of V_s^- and Z_L^- to the ground plane are made. Although there are many literatures have reported that using the ground plane as return path eliminates EMI problem at the board level, the example here shows how to make use of the full-wave circuit model to quantify ground voltage drop for EMI assessment purposes. The ability to predict voltage drop for different signal and power delivery paths on PCB allows potential EMI problems to be identified early during the PCB layout stage.

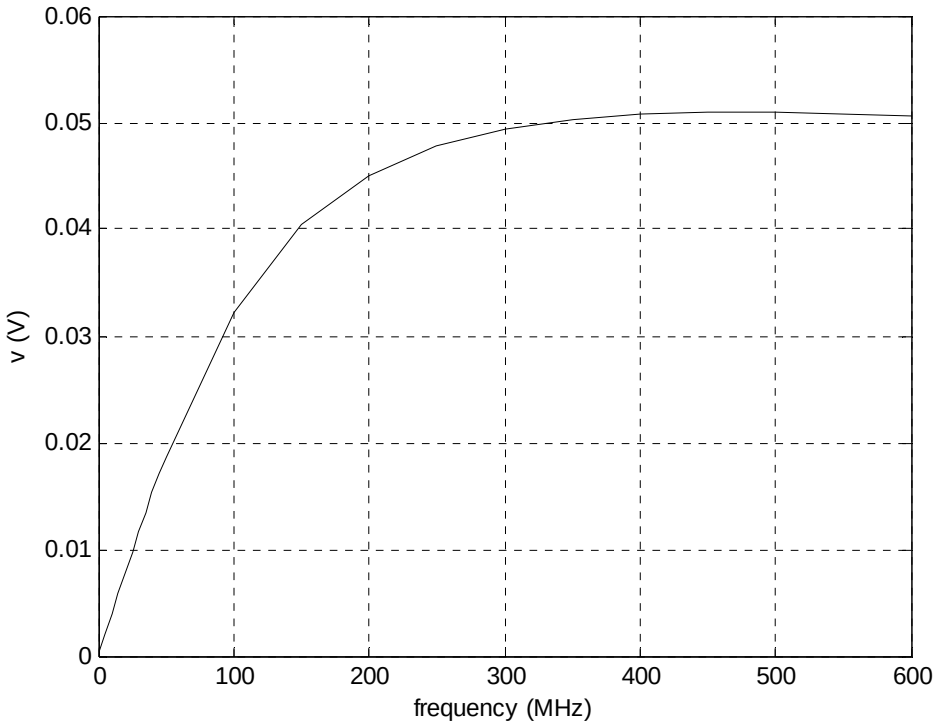

Fig. 4.9 Voltage difference between load ground and 0V ground with a 51 Ω load for a closed conducting loop PCB with shorted ground plane at both ends

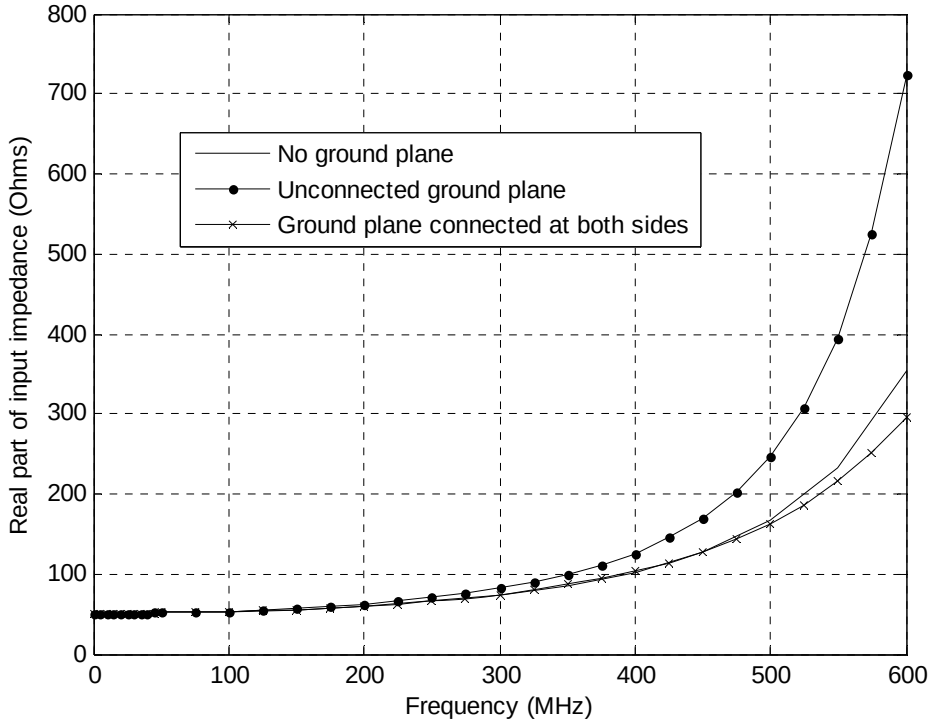

Fig. 4.10 Real part of input impedance for a closed conducting loop PCB with shorted ground plane at both ends with a 51 Ω load

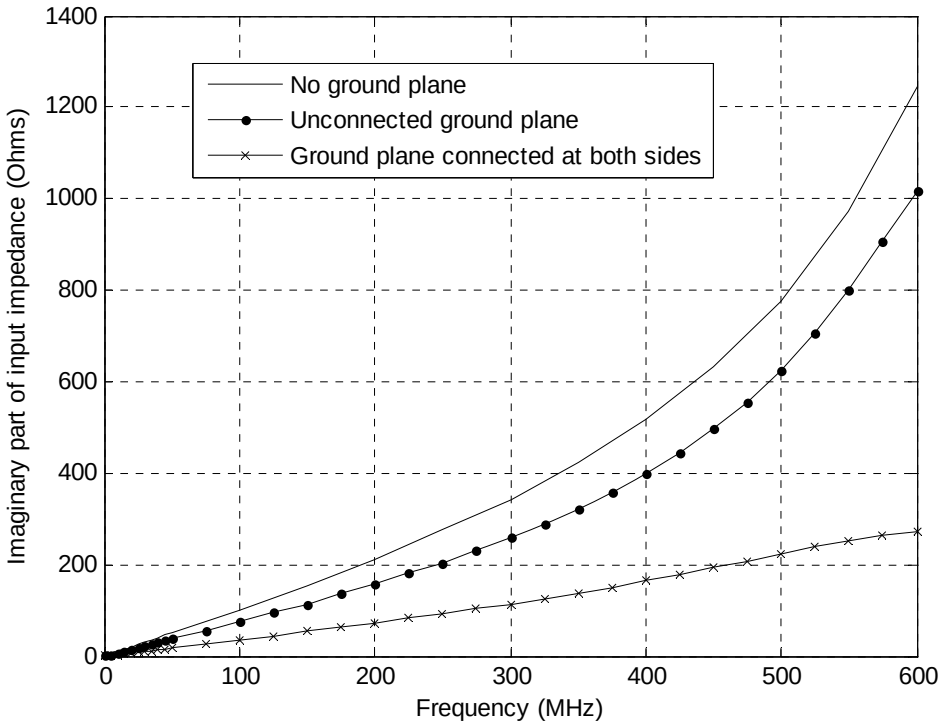

Fig. 4.11 Imaginary part of input impedance for a closed conducting loop PCB with shorted ground plane at both ends with a 51 Ω load

4.2.2 Investigation of Relationship between Ground Bounce and Common-Mode Radiation

The second application example investigates the relationship between ground bounce and CM radiation. Although many literatures have reported that CM radiation is due to significant ground bounce on the PCB, no comprehensive analysis is carried out. A microstrip line with a 50 mm × 17.5 mm × 1 mm substrate (ε_r = 2.45), a 50 mm × 17.5 mm ground plane and trace width of 2.5 mm, as shown in Fig. 4.12, is used as a case study. The microstrip line structure is subdivided into rectangular cells of equal size, where dimensions of each cell are 2.5 mm by 2.5 mm by 1 mm. The excitation source voltage V_S, applied at the source end of the microstrip line, is kept constant at 1V for

all the simulation frequencies. Five different loads to be connected at the opposite end (load end) of the microstrip line are selected in the study. These loads are 0 Ω (short-circuited), 10 Ω, 55 Ω (matched load), 100 Ω and ∞ (open-circuited).

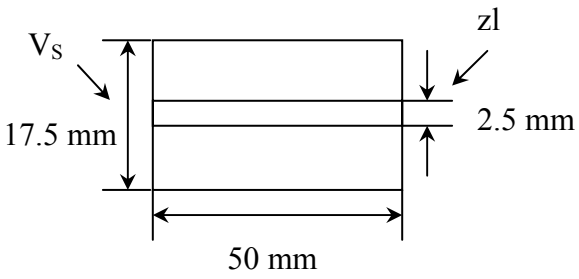

Fig. 4.12 A microstrip line

Fig. 4.13 shows the predicted ground voltage drops (vg) between the source and the load ends for the five different load terminations. Fig. 4.14 shows the predicted maximum radiated electric field (Emax) at 3 m from the microstrip line for the five different load terminations. The impedance of the microstrip line is basically the load and the loop inductive reactance, where it can be decomposed into upper trace net inductance L_t and ground inductance. vg is mainly due to the ground net inductance L_g, which is simply vg = $j\omega L_g I_l$ (I_l is the circuit loop current). Under short-circuited termination, the impedance of the circuit loop is inductive and the ground voltage drop is due to the ground inductance, which can be obtained by applying the potential divider rule from circuit theory, vg = $V_S L_g/(L_g + L_t)$. As frequency increases, both the upper trace inductance and ground inductance will remain rather constant, hence, vg will also remains rather constant with increasing frequency. When zl = 10 Ω, the

impedance of the circuit loop is dominated by the load resistance when the frequency is low but is dominated by the loop inductance when the frequency is high. At the lower frequency, the current is determined by the load resistance and remained rather constant. Hence, vg increases linearly with frequency. At the higher frequency, the loop inductive reactance dominates; vg becomes constant and approaches the same magnitude as in the case of the short-circuited load condition. With matched load, vg increases linearly as frequency increases. This is expected because under matched load condition, the circuit loop current remains constant and the ground inductive reactance is still increases linearly with frequency. Under the open-circuited condition, the current depends on the capacitive reactance and increases linearly with frequency. Therefore, vg has a second order increase with frequency. As for the zl = 100 Ω, vg will lie in between the vg curves with matched load and open-circuited load.

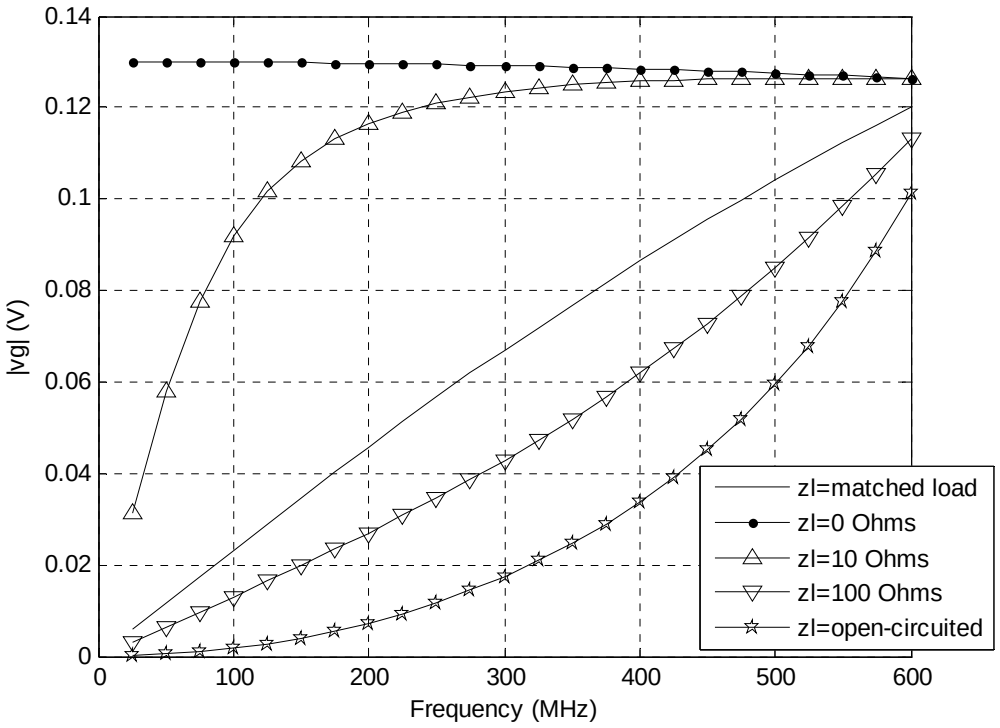

Fig. 4.13 |vg| of microstrip line under different load conditions

Fig. 4.14 shows that, in general, Emax of the microstrip line is lower with higher load impedance. Hence, the lowest Emax is observed with open-circuited load, where the loop current is lowest. It is observed that the radiated electric field and ground voltage drop has a strong correlation, where lower ground bounce indicates a lower level of radiation from the microstrip line.

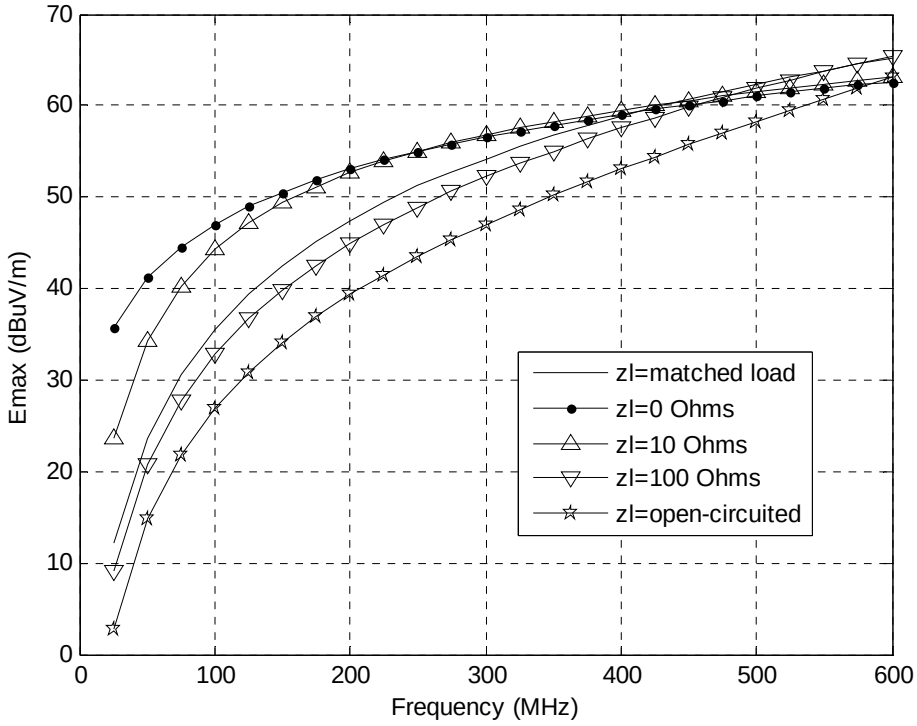

Fig. 4.14 Emax of microstrip line under different load conditions

Now a 100 mm conductor is attached to the ground of the same microstrip line, as shown in Fig. 4.15. The width of the attached conductor is 2.5 mm. Again, the excitation source voltage V_S is kept constant at 1V for all simulation frequencies and the same set of five different loads are selected in the simulation.

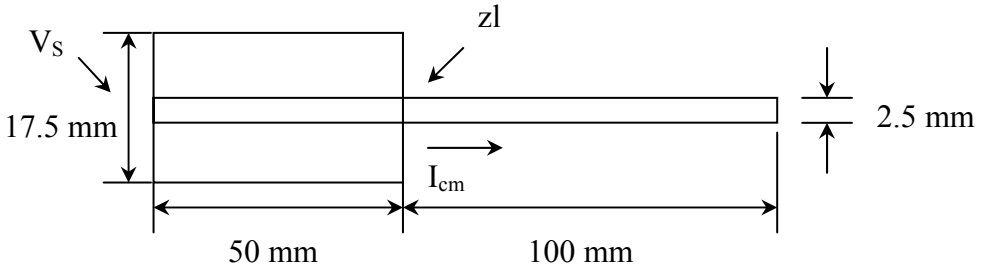

Fig. 4.15 A microstrip line with a 100 mm attached ground conductor

The simulated vg from 25 MHz to 600 MHz, for the various loads, are plotted in Fig. 4.16. Similar trends as those vg curves without the attached conductor are observed. Slight variation in vg with the attached conductor is expected because of additional asymmetry due to the attached conductor. Fig. 4.17 shows the predicted CM current (Icm) on the 100 mm attached conductor. Generally, lower load impedance produces lower Icm. This is because Icm depends on the load voltage, and lower load impedance will produce lower load voltage. Hence, lower load impedance will result in lower Icm. The maximum radiated electric fields at 3 m from the microstrip line with attached conductor for various loads are predicted and plotted in Fig. 4.18. With the attached conductor, increase in Emax is expected due to the additional CM radiation from the attached conductor. The level of increase varies with the load impedance. Under short-circuited load condition, the increase of Emax is very minimal, whereas Emax of open-circuited load increases significantly. Emax in Fig. 4.18 consists of both the DM radiation from the microstrip line and the CM radiation from the attached conductor. To know the DM and CM contributions in the overall radiation, the DM radiation from the microstrip line and the CM radiation from the attached conductor are decomposed and plotted separately. The DM radiation can be estimated by only consider the current flow in the microstrip line (excluding the attached conductor current). The CM

radiation can be estimated by only consider the attached conductor current. The DM and CM radiation plots are given in Fig. 4.19 and Fig. 4.20, respectively. DM radiation is clearly dominated in the lower frequency range, CM radiation is about 10 to 20 dB lower than the DM radiation (depending on the load). For low impedance loads (short-circuited and 10 Ω load), CM is lower than DM throughout the simulated frequency range. Beyond 450 MHz, those with higher impedance loads, the CM radiation become comparable to DM radiation and even higher than the DM radiation. By relating the ground bounce vg and the CM radiation with different load impedances, it is found higher vg not necessarily contributes to higher CM radiation from the attached conductor.

Generally, lower load impedance has lower CM radiation. Also, lower Icm produces lower CM radiation, hence, CM radiation is dependent on Icm. For low impedance loads (short-circuited and 10 Ω load), CM radiation is significantly lower than total Emax throughout the simulated frequency range. Beyond 500 MHz, those with higher impedance loads, the CM radiation become comparable to the total Emax. Although, it is generally believed that the cause of CM current on the cable is related to ground bounce of high-speed PCB, it is found from simulations that higher |vg| not necessarily contributes to higher CM radiation from the attached conductor.

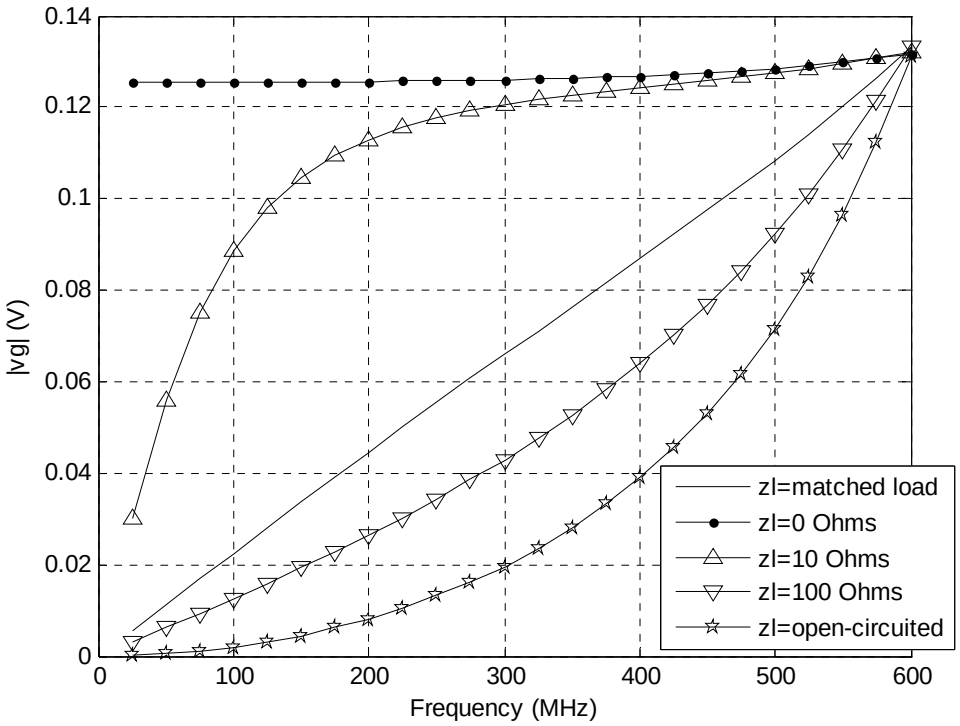

Fig. 4.16 |vg| of microstrip line with a 100 mm attached conductor under different load conditions

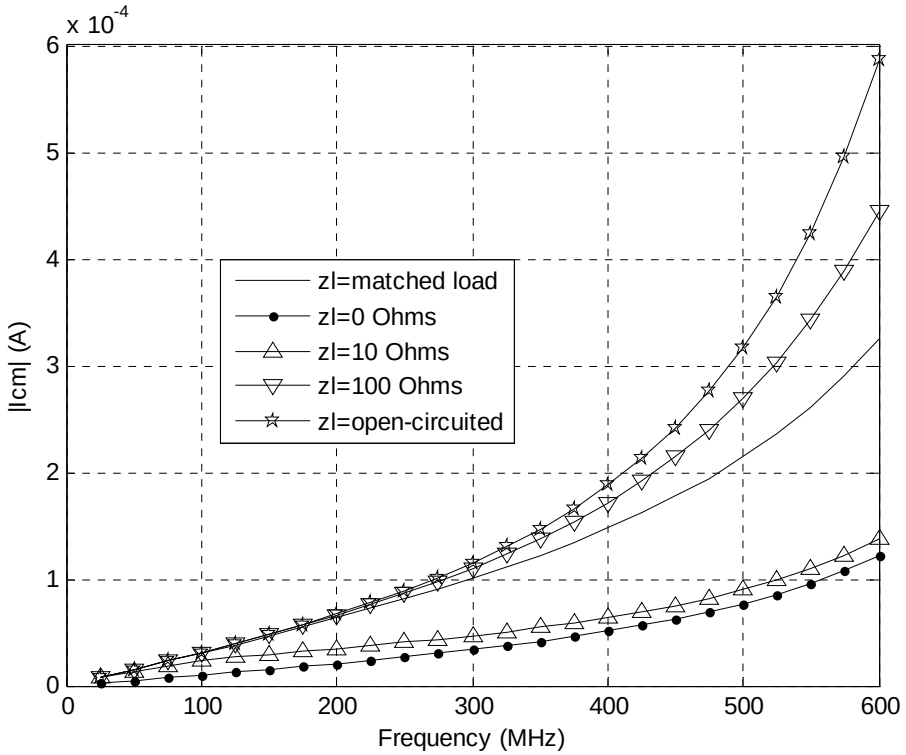

Fig. 4.17 |Icm| of microstrip line with a 100 mm attached conductor under different load conditions

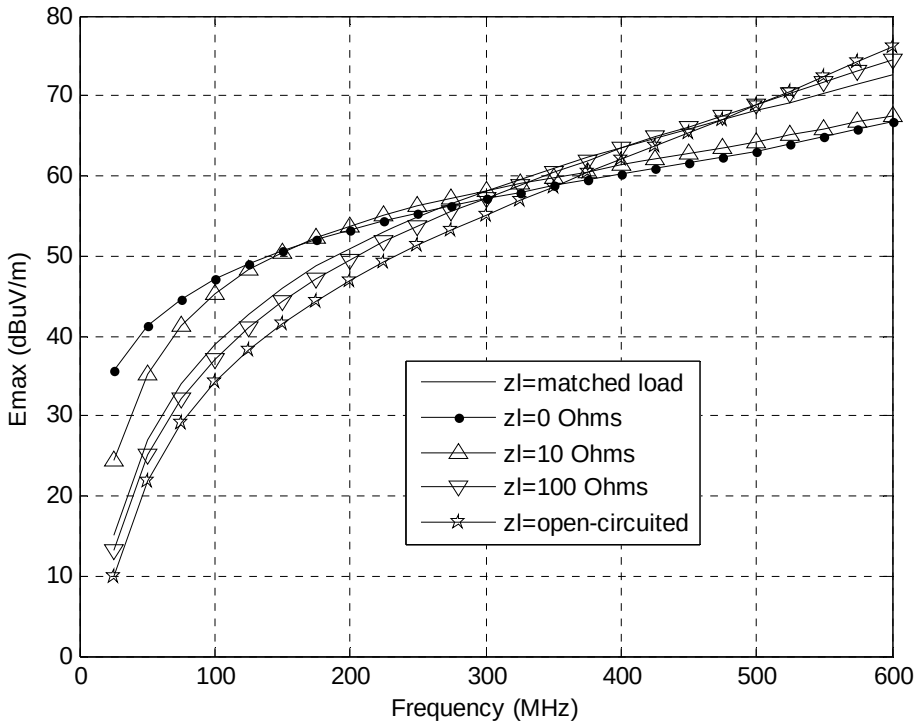

Fig. 4.18 Emax of microstrip line with a 100 mm attached conductor under different load conditions

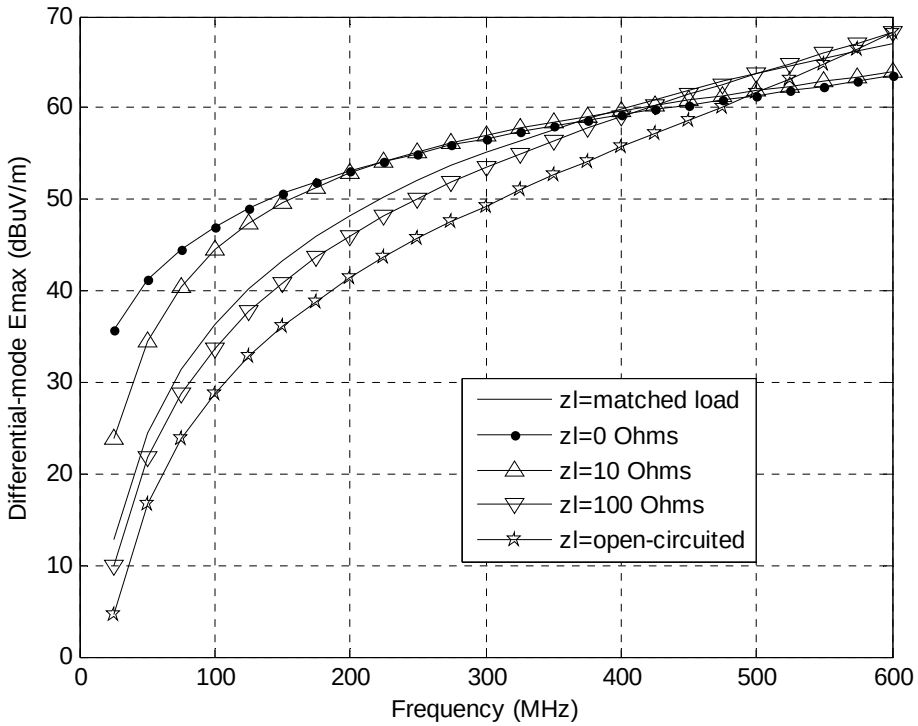

Fig. 4.19 Emax of microstrip line without considering radiation from the attached conductor under different load conditions

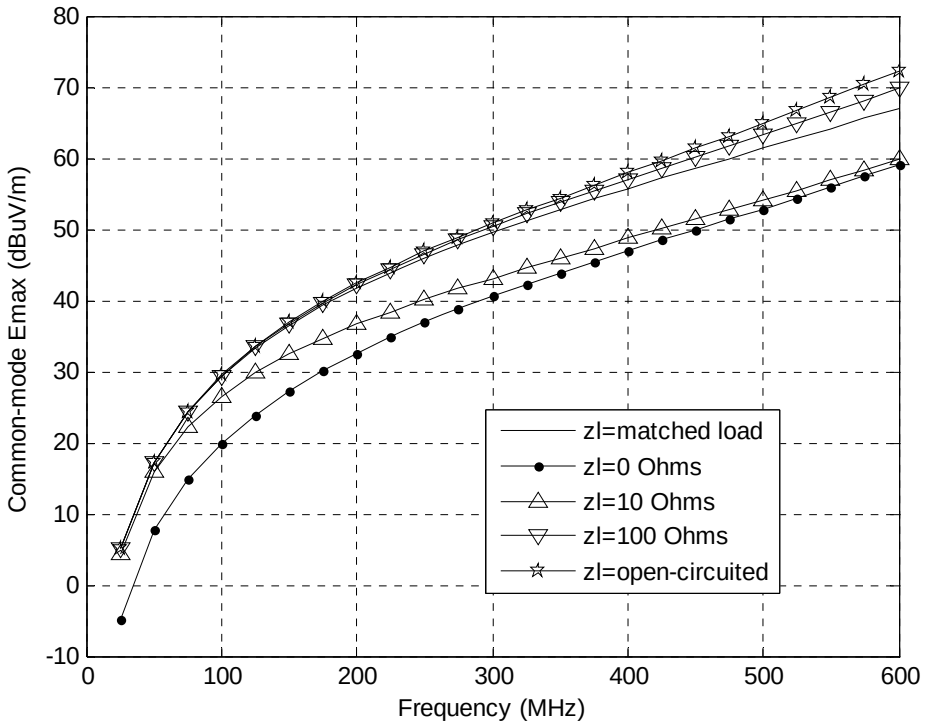

Fig. 4.20 Common-mode Emax from the 100 mm attached conductor without considering the radiation from the microstrip line under different load conditions

4.2.3 Prediction of Maximum Allowable Ground Voltage to Comply with Radiated Emission Limit

The last example here is to illustrate how to make use of ground bounce information to assess possible radiated emission failure for a specific radiated emission limit, for example, the FCC Class B radiated emission limit. A microstrip supported by a 101.6 mm × 5.588 mm × 0.7747 mm substrate ($\varepsilon_r = 4.5$) with a ground plane, as shown in Fig. 4.21, is used as a case study example. The width of the upper trace is 0.508 mm. For numerical modelling purposes, the microstrip structure is subdivided into rectangular cells of equal size, where the dimension of each cell is 5.08 mm by 0.508 mm by 0.38735 mm. To study the effect of ground discontinuity on the ground voltage drop, a

slot of size of $L_s \times W_s$ is cut in the ground plane. Two different ground plane configurations are simulated, one without slot and one with slot. The slot dimension is L_s = 10.16 mm and W_s = 2.54 mm. In all simulations, the excitation source voltage V_S, applied at the source end of the microstrip, is kept constant at 1V for all frequencies.

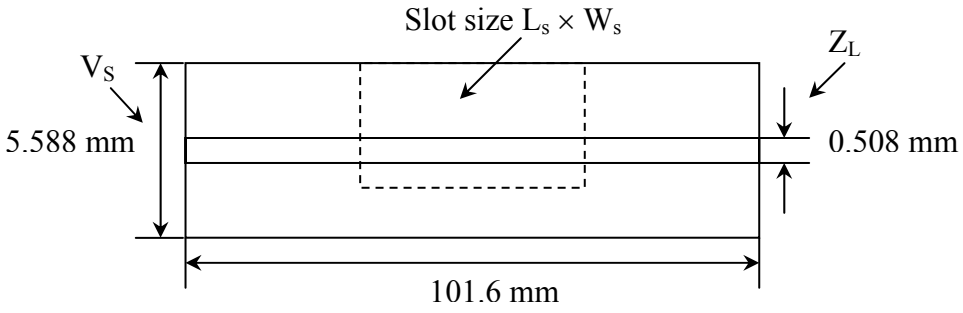

Fig. 4.21 A microstrip line with slot

The load end is terminated by Z_L = 83 Ω, which is the characteristic impedance of the line. The predicted voltage difference between the ground points of the source and the load ends, from 50 MHz to 1 GHz, is plotted in Fig. 4.22. The maximum radiated electric field at 3 m from the microstrip line is also predicted and plotted in Fig. 4.23. As expected, Fig. 4.22 shows that the ground voltage drop (Vg) without slot in the ground plane is the lower among the two different configurations. However, once there is a slot in the ground plane, the return path in the ground plane is disturbed and results in higher ground inductance, which translates to higher ground voltage drop. Fig. 4.23 indicates that maximum radiated electric field (Emax) from the microstrip line structure increases when there is a slot in the ground plane. This is expected as the slot causes larger loop area of the signal delivery path and hence, higher radiated electric field.

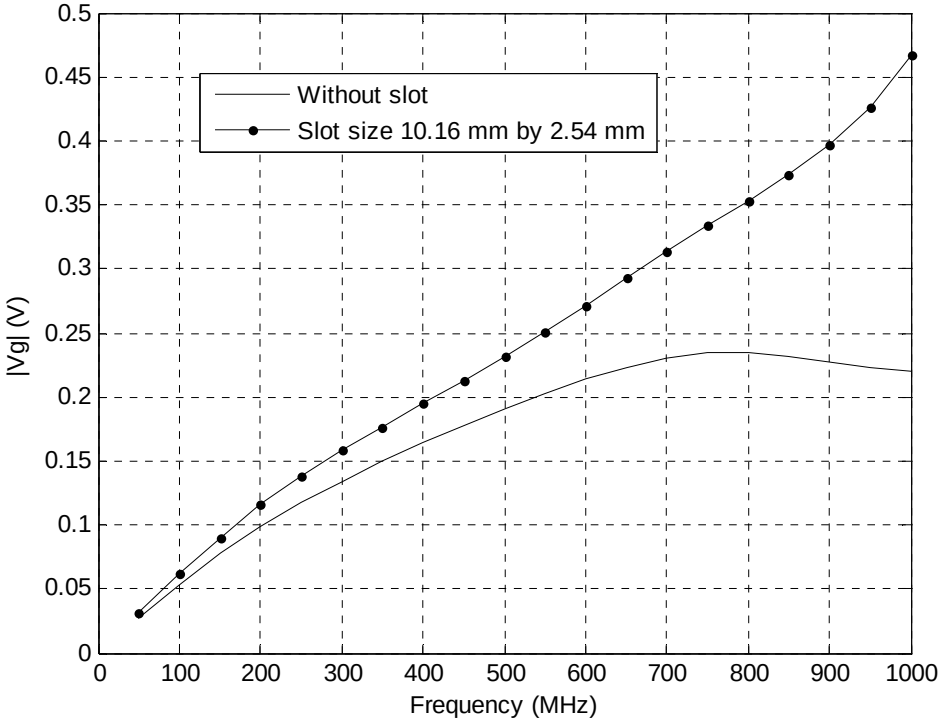

Fig. 4.22 Magnitude of Vg of microstrip line as a function of frequency

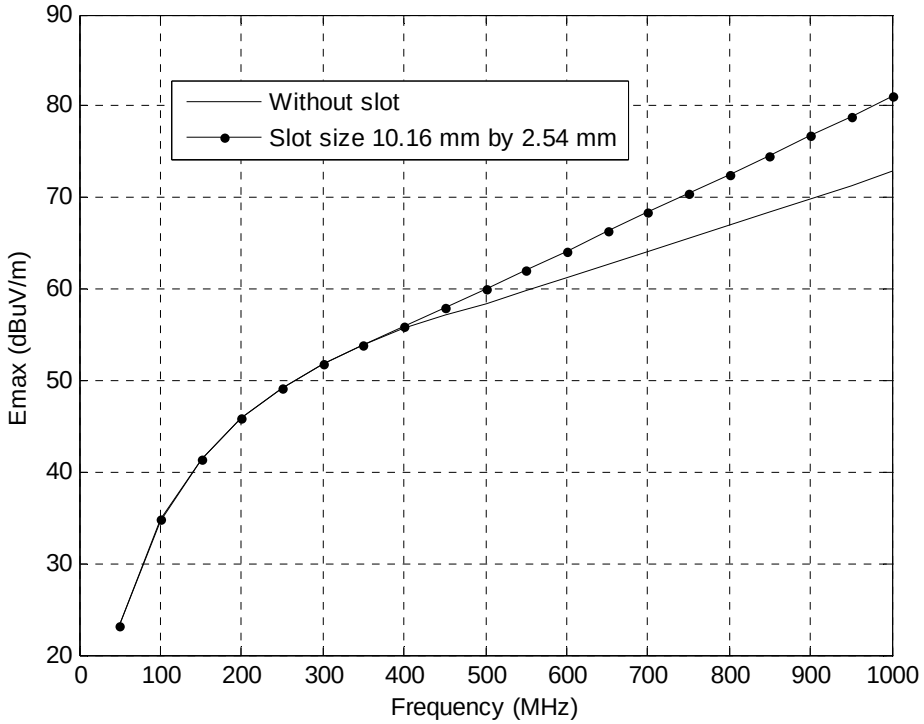

Fig. 4.23 Emax at 3 m from the microstrip line as a function of frequency

The simulated results show that there is a strong correlation between ground voltage drop and radiated electric field for a signal delivery path. As radiated emission from a digital device is regulated by FCC Class B limit [7], one could set the FCC limit as the maximum allowable radiated emission from the signal delivery path and determine the maximum allowable ground voltage drop of the signal delivery path. For example, given the same microstrip structure shown in Fig. 4.21, one could determine the maximum allowable ground voltage limits for the two different ground configurations so as to meet FCC radiated emission limit. The maximum allowable ground voltage limits for the two different ground configurations are calculated and plotted in Fig. 4.24 and Fig. 4.25. For ease of reading, Fig. 4.24 shows the maximum allowable ground voltage limits (Vg,max) from 50 MHz to 500 MHz and Fig. 4.25 shows the maximum allowable ground voltage limit from 500 MHz to 1 GHz.

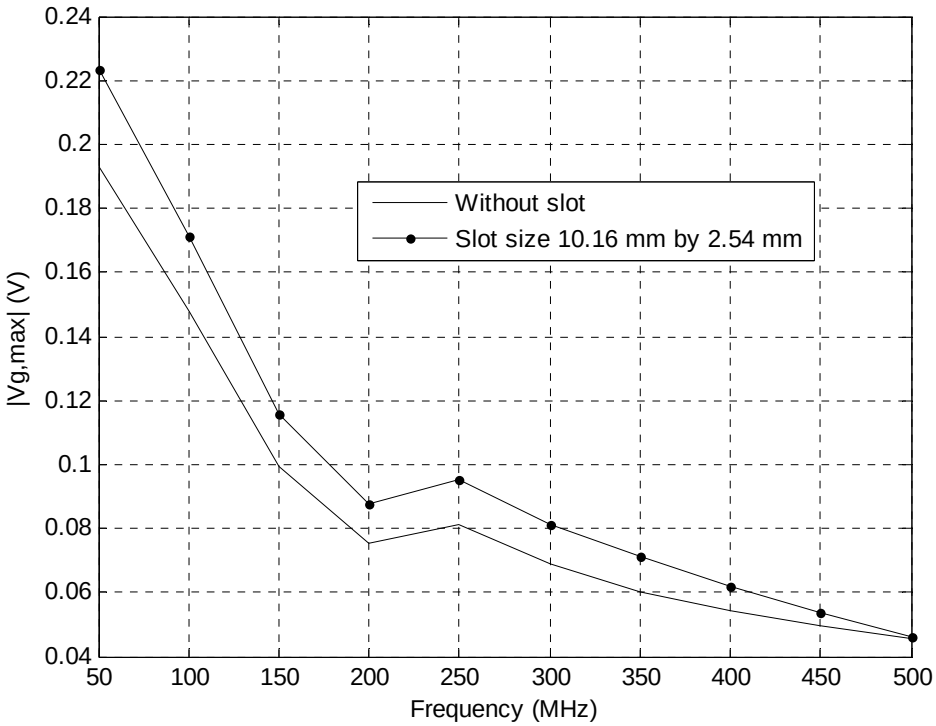

Fig. 4.24 Magnitude of Vg,max (50 MHz to 500 MHz) to meet FCC radiated emission limit

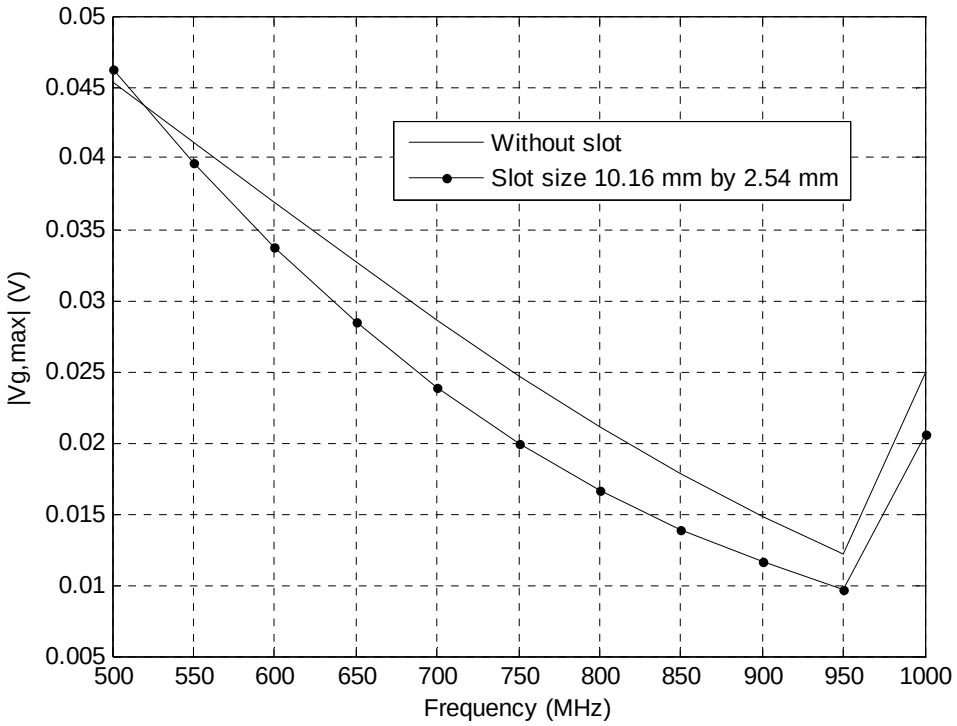

Fig. 4.25 Magnitude of Vg,max (500 MHz to 1 GHz) to meet FCC radiated emission limit

In general, the Vg,max reduces with increasing frequency. Also, above 500 MHz, the slot in the ground plane has made FCC radiated emission compliance tougher because the Vg,max becomes more stringent.

As shown earlier, by given a radiated emission limit, one could predict the maximum allowable ground voltage limit for any signal delivery path on a PCB. With such a limit, one could assess the signal to be delivered to this signal line would likely to cause potential EMI failure. To illustrate the concept, the same microstrip line in will be used as an example. The source end of the line will be fed with a trapezoidal voltage waveform with 50 % duty cycle. For simplicity, it is assumed that both rise and fall times of the waveform are identical. The magnitudes of the harmonics of the trapezoidal waveform can be determined by equation (4.1).

$$|X_n| = \begin{cases} \dfrac{A}{(n\pi)^2 f_o \tau_r} \left|\sin(2n\pi f_o \tau_r)\right| & n \text{ odd} \\ 0 & n \text{ even} \end{cases} \tag{4.1}$$

where A is the amplitude of the trapezoidal, n is the harmonic number, f_o is the fundamental frequency and τ_r is the rise time.

Assume that a trapezoidal waveform with amplitude of 3.3 V and frequency of 50 MHz is fed to the source end of the microstrip line. Two different rise times of 0.625 ns and 1 ns will be used in the simulation to calculate the respective ground voltage as well as maximum radiated electric field Emax. Fig. 4.26 shows the comparison of the ground voltage with maximum allowable ground voltage limit Vg,max. For the waveform with rise time of 0.625 ns, the ground voltage has exceeded Vg,max marginally at around 950 MHz, which indicates that radiated emission from the microstrip line will fail the FCC limit slightly at the said frequency. For the waveform with rise time of 1 ns, the ground voltage is much lower than Vg,max throughout the frequency range. This implies that radiated emission from the same microstrip line will now comply with the FCC limit with good margin.

Fig. 4.27 plots the maximum radiated electric field Emax from the microstrip line for the two different rise times. It confirms the implications based the ground voltage prediction.

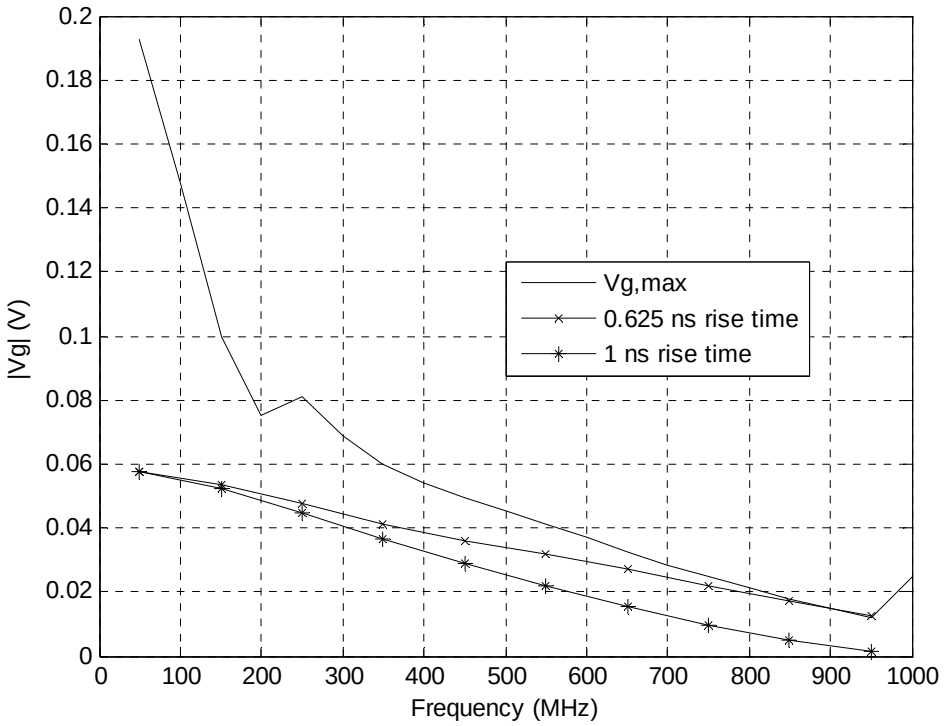

Fig. 4.26 |Vg| of the microstrip line without slot as a function of frequency with a trapezoidal voltage source (3.3 V amplitude and different rise times)

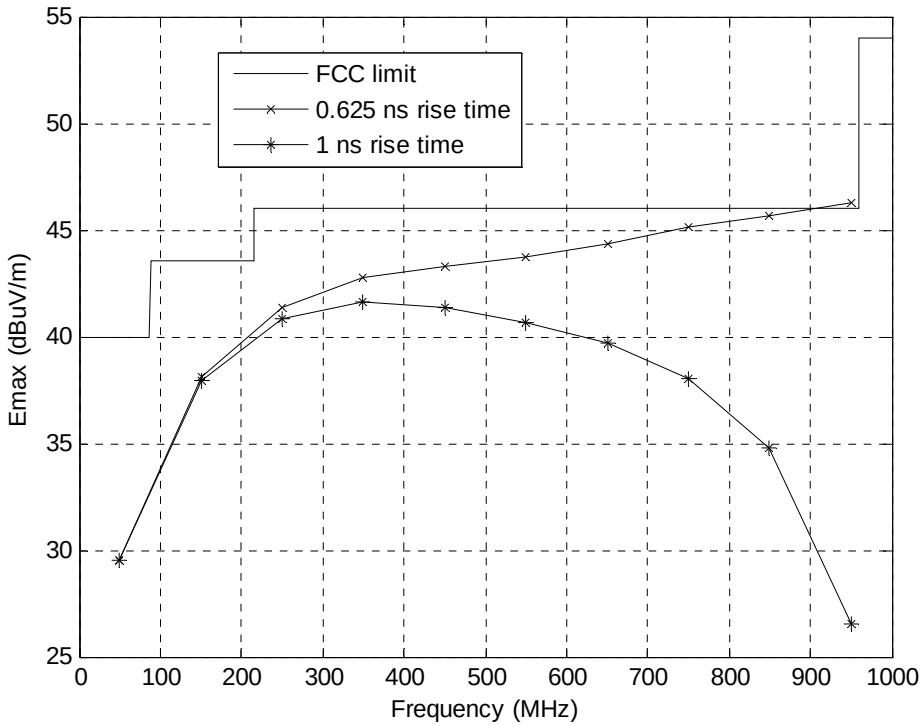

Fig. 4.27 Emax at 3 m from the microstrip line without slot as a function of frequency with trapezoidal voltage source (3.3 V amplitude and different rise times)

Now use the same microstrip line structure but with a slot of size 10.16 mm × 2.54 mm in the ground plane. The same trapezoidal waveform is fed to the microstrip line again. In the case of 0.625 ns rise time, Fig. 4.28 shows that the ground voltage has exceeded Vg,max from 550 MHz onwards. Hence, radiated emission from the microstrip line with the given slot is expected to fail the FCC limit above 550 MHz. In the case of 1 ns rise time, the ground voltage does increase but is still within Vg,max and it implies that radiated emission from the microstrip line with the slot is still below the FCC limit. Fig. 4.29 shows the radiated electric field from the microstrip line with slot for both rise times. Again, it confirms the earlier implications based on the ground voltage prediction.

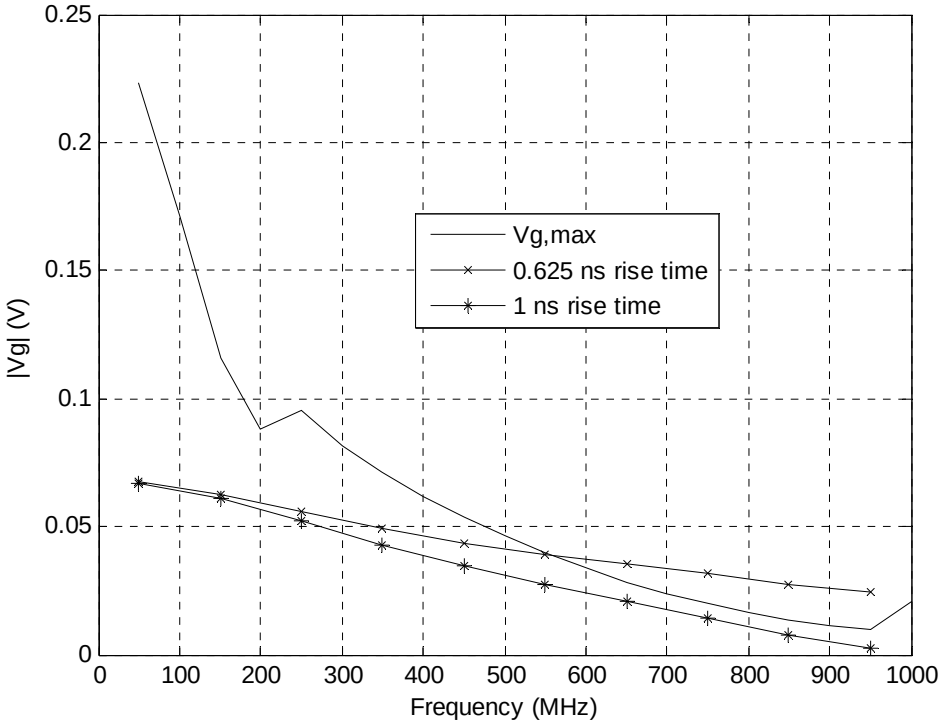

Fig. 4.28 |Vg| of the microstrip line with slot size 10.16 mm by 2.54 mm as a function of frequency with trapezoidal voltage source (3.3 V amplitude and different rise times)

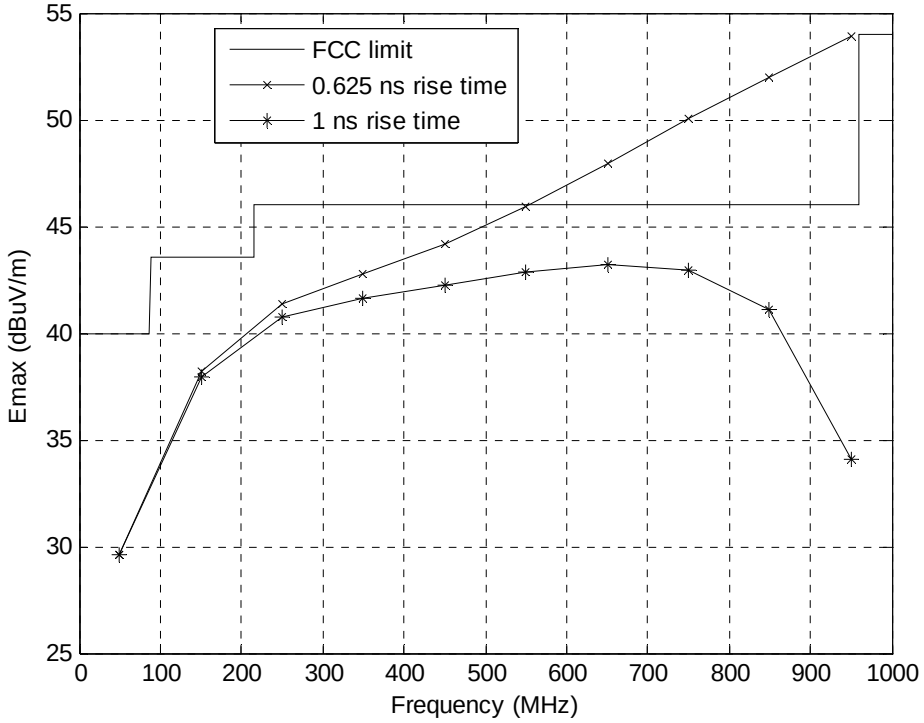

Fig. 4.29 Emax at 3 m from the microstrip line with slot size 10.16 mm by 2.54 mm as a function of frequency with trapezoidal voltage source (3.3 V amplitude and different rise time)

4.3 Conclusion

The extracted full-wave circuit model proposed in this thesis has been validated through comparison with well-established EM solver in the market as well as through experimental data. With the full-wave model, voltage drop between any two points on the interconnecting trace on any PCB could be predicted with ease, which is usually not readily available from commercial EDA tools and EM solvers. The ability of predicting RF voltage drop of any arbitrary printed circuit interconnects opens the doors for many challenging EMI/SI analyses that are either impossible or difficult to be done by many existing tools, such as those three application examples illustrated here.

CHAPTER FIVE

5 CONCLUSIONS AND RECOMMENDED FUTURE WORKS

5.1 Conclusions

Based on full-wave formulation of Maxwell's equation, a extraction code that is capable of extracting full-wave equivalent circuit of any arbitrary printed circuit interconnects with defined geometry and dimension, has been successfully developed and validated.

Bearing in mind the accuracy and computational efficiently of the extraction code, a simplified full-wave model is proposed. The simplified model managed to retain the full-wave accuracy of a comprehensive model but with much reduced circuit elements. Also, to enhance the computational time for the circuit extraction, a semi-analytical approach has been proposed to evaluate the various integrals that are resulted from the electric field integral equations (EFIEs) formulation. The semi-analytical approach not only improves the circuit extraction speed, but most importantly, retains the necessary accuracy needed for the model.

The code has been validated through comparisons with results obtained by well-established commercial EM solver HFSS as well as with experimental results. The ability of the proposed model to predict voltage difference between any two points on the conductor allows many systematic and in-depth board-level EMI/SI analyses to be carried out.

5.2 Recommended Future Works

In the author's opinion, the following future works are worth exploring:

- Typical PCB structures have non-right-angled bend printed circuit traces and circular vias. However, the code developed in this thesis still restricted to printed circuit traces that are rectangular in geometry. In order to model these non-rectangular shapes, other more complicated basis functions should be chosen.

- Current code developed in this thesis cannot read in the geometry of the structure from PCB layout files, the user need to key in the geometry of the structure manually. Hence, interfacing with PCB layout files and the proposed code should be developed so that the PCB layout data could be imported directly for various EMI/SI analyses.

- Good grounding topology is very crucial in PCB design. Design guidelines for different grounding arrangement in PCB layout should be developed. This will enrich the knowledge of the field and also can be useful to others.

APPENDIX

A.1 DEFINITION OF VARIOUS VARIABLES USED IN TABLE 3.2–3.7

The various variables used in Table 3.2 are defined as follows:

$$g_{2D\Pi,m} = f_{2D\Pi,m}(u_2, v_1, w_o) - f_{2D\Pi,m}(u_2, v_2, w_o) - f_{2D\Pi,m}(u_1, v_1, w_o) + f_{2D\Pi,m}(u_1, v_2, w_o) \quad \text{(A.1)}$$

where

$$\begin{aligned} u_1 &= u_o - \frac{\Delta u_j}{2} \quad u_2 = u_o + \frac{\Delta u_j}{2} \\ v_1 &= v_o - \frac{\Delta v_j}{2} \quad v_2 = v_o + \frac{\Delta v_j}{2} \end{aligned} \quad \text{(A.2)}$$

$$f_{2D\Pi,0} \equiv N_1 \quad f_{2D\Pi,1} \equiv N_2 \quad f_{2D\Pi,2} \equiv N_3 \quad \text{(A.3)}$$

The various variables used in Table 3.3 are defined as follows:

$$\begin{aligned} g_{3D\Pi,m} &= f_{3D\Pi,m}(u_2, v_2, w_2) - f_{3D\Pi,m}(u_2, v_2, w_1) - f_{3D\Pi,m}(u_2, v_1, w_2) + f_{3D\Pi,m}(u_2, v_1, w_1) \\ &- f_{3D\Pi,m}(u_1, v_2, w_2) + f_{3D\Pi,m}(u_1, v_2, w_1) + f_{3D\Pi,m}(u_1, v_1, w_2) - f_{3D\Pi,m}(u_1, v_1, w_1) \end{aligned} \quad \text{(A.4)}$$

where

$$\begin{aligned} u_1 &= u_o - \frac{\Delta u_j}{2} \quad u_2 = u_o + \frac{\Delta u_j}{2} \\ v_1 &= v_o - \frac{\Delta v_j}{2} \quad v_2 = v_o + \frac{\Delta v_j}{2} \\ w_1 &= w_o - \frac{\Delta w_j}{2} \quad w_2 = w_o + \frac{\Delta w_j}{2} \end{aligned} \quad \text{(A.5)}$$

$$f_{3D\Pi,0} \equiv N_4 \quad f_{3D\Pi,1} \equiv N_5 \quad f_{3D\Pi,2} \equiv N_6 \tag{A.6}$$

The various variables used in Table 3.4 are defined as follows:

$$\begin{aligned} g_{2D\Lambda r,m} &= f_{2D\Lambda m,1}(u_2,v_1,w_o) - f_{2D\Lambda m,1}(u_2,v_2,w_o) - f_{2D\Lambda m,1}(u_1,v_1,w_o) + f_{2D\Lambda m,1}(u_1,v_2,w_o) \\ &+ \frac{1}{\Delta u_j}\left[f_{2D\Lambda m,2}(u_2,v_1,w_o) - f_{2D\Lambda m,2}(u_2,v_2,w_o) - f_{2D\Lambda m,2}(u_1,v_1,w_o) + f_{2D\Lambda m,2}(u_1,v_2,w_o)\right. \\ &- f_{2D\Lambda m,2}(u_4,v_1,w_o) + f_{2D\Lambda m,2}(u_4,v_2,w_o) + f_{2D\Lambda m,2}(u_3,v_1,w_o) - f_{2D\Lambda m,2}(u_3,v_2,w_o) \\ &- f_{2D\Lambda m,3}(u_2,v_1,w_o) + f_{2D\Lambda m,3}(u_2,v_2,w_o) + f_{2D\Lambda m,3}(u_1,v_1,w_o) - f_{2D\Lambda m,3}(u_1,v_2,w_o) \\ &\left. + f_{2D\Lambda m,3}(u_4,v_1,w_o) - f_{2D\Lambda m,3}(u_4,v_2,w_o) - f_{2D\Lambda m,3}(u_3,v_1,w_o) + f_{2D\Lambda m,3}(u_3,v_2,w_o)\right] \end{aligned} \tag{A.7}$$

where

$$\begin{aligned} &u_o = u_{io} - u_{jo} \quad v_o = v_{io} - v_{jo} \quad v_1 = v_o - \frac{\Delta v_j}{2} \quad v_2 = v_o + \frac{\Delta v_j}{2} \\ &u_1 = u_o - \frac{\Delta u_i}{2} - \frac{\Delta u_j}{2} \quad u_2 = u_o + \frac{\Delta u_i}{2} - \frac{\Delta u_j}{2} \\ &u_3 = u_o - \frac{\Delta u_i}{2} + \frac{\Delta u_j}{2} \quad u_4 = u_o + \frac{\Delta u_i}{2} + \frac{\Delta u_j}{2} \end{aligned} \tag{A.8}$$

$$\begin{aligned} &f_{2D\Lambda 0,1} \equiv N_7 \quad f_{2D\Lambda 0,2} \equiv N_8 \quad f_{2D\Lambda 0,3} \equiv N_9 \\ &f_{2D\Lambda 1,1} \equiv N_{10} \quad f_{2D\Lambda 1,2} \equiv N_{11} \quad f_{2D\Lambda 1,3} \equiv N_{12} \\ &f_{2D\Lambda 2,1} \equiv N_{13} \quad f_{2D\Lambda 2,2} \equiv N_{14} \quad f_{2D\Lambda 2,3} \equiv N_{15} \end{aligned} \tag{A.9}$$

The various variables used in Table 3.5 are defined as follows:

$$\begin{aligned} g_{2D\Lambda f,m} &= f_{2D\Lambda m,1}(u_4,v_2,w_o) - f_{2D\Lambda m,1}(u_4,v_1,w_o) - f_{2D\Lambda m,1}(u_3,v_2,w_o) \\ &+ f_{2D\Lambda m,1}(u_3,v_1,w_o) - \frac{1}{\Delta u_j}\left[f_{2D\Lambda m,2}(u_2,v_1,w_o) - f_{2D\Lambda m,2}(u_2,v_2,w_o)\right. \\ &- f_{2D\Lambda m,2}(u_1,v_1,w_o) + f_{2D\Lambda m,2}(u_1,v_2,w_o) \\ &- f_{2D\Lambda m,2}(u_4,v_1,w_o) + f_{2D\Lambda m,2}(u_4,v_2,w_o) + f_{2D\Lambda m,2}(u_3,v_1,w_o) - f_{2D\Lambda m,2}(u_3,v_2,w_o) \\ &- f_{2D\Lambda m,3}(u_2,v_1,w_o) + f_{2D\Lambda m,3}(u_2,v_2,w_o) + f_{2D\Lambda m,3}(u_1,v_1,w_o) - f_{2D\Lambda m,3}(u_1,v_2,w_o) \\ &\left. + f_{2D\Lambda m,3}(u_4,v_1,w_o) - f_{2D\Lambda m,3}(u_4,v_2,w_o) - f_{2D\Lambda m,3}(u_3,v_1,w_o) + f_{2D\Lambda m,3}(u_3,v_2,w_o)\right] \end{aligned} \tag{A.10}$$

The rest of the variables are defined in equations (A.8)–(A.9).

The various variables used in Table 3.6 are defined as follows:

$$
\begin{aligned}
g_{3D\Lambda r,m} &= \left[f_{3D\Lambda m,1}(u_2,v_1,w_2) - f_{3D\Lambda m,1}(u_2,v_1,w_1) - f_{3D\Lambda m,1}(u_2,v_2,w_2) + f_{3D\Lambda m,1}(u_2,v_2,w_1) \right. \\
&\quad \left. - f_{3D\Lambda m,1}(u_1,v_1,w_2) + f_{3D\Lambda m,1}(u_1,v_1,w_1) + f_{3D\Lambda m,1}(u_1,v_2,w_2) - f_{3D\Lambda m,1}(u_1,v_2,w_1) \right] \\
&\quad - \frac{1}{\Delta u_j} \left[f_{3D\Lambda m,2}(u_2,v_1,w_1) - f_{3D\Lambda m,2}(u_2,v_1,w_2) - f_{3D\Lambda m,2}(u_2,v_2,w_1) + f_{3D\Lambda m,2}(u_2,v_2,w_2) \right. \\
&\quad - f_{3D\Lambda m,2}(u_1,v_1,w_1) + f_{3D\Lambda m,2}(u_1,v_1,w_2) + f_{3D\Lambda m,2}(u_1,v_2,w_1) - f_{3D\Lambda m,2}(u_1,v_2,w_2) \\
&\quad - f_{3D\Lambda m,2}(u_4,v_1,w_1) + f_{3D\Lambda m,2}(u_4,v_1,w_2) + f_{3D\Lambda m,2}(u_4,v_2,w_1) - f_{3D\Lambda m,2}(u_4,v_2,w_2) \\
&\quad \left. + f_{3D\Lambda m,2}(u_3,v_1,w_1) - f_{3D\Lambda m,2}(u_3,v_1,w_2) - f_{3D\Lambda m,2}(u_3,v_2,w_1) + f_{3D\Lambda m,2}(u_3,v_2,w_2) \right] \\
&\quad + \frac{1}{\Delta u_j} \left[f_{3D\Lambda m,3}(u_2,v_1,w_1) - f_{3D\Lambda m,3}(u_2,v_1,w_2) - f_{3D\Lambda m,3}(u_2,v_2,w_1) + f_{3D\Lambda m,3}(u_2,v_2,w_2) \right. \\
&\quad - f_{3D\Lambda m,3}(u_1,v_1,w_1) + f_{3D\Lambda m,3}(u_1,v_1,w_2) + f_{3D\Lambda m,3}(u_1,v_2,w_1) - f_{3D\Lambda m,3}(u_1,v_2,w_2) \\
&\quad - f_{3D\Lambda m,3}(u_4,v_1,w_1) + f_{3D\Lambda m,3}(u_4,v_1,w_2) + f_{3D\Lambda m,3}(u_4,v_2,w_1) - f_{3D\Lambda m,3}(u_4,v_2,w_2) \\
&\quad \left. + f_{3D\Lambda m,3}(u_3,v_1,w_1) - f_{3D\Lambda m,3}(u_3,v_1,w_2) - f_{3D\Lambda m,3}(u_3,v_2,w_1) + f_{3D\Lambda m,3}(u_3,v_2,w_2) \right]
\end{aligned}
\tag{A.11}
$$

where

$$
\begin{aligned}
& u_o = u_{io} - u_{jo} \quad v_o = v_{io} - v_{jo} \quad w_o = w_{io} - w_{jo} \\
& v_1 = v_o - \frac{\Delta v_j}{2} \quad v_2 = v_o + \frac{\Delta v_j}{2} \quad w_1 = w_o - \frac{\Delta w_j}{2} \quad w_2 = w_o + \frac{\Delta w_j}{2} \\
& u_1 = u_o - \frac{\Delta u_i}{2} - \frac{\Delta u_j}{2} \quad u_2 = u_o + \frac{\Delta u_i}{2} - \frac{\Delta u_j}{2} \\
& u_3 = u_o - \frac{\Delta u_i}{2} + \frac{\Delta u_j}{2} \quad u_4 = u_o + \frac{\Delta u_i}{2} + \frac{\Delta u_j}{2}
\end{aligned}
\tag{A.12}
$$

$$
\begin{aligned}
& f_{3D\Lambda 0,1} \equiv N_{16} \quad f_{3D\Lambda 0,2} \equiv N_{17} \quad f_{3D\Lambda 0,3} \equiv N_{18} \\
& f_{3D\Lambda 1,1} \equiv N_{19} \quad f_{3D\Lambda 1,2} \equiv N_{20} \quad f_{3D\Lambda 1,3} \equiv N_{21} \\
& f_{3D\Lambda 2,1} \equiv N_{22} \quad f_{3D\Lambda 2,2} \equiv N_{23} \quad f_{3D\Lambda 2,3} \equiv N_{24}
\end{aligned}
\tag{A.13}
$$

The various variables used in Table 3.7 are defined as follows:

$$
\begin{aligned}
g_{3\mathrm{D}\Lambda f,m} &= \left[f_{3\mathrm{D}\Lambda m,1}(u_4,v_1,w_1) - f_{3\mathrm{D}\Lambda m,1}(u_4,v_1,w_2) - f_{3\mathrm{D}\Lambda m,1}(u_4,v_2,w_1) + f_{3\mathrm{D}\Lambda m,1}(u_4,v_2,w_2)\right. \\
&\left. - f_{3\mathrm{D}\Lambda m,1}(u_3,v_1,w_1) + f_{3\mathrm{D}\Lambda m,1}(u_3,v_1,w_2) + f_{3\mathrm{D}\Lambda m,1}(u_3,v_2,w_1) - f_{3\mathrm{D}\Lambda m,1}(u_3,v_2,w_2)\right] \\
&+ \frac{1}{\Delta u_j}\left[f_{3\mathrm{D}\Lambda m,2}(u_2,v_1,w_1) - f_{3\mathrm{D}\Lambda m,2}(u_2,v_1,w_2) - f_{3\mathrm{D}\Lambda m,2}(u_2,v_2,w_1) + f_{3\mathrm{D}\Lambda m,2}(u_2,v_2,w_2)\right. \\
&- f_{3\mathrm{D}\Lambda m,2}(u_1,v_1,w_1) + f_{3\mathrm{D}\Lambda m,2}(u_1,v_1,w_2) + f_{3\mathrm{D}\Lambda m,2}(u_1,v_2,w_1) - f_{3\mathrm{D}\Lambda m,2}(u_1,v_2,w_2) \\
&- f_{3\mathrm{D}\Lambda m,2}(u_4,v_1,w_1) + f_{3\mathrm{D}\Lambda m,2}(u_4,v_1,w_2) + f_{3\mathrm{D}\Lambda m,2}(u_4,v_2,w_1) - f_{3\mathrm{D}\Lambda m,2}(u_4,v_2,w_2) \\
&\left. + f_{3\mathrm{D}\Lambda m,2}(u_3,v_1,w_1) - f_{3\mathrm{D}\Lambda m,2}(u_3,v_1,w_2) - f_{3\mathrm{D}\Lambda m,2}(u_3,v_2,w_1) + f_{3\mathrm{D}\Lambda m,2}(u_3,v_2,w_2)\right] \\
&- \frac{1}{\Delta u_j}\left[f_{3\mathrm{D}\Lambda m,3}(u_2,v_1,w_1) - f_{3\mathrm{D}\Lambda m,3}(u_2,v_1,w_2) - f_{3\mathrm{D}\Lambda m,3}(u_2,v_2,w_1) + f_{3\mathrm{D}\Lambda m,3}(u_2,v_2,w_2)\right. \\
&- f_{3\mathrm{D}\Lambda m,3}(u_1,v_1,w_1) + f_{3\mathrm{D}\Lambda m,3}(u_1,v_1,w_2) + f_{3\mathrm{D}\Lambda m,3}(u_1,v_2,w_1) - f_{3\mathrm{D}\Lambda m,3}(u_1,v_2,w_2) \\
&- f_{3\mathrm{D}\Lambda m,3}(u_4,v_1,w_1) + f_{3\mathrm{D}\Lambda m,3}(u_4,v_1,w_2) + f_{3\mathrm{D}\Lambda m,3}(u_4,v_2,w_1) - f_{3\mathrm{D}\Lambda m,3}(u_4,v_2,w_2) \\
&\left. + f_{3\mathrm{D}\Lambda m,3}(u_3,v_1,w_1) - f_{3\mathrm{D}\Lambda m,3}(u_3,v_1,w_2) - f_{3\mathrm{D}\Lambda m,3}(u_3,v_2,w_1) + f_{3\mathrm{D}\Lambda m,3}(u_3,v_2,w_2)\right]
\end{aligned}
\tag{A.14}
$$

The full mathematical expressions of all the functions in equations (A.3), (A.6), (A.9) and (A.13) can be found in Appendix A.2.

The rest of the variables are defined in equations (A.12)–(A.13).

A.2 FULL EXPRESSIONS OF VARIOUS INTEGRATIONS

The full expressions of all the functions in equations (A.3), (A.6), (A.9) and (A.13) are listed here. For ease of expressing the individual terms, the definition of R is given by

$$R = \sqrt{u^2 + v^2 + w^2}$$

$$N_1(u,v,w) = \iint \frac{1}{R} du dv = v \tanh^{-1} \frac{u}{R} + u \tanh^{-1} \frac{v}{R} - w \tan^{-1} \frac{uv}{wR}$$

$$N_2(u,v,w) = \iint R du dv$$
$$= \frac{1}{6} v\left(v^2 + 3w^2\right) \tanh^{-1} \frac{u}{R} + \frac{1}{6} u\left(u^2 + 3w^2\right) \tanh^{-1} \frac{v}{R} - \frac{1}{3} w^3 \tan^{-1} \frac{uv}{wR} + \frac{1}{3} uvR$$

$$N_3(u,v,w) = \iint R^3 du dv = \frac{7}{40} uvR^3 + \frac{11}{40} uvw^2 R - \frac{1}{5} w^5 \tan^{-1} \frac{uv}{wR}$$
$$+ \frac{1}{40} v\left(3v^4 + 10v^2 w^2 + 15w^4\right) \tanh^{-1} \frac{u}{R} + \frac{1}{40} u\left(3u^4 + 10u^2 w^2 + 15w^4\right) \tanh^{-1} \frac{v}{R}$$

$$N_4(u,v,w) = \iiint \frac{1}{R} du dv dw = vw \tanh^{-1} \frac{u}{R} + uw \tanh^{-1} \frac{v}{R} + uv \tanh^{-1} \frac{w}{R}$$
$$- \frac{u^2}{2} \tan^{-1} \frac{vw}{uR} - \frac{v^2}{2} \tan^{-1} \frac{uw}{vR} - \frac{w^2}{2} \tan^{-1} \frac{uv}{wR}$$

$$N_5(u,v,w) = \iiint R du dv dw = \frac{1}{6} vw\left(v^2 + w^2\right) \tanh^{-1} \frac{u}{R} + \frac{1}{6} uw\left(u^2 + w^2\right) \tanh^{-1} \frac{v}{R}$$
$$+ \frac{1}{6} uv\left(u^2 + v^2\right) \tanh^{-1} \frac{w}{R} - \frac{1}{12} u^4 \tan^{-1} \frac{vw}{uR} - \frac{1}{12} v^4 \tan^{-1} \frac{uw}{vR} - \frac{1}{12} w^4 \tan^{-1} \frac{uv}{wR} + \frac{1}{4} uvwR$$

$$N_6(u,v,w)=\iiint R^3\,dudvdw=\frac{1}{120}vw\left(9v^4+10v^2w^2+9w^4\right)\tanh^{-1}\frac{u}{R}$$
$$+\frac{1}{120}uw\left(9u^4+10u^2w^2+9w^4\right)\tanh^{-1}\frac{v}{R}+\frac{1}{120}uv\left(9u^4+10u^2v^2+9v^4\right)\tanh^{-1}\frac{w}{R}$$
$$-\frac{1}{30}u^6\tan^{-1}\frac{vw}{uR}-\frac{1}{30}v^6\tan^{-1}\frac{uw}{vR}-\frac{1}{30}w^6\tan^{-1}\frac{uv}{wR}+\frac{2}{15}uvwR^3$$

$$N_7(u,v,w)=\iiint\frac{1}{R}\,dudvdu=uv\tanh^{-1}\frac{u}{R}+\frac{1}{2}\left(u^2-w^2\right)\tanh^{-1}\frac{v}{R}-uw\tan^{-1}\frac{uv}{wR}-\frac{1}{2}vR$$

$$N_8(u,v,w)=\int u\iint\frac{1}{R}\,dudvdu$$
$$=\frac{1}{12}v\left(6u^2+v^2+3w^2\right)\tanh^{-1}\frac{u}{R}+\frac{1}{3}u^3\tanh^{-1}\frac{v}{R}-\frac{1}{6}w\left(3u^2+w^2\right)\tan^{-1}\frac{uv}{wR}-\frac{1}{12}uvR$$

$$N_9(u,v,w)=\iiint\frac{u}{R}\,dudvdu$$
$$=\frac{1}{6}v\left(v^2+3w^2\right)\tanh^{-1}\frac{u}{R}+\frac{1}{6}u\left(u^2+3w^2\right)\tanh^{-1}\frac{v}{R}-\frac{1}{3}w^3\tan^{-1}\frac{uv}{wR}+\frac{1}{3}uvR$$

$$N_{10}(u,v,w)=\iiint R\,dudvdu=\frac{1}{6}uv\left(v^2+3w^2\right)\tanh^{-1}\frac{u}{R}+\frac{1}{24}\left(u^4+6u^2w^2-3w^4\right)\tanh^{-1}\frac{v}{R}$$
$$+\frac{1}{8}vR^3-\frac{1}{24}v\left(5v^2+8w^2\right)R-\frac{1}{3}uw^3\tan^{-1}\frac{uv}{wR}$$

$$N_{11}(u,v,w)=\int u\iint R\,dudvdu=\frac{1}{240}v\left(20u^2v^2+3v^4+10v^2w^2+60u^2w^2+15w^4\right)\tanh^{-1}\frac{u}{R}$$
$$+\frac{1}{30}u^3\left(u^2+5w^2\right)\tanh^{-1}\frac{v}{R}-\frac{1}{30}w^3\left(5u^2+w^2\right)\tan^{-1}\frac{uv}{wR}+\frac{11}{120}uvR^3-\frac{1}{240}uv\left(25v^2+29w^2\right)R$$
$$N_{12}(u,v,w)=\iiint uR\,dudvdu=\frac{7}{120}uvR^3+\frac{11}{120}uvw^2R-\frac{1}{15}w^5\tan^{-1}\frac{uv}{wR}$$
$$+\frac{1}{120}v\left(3v^4+10v^2w^2+15w^4\right)\tanh^{-1}\frac{u}{R}+\frac{1}{120}u\left(3u^4+10u^2w^2+15w^4\right)\tanh^{-1}\frac{v}{R}$$

$$N_{13}(u,v,w)=\iiint R^3\,dudvdu$$
$$=\frac{1}{40}uv\left(3v^4+10v^2w^2+15w^4\right)\tanh^{-1}\frac{u}{R}+\frac{1}{80}\left(u^6+5u^4w^2+15u^2w^4-5w^6\right)\tanh^{-1}\frac{v}{R}$$
$$-\frac{1}{5}uw^5\tan^{-1}\frac{uv}{wR}+\frac{3}{80}vR^5-\frac{1}{120}v\left(v^2-12w^2\right)R^3-\frac{1}{80}v\left(5v^4+22v^2w^2+22w^4\right)R$$

$$N_{14}(u,v,w)=\int u\iint R^3\,dudvdu$$
$$=\frac{1}{1120}v\left(42u^2v^4+140u^2v^2w^2+210u^2w^4+5v^6+21v^4w^2+35v^2w^4+35w^6\right)\tanh^{-1}\frac{u}{R}$$
$$+\frac{1}{280}u^3\left(3u^4+14u^2w^2+35w^4\right)\tanh^{-1}\frac{v}{R}-\frac{1}{70}w^5\left(7u^2+w^2\right)\tan^{-1}\frac{uv}{wR}$$
$$+\frac{13}{420}uvR^5-\frac{1}{840}uv\left(11v^2-55w^2\right)R^3-\frac{1}{1120}uv\left(25v^4+144v^2w^2+127w^4\right)R$$

$$N_{15}(u,v,w)=\iiint uR^3\,dudvdu=\frac{1}{560}v\left(5v^6+21v^4w^2+35v^2w^4+35w^6\right)\tanh^{-1}\frac{u}{R}$$
$$+\frac{1}{560}u\left(5u^6+21u^4w^2+35u^2w^4+35w^6\right)\tanh^{-1}\frac{v}{R}$$
$$-\frac{1}{35}w^7\tan^{-1}\frac{uv}{wR}+\frac{41}{1680}uvR^5+\frac{11}{1680}uv\left(52u^2w^2-30u^2v^2+52v^2w^2+133w^4\right)R$$

$$N_{16}(u,v,w)=\int\iiint\frac{1}{R}\,dudvdwdu=uvw\tanh^{-1}\frac{u}{R}+\frac{1}{6}w\left(3u^2-w^2\right)\tanh^{-1}\frac{v}{R}$$
$$+\frac{1}{6}v\left(3u^2-v^2\right)\tanh^{-1}\frac{w}{R}-\frac{1}{6}u^3\tan^{-1}\frac{vw}{uR}-\frac{1}{2}uv^2\tan^{-1}\frac{uw}{vR}-\frac{1}{2}uw^2\tan^{-1}\frac{uv}{wR}-\frac{1}{3}vwR$$

$$N_{17}(u,v,w)=\int u\iiint\frac{1}{R}\,dudvdwdu=\frac{1}{12}vw\left(6u^2+v^2+w^2\right)\tanh^{-1}\frac{u}{R}+\frac{1}{3}u^3w\tanh^{-1}\frac{v}{R}$$
$$+\frac{1}{3}u^3v\tanh^{-1}\frac{w}{R}-\frac{1}{8}u^4\tan^{-1}\frac{vw}{uR}-\frac{1}{24}v^2\left(6u^2+v^2\right)\tan^{-1}\frac{uw}{vR}-\frac{1}{24}w^2\left(6u^2+w^2\right)\tan^{-1}\frac{uv}{wR}$$
$$-\frac{1}{24}uvwR$$

$$N_{18}(u,v,w)=\int\iiint\frac{u}{R}\,dudvdwdu=\frac{1}{6}vw\left(v^2+w^2\right)\tanh^{-1}\frac{u}{R}+\frac{1}{6}uw\left(u^2+w^2\right)\tanh^{-1}\frac{v}{R}$$
$$+\frac{1}{6}uv\left(u^2+v^2\right)\tanh^{-1}\frac{w}{R}-\frac{1}{12}u^4\tan^{-1}\frac{vw}{uR}-\frac{1}{12}v^4\tan^{-1}\frac{uw}{vR}-\frac{1}{12}w^4\tan^{-1}\frac{uv}{wR}+\frac{1}{4}uvwR$$

$$N_{19}(u,v,w)=\int\iiint R\,dudvdwdu=\frac{1}{6}uvw\left(v^2+w^2\right)\tanh^{-1}\frac{u}{R}$$
$$+\frac{1}{120}w\left(5u^4+10u^2w^2-3w^4\right)\tanh^{-1}\frac{v}{R}+\frac{1}{120}v\left(5u^4+10u^2v^2-3v^4\right)\tanh^{-1}\frac{w}{R}$$
$$-\frac{1}{60}u^5\tan^{-1}\frac{vw}{uR}-\frac{1}{12}uv^4\tan^{-1}\frac{uw}{vR}-\frac{1}{12}uw^4\tan^{-1}\frac{uv}{wR}+\frac{1}{10}vwR^3-\frac{19}{120}vw\left(v^2+w^2\right)R$$

$$N_{20}(u,v,w)=\int u\iiint R\,du\,dv\,dw\,du$$
$$=\frac{1}{720}vw\left(60u^2v^2+9v^4+10v^2w^2+60u^2w^2+9w^4\right)\tanh^{-1}\frac{u}{R}+\frac{1}{90}u^3w\left(3u^2+5w^2\right)\tanh^{-1}\frac{v}{R}$$
$$+\frac{1}{90}u^3v\left(3u^2+5v^2\right)\tanh^{-1}\frac{w}{R}-\frac{1}{72}u^6\tan^{-1}\frac{vw}{uR}-\frac{1}{360}v^4\left(15u^2+2v^2\right)\tan^{-1}\frac{uw}{vR}$$
$$-\frac{1}{360}w^4\left(15u^2+2w^2\right)\tan^{-1}\frac{uv}{wR}+\frac{13}{180}uvwR^3-\frac{19}{240}uvw\left(v^2+w^2\right)R$$

$$N_{21}(u,v,w)=\int\iiint uR\,du\,dv\,dw\,du=\frac{1}{360}vw\left(9v^4+10v^2w^2+9w^4\right)\tanh^{-1}\frac{u}{R}$$
$$+\frac{1}{360}uw\left(9u^4+10u^2w^2+9w^4\right)\tanh^{-1}\frac{v}{R}+\frac{1}{360}uv\left(9u^4+10u^2v^2+9v^4\right)\tanh^{-1}\frac{w}{R}$$
$$-\frac{1}{90}u^6\tan^{-1}\frac{vw}{uR}-\frac{1}{90}v^6\tan^{-1}\frac{uw}{vR}-\frac{1}{90}w^6\tan^{-1}\frac{uv}{wR}+\frac{2}{45}uvwR^3$$

$$N_{22}(u,v,w)=\int\iiint R^3\,du\,dv\,dw\,du=\frac{1}{120}uvw\left(9v^4+10v^2w^2+9w^4\right)\tanh^{-1}\frac{u}{R}$$
$$+\frac{1}{1680}w\left(21u^6+35u^4w^2+63u^2w^4-15w^6\right)\tanh^{-1}\frac{v}{R}$$
$$+\frac{1}{1680}v\left(21u^6+35u^4v^2+63u^2v^4-15v^6\right)\tanh^{-1}\frac{w}{R}$$
$$-\frac{1}{210}u^7\tan^{-1}\frac{vw}{uR}-\frac{1}{30}uv^6\tan^{-1}\frac{uw}{vR}-\frac{1}{30}uw^6\tan^{-1}\frac{uv}{wR}$$
$$+\frac{5}{168}vwR^5-\frac{1}{168}vw\left(v^2+w^2\right)R^3-\frac{1}{560}vw\left(27v^4+44v^2w^2+27w^4\right)R$$

$$N_{23}(u,v,w)=\int u\iiint R^3\,du\,dv\,dw\,du$$
$$=\frac{1}{3360}vw\left(126u^2v^4+140u^2v^2w^2+126u^2w^4+15v^6+21v^4w^2+21v^2w^4+15w^6\right)\tanh^{-1}\frac{u}{R}$$
$$+\frac{1}{840}u^3w\left(9u^4+14u^2w^2+21w^4\right)\tanh^{-1}\frac{v}{R}+\frac{1}{840}u^3v\left(9u^4+14u^2v^2+21v^4\right)\tanh^{-1}\frac{w}{R}$$
$$-\frac{1}{240}u^8\tan^{-1}\frac{vw}{uR}-\frac{1}{1680}v^6\left(28u^2+3v^2\right)\tan^{-1}\frac{uw}{vR}-\frac{1}{1680}w^6\left(28u^2+3w^2\right)\tan^{-1}\frac{uv}{wR}$$
$$+\frac{41}{1680}uvwR^5-\frac{17}{1680}uvw\left(v^2+w^2\right)R^3-\frac{1}{1120}uvw\left(19v^4+36v^2w^2+19w^4\right)R$$

$$N_{24}(u,v,w) = \int\int\int\int uR^3 dudvdwdu = \frac{1}{560}vw\left(5v^6 + 7v^4w^2 + 7v^2w^4 + 5w^6\right)\tanh^{-1}\frac{u}{R}$$
$$+\frac{1}{560}uw\left(5u^6 + 7u^4w^2 + 7u^2w^4 + 5w^6\right)\tanh^{-1}\frac{v}{R}$$
$$+\frac{1}{560}uv\left(5u^6 + 7u^4v^2 + 7u^2v^4 + 5v^6\right)\tanh^{-1}\frac{w}{R}$$
$$-\frac{1}{280}u^8\tan^{-1}\frac{vw}{uR} - \frac{1}{280}v^8\tan^{-1}\frac{uw}{vR} - \frac{1}{280}w^8\tan^{-1}\frac{uv}{wR}$$
$$+\frac{2}{105}uvwR^5 - \frac{1}{70}uvw\left(u^2v^2 + u^2w^2 + v^2w^2\right)R$$

A.3 N-POINT QUADRATURE INTEGRATION

Since the weights are symmetrical, the N-point quadrature double integration can be written as follow

$$Q = \sum_{i=1}^{N/2}\sum_{j=1}^{N/2} w_i w_j \left[f\left(x_i, x_j\right) + f\left(x_{N-i+1}, x_j\right) + f\left(x_i, x_{N-j+1}\right) + f\left(x_{N-i+1}, x_{N-j+1}\right)\right]$$

The N-point quadrature triple integration can be written as follow

$$\begin{aligned} Q = \sum_{i=1}^{N/2}\sum_{j=1}^{N/2}\sum_{k=1}^{N/2} w_i w_j w_k \Big[& f\left(x_i, x_j, x_k\right) + f\left(x_{N-i+1}, x_j, x_k\right) \\ & + f\left(x_i, x_{N-j+1}, x_k\right) + f\left(x_{N-i+1}, x_{N-j+1}, x_k\right) \\ & + f\left(x_i, x_j, x_{N-k+1}\right) + f\left(x_{N-i+1}, x_j, x_{N-k+1}\right) \\ & + f\left(x_i, x_{N-j+1}, x_{N-k+1}\right) + f\left(x_{N-i+1}, x_{N-j+1}, x_{N-k+1}\right)\Big] \end{aligned}$$

The N-point quadrature quadruple integration can be written as follow

$$
\begin{aligned}
Q = \sum_{i=1}^{N/2}\sum_{j=1}^{N/2}\sum_{k=1}^{N/2}\sum_{l=1}^{N/2} w_i w_j w_k w_l \Big[& f\left(x_i, x_j, x_k, x_l\right) + f\left(x_{N-i+1}, x_j, x_k, x_l\right) \\
& + f\left(x_i, x_{N-j+1}, x_k, x_l\right) + f\left(x_{N-i+1}, x_{N-j+1}, x_k, x_l\right) \\
& + f\left(x_i, x_j, x_{N-k+1}, x_l\right) + f\left(x_{N-i+1}, x_j, x_{N-k+1}, x_l\right) \\
& + f\left(x_i, x_{N-j+1}, x_{N-k+1}, x_l\right) + f\left(x_{N-i+1}, x_{N-j+1}, x_{N-k+1}, x_l\right) \\
& + f\left(x_i, x_j, x_k, x_{N-l+1}\right) + f\left(x_{N-i+1}, x_j, x_k, x_{N-l+1}\right) \\
& + f\left(x_i, x_{N-j+1}, x_k, x_{N-l+1}\right) + f\left(x_{N-i+1}, x_{N-j+1}, x_k, x_{N-l+1}\right) \\
& + f\left(x_i, x_j, x_{N-k+1}, x_{N-l+1}\right) + f\left(x_{N-i+1}, x_j, x_{N-k+1}, x_{N-l+1}\right) \\
& f\left(x_i, x_{N-j+1}, x_{N-k+1}, x_{N-l+1}\right) + f\left(x_{N-i+1}, x_{N-j+1}, x_{N-k+1}, x_{N-l+1}\right) \Big]
\end{aligned}
$$

where w_i, w_j, w_k and w_l are the weights, x_i, x_j, x_k and x_l are the abscissas and $f()$ is the function to be integrated.

AUTHOR'S PUBLICATIONS

International Journal Papers

1. **E. K. Chua** and K. Y. See, "Full-wave equivalent circuit model for 2D conductor," *IEE Electronics Letter*, Vol. 39, No. 19, pp. 1367–1369, Sep. 2003.
2. **E. K. Chua**, K. Y. See, Z. H. Liu, "Accurate and efficient computation of MoM matrix involving 2D triangular basis function with line matching," *Int. Journal of Computational Methods*. Vol. 3, No. 3, pp. 355–370, Sep. 2006.

Conference Papers

1. **E. K. Chua**, K. Y. See and Z. Liu, "Modeling RF voltage drop of printed circuit interconnects using a full-wave approach," *17th International Zurich Symposium on Electromagnetic Compatibility*, pp. 332-335, Mar. 2006.
2. **E. K. Chua**, K. Y. See, E. P. Li and W. Y. Chang, "Investigation of relationship between ground bounce and common-mode radiation," *IEEE Electronics Packaging Technology Conference*, pp. 610-614, Dec. 2006.
3. K. Y. See and **E. K. Chua**, "SPICE-compatible full-wave equivalent circuit model for interconnect structures," *IEEE Electronics Packaging Technology Conference*, pp. 168-170, Dec. 2003.

4. K. Y. See, **E. K. Chua** and Y. Zhao, "Modeling common-mode radiation from high-speed PCB using method of moment," *IEEE Electronics Packaging Technology Conference*, pp. 523-525, Dec. 2003.
5. K. Y. See, **E. K. Chua** and Z. Liu, "Prediction of RF ground voltage drop using a full-wave approach," *International Symposium on Electromagnetic Compatibility*, Vol. 3, pp. 712-717, Aug. 2006.
6. K. Y. See, **E. K. Chua** and Z. Liu, "Full wave modeling of RF voltage drop on printed circuit interconnects," *1st Electronics Systemintegration Technology Conference*, Sep. 2006.
7. Z. Liu, K. Y. See, E. P. Li and **E. K. Chua**, "Crosstalk Analysis in Frequency and Time Domain Using FDTD-VF Method," *IEEE Electronics Packaging Technology Conference*, pp. 167-170, Dec. 2005.
8. Z. Liu, K. Y. See, E. P. Li and **E. K. Chua**, "An Efficient Approach for the Power/Ground Plane Equivalent Circuit Extraction," *17th Int. Zurich Sym. on EMC*, pp. 379-382, Mar. 2006.

BIBLIOGRAPHY

[1] B. Keiser, *Principles of electromagnetic compatibility*, 3rd ed., Artech House, 1987.

[2] R. Perez, *Handbook of electromagnetic compatibility*. San Diego, Academic Press, 1995.

[3] M. T. Frederick, V. I. Michel and K. Torbjörn, *EMC analysis methods and computational models*. John Wiley & Sons, 1997.

[4] W. C. Bosshart, *Printed circuit boards design and technology*. Tata, McGraw-Hill, 1983.

[5] B. Archambeault, *PCB design for real-world EMI control*. Kluwer Academic Publishers, 2002.

[6] B. Archambeault, *EMI/EMC computational modeling handbook*, 2nd ed., Kluwer Academic Publishers, 2001.

[7] *FCC title 47 part 15, 18 and 68 of the US code of Federal regulations*, Federal Communications Commission, Washington DC.

[8] *Limits and methods of measurement of radio interference characteristics of information technology equipment*, CISPR Publication 22, 1985.

[9] S. Yoshida and H. Tohya, "Novel decoupling circuit enabling notable electromagnetic noise suppression and high-density packaging in a digital printed circuit board," *IEEE Int. Symp. Electromagnetic Compatibility*, Vol. 2, pp. 641-646, 1998.

[10] C. R. Paul, "A comparison of the contributions of common-mode and differential-mode currents in radiated emissions," *IEEE Trans. Electromagnetic Compatibility*, Vol. 31, No. 2, pp. 189-193, May 1989.

[11] J. L. Drewniak, S. Fei, T. P. VanDoren, T. H. Hubing and J. Shaw, "Diagnosing and modeling common-mode radiation from printed circuit boards with attached cables," *IEEE Int. Symp. Electromagnetic Compatibility, Symposium Record*, pp. 465-470, 1995.

[12] J. L. Drewniak, T. H. Hubing and T. P. VanDoren, "Investigation of fundamental mechanisms of common-mode radiation from printed circuit boards with attached cables," *IEEE Int. Symp. Electromagnetic Compatibility*, pp. 110-115, August 1994.

[13] D. M. Hockanson, J. L. Drewniak, T. H. Hubing, T. P. VanDoren, S. Fei and M. J. Wilhelm, "Investigation of fundamental EMI source mechanisms driving common-mode radiation from printed circuit boards with attached cables," *IEEE Trans. Electromagnetic Compatibility,* Vol. 38, No. 4, pp. 557-566, Nov 1996.

[14] C. F. M. **C**arobbi, L. M. Millanta and M**.** Polignano, "Common-mode emissions from printed circuit boards simplified models, analysis and experiments," *IEEE Int. Symp. Electromagnetic Compatibility,* Vol. 2, pp. 806-810, 1999.

[15] D. M. Hockanson, J. L. Drewniak, T. H. Hubing and T. P. VanDoren, "FDTD modeling of common-mode radiation from cables," *IEEE Trans. Electromagnetic Compatibility*, Vol. 38, No. 3, pp. 376-387, Aug 1996.

[16] Hockanson D. M., Drewniak J. L., Hubing T. H. and VanDoren T. P., "FDTD modeling of thin wires for simulating common-mode radiation from

structures with attached cables," *IEEE Int. Symp. Electromagnetic Compatibility*, pp. 168-173, 1995.

[17] D. M. Hockanson, C. W. Lam, J. L. Drewniak, T. H. Hubing and T. P. VanDoren, "Experimental and numerical investigations of fundamental radiation mechanisms in PCB designs with attached cables", *IEEE Int. Symp. Electromagnetic Compatibility*, pp. 305-310, 1996.

[18] X. Ye, J. Nadolny, J. L. Drewniak, T. H. Hubing, T. P. VanDoren & D. E. DuBroff, "EMI associated with inter-board connection for module-on-backplane and stacked-card configurations," *IEEE Int. Symp. Electromagnetic Compatibility*, Vol. 2, pp. 797-802, 1999.

[19] X. Ye, D. M. Hockanson and J. L. Drewniak, "A common-mode current measurement technique for EMI performance evaluation of PCB structures," *Asia-Pacific Conf. Environmental Electromagnetics*, pp. 389-394, May 2000.

[20] D. M. Hockanson, X. Ye, J. L. Drewniak, T. H. Hubing, T. P. VanDoren and R. E. DuBroff, "FDTD and experimental investigation of EMI from stacked-card PCB configurations," *IEEE Trans. Electromagnetic Compatibility*, Vol. 43, No. 1, pp. 1-9, Feb. 2001.

[21] X. Ye, J. Nadolny, J. L. Drewniak, R. E. DuBroff, T. P. VanDoren and T. H. Hubing, "Experimental and FDTD study of the EMI performance of an open-pin-field connector for modules-on-backplanes," *IEEE Int. Symp. Electromagnetic Compatibility*, Vol. 2, pp. 789-794, 2000.

[22] D. Berg, M. Tanaka, Y. Ji, X. Ye, J. L. Drewniak, T. H. Hubing, R. E. DuBroff and T. P. VanDoren, "FDTD and FEM/MOM modeling of EMI

resulting from a trace near a PCB edge," *IEEE Int. Symp. Electromagnetic Compatibility*, Vol. 1, pp. 135-140, 2000.

[23] W. Cui, M. Li, X. Luo, J. L. Drewniak, T. H. Hubing, T. P. VanDoren and R. E. DuBroff, "Anticipating EMI from coupling between high-speed digital and I/O lines," *IEEE Int. Symp. Electromagnetic Compatibility*, Vol. 1, pp. 189-194, 1999.

[24] W. Cui, H. Shi, X. Luo, J. L. Drewniak, T. P. Van Doren and T. Anderson, "Lump-element sections for modeling coupling between high-speed digital and I/O lines," *IEEE Int. Symp. Electromagnetic Compatibility*, pp. 260-265, Aug. 1997.

[25] M. Tanaka, W. Cui, X. Luo, J. L. Drewniak, T. H. Hubing, T. P. VanDoren and R. E. DuBroff, "FDTD Modeling of EMI Antennas," *IEEE Int. Symp. Electromagnetic Compatibility*, pp. 560-563, May 1999.

[26] T. Granberg, *Handbook of digital techniques for high-speed design; design examples, signaling and memory technologies, fiber optics, modeling and simulation to ensure signal integrity*. Prentice Hall, 2004.

[27] S. C. Thierauf, *High-speed circuit board signal integrity*. Artech House, 2004.

[28] E. Bogatin, *Signal integrity: simplified*. Prentice Hall, 2004.

[29] D. Brooks, *Signal integrity issues and printed circuit board design*. Prentice Hall, 2003.

[30] Y.-H. Lin and T.-L. Wu, "Analysis of radiation caused by SSN and transmission line by combining the equivalent circuits of active IC into FDTD," *IEEE Int. Symp. Electromagnetic Compatibility*, Vol. 1, pp. 277-282, Aug. 2004.

[31] E. Kurzweil, M. Lallement, R. Blanc and R. Pasquinelli, "Catch the ground bounce before it hits your system," *Int. Test Conference*, pp. 574-584, Oct. 1993.

[32] R. G. Kaires, "The mythology of ground bounce," *IEEE Int. Symp. Electromagnetic Compatibility*, Vol. 1, pp. 405-410, Aug. 1999.

[33] A. Zenteno, V. H. Champac, M. Renovell and F. Azais, "Analysis and attenuation proposal in ground bounce," *Asian Test Symposium*, pp. 460-463, Nov. 2004.

[34] S. W. Leung, L. Wan and C. M. Ip, "Modeling of the ground bounce effect on PCBs for high speed digital circuits," *IEEE Int. Symp. Electromagnetic Compatibility*, Vol. 1, pp. 110-115, Aug. 1999.

[35] S. W. Leung, L. C. Fung & L. Wan, "A mathematical model for ground voltage fluctuation in PCBs," *Asia-Pacific Conf. Environmental Electromagnetics*, pp. 100-104, May 2000.

[36] F. Y. Yuan, "Analysis of power/ground noises and decoupling capacitors in printed circuit board systems," *IEEE Int. Symp. Electromagnetic Compatibility*, pp. 425-430, Aug. 1997.

[37] F. Y. Yuan, T. K. Postel and L. M. Rubin, "Analysis and modelling of power distribution networks and plane structures in multichip modules and PCB's," *IEEE Int. Symp. Electromagnetic Compatibility*, pp. 447-452, Aug. 1995.

[38] A. Nishizawa, M. Shimazaki and S. Tanabe, "Ground bouncing analysis using a program linking FDTD and SPICE," *IEEE Int. Symp. Electromagnetic Compatibility*, pp. 381-384, May 1999.

[39] P. Heydari and M. Pedram, "Analysis and optimization of ground bounce in digital CMOS circuits," *Int. Conf. Computer Design*, pp. 121-126, Sep. 2000.

[40] P. Heydari and M. Pedram, "Ground bounce in digital VLSI circuits," *IEEE Trans. VLSI Syst.*, Vol. 11, No. 2, pp. 180–193, Apr. 2003.

[41] C.-K. Cheng, J. Lillis, S. Lin and N. H. Chang, *Interconnect analysis and synthesis*. John Wiley & Sons, 2000.

[42] M. Celik, L. Pileggi and A. Odabasioglu, *IC interconnect analysis*. Kluwer Academic Publishers, 2002.

[43] H. W. Johnson and M. Graham, *High speed digital design: a handbook of black magic*. Prentice Hall, 1993.

[44] B. Bhat and S. K. Koul, *Stripline-like transmission lines for microwave integrated circuits*. Wiley Eastern Limited, 1989.

[45] J. A. B. Faria, *Multiconductor transmission-line structures: modal analysis techniques*. John Wiley & Sons, 1993.

[46] P. Grivet, *The physics of transmission lines at high and very high frequencies*. Academic Press, 1970.

[47] D. M. Pozar, *Microwave engineering*, 2nd ed., John Wiley & Sons, 1998.

[48] R. E. Collin, *Foundations for microwave engineering*. McGraw-Hill, 1992.

[49] X. Shi, J.-G. Ma, K. S. Yeo, M. A. Do and E. Li, "Equivalent circuit model of on-wafer CMOS interconnects for RFICs," *IEEE Trans. Very Large Scale Integr. Syst.*, Vol. 13, No. 9, pp. 1060-1071, Sep. 2005.

[50] X. Shi, J.-G. Ma, B. H. Ong, K. S. Yeo, M. A. Do and E. Li, "RF equivalent-circuit model of interconnect bends based on S-parameter

measurements," *Microw. Opt. Technol. Lett.*, Vol. 45, No. 2, pp. 170-173, Apr. 2005.

[51] T. R. Chandrupatla and A. D. Belegundu, *Introduction to finite elements in engineering*, 2nd ed., Prentice Hall, 1997.

[52] J. M. Jin, *The finite element method in electromagnetics*. John Wiley & Sons, 1993.

[53] D. M. Sullivan, *Electromagnetic simulation using the FDTD method*. Wiley-IEEE Press, 2000.

[54] A. Taflove, *Computational electrodynamics: The finite-difference time-domain method*. Artech House, 1995.

[55] S. M. Rao, *Time domain electromagnetics*. Academic Press, 1999.

[56] R. Holland, V. P. Cable and L. C. Wilson, "Finite-volume time-domain (FVTD) techniques for EM scattering," *IEEE Trans. Electromagnetic Compatibility*, Vol. 33, No. 4, pp. 281-294, Nov. 1991.

[57] R. F. Harrington, *Field computation by moment methods*. 2nd ed., IEEE Press, 1993.

[58] J. Moore and R. Pizer, *Moment methods in electromagnetics: techniques and applications*. John Wiley & Sons, 1984.

[59] A. E. Ruehli, "Equivalent circuit models for three-dimensional multiconductor systems," *IEEE Trans. Microw. Theory & Techn.*, Vol. 22, No. 3, pp. 216-221, Mar. 1974.

[60] H. Heeb and A. E. Ruehli, "Retarded models for PC board interconnects – or how the speed of light affects our SPICE circuit simulation," *IEEE Int. Conf. Computer Aided Simulation*, pp. 70-73, Nov. 1991.

[61] A. E. Ruehli and H. Heeb, "Circuit models for three-dimensional geometrices including dielectrics," *IEEE Trans. Microw. Theory & Techn.*, Vol. 40, No. 7, pp. 1507-1516, Jul. 1992.

[62] H. Heeb and A. E. Ruehli, "Three-dimensional interconnect analysis using partial element equivalent circuits," *IEEE Trans. Circuit & Syst. – 1*, Vol. 39, No. 11, pp. 974-982, Nov. 1992.

[63] Y. Cao, Z.-F. Li, Ji-Feng Mao and Jun-Fa Mao, "A PEEC with a new capacitance model for circuit simulation of interconnects and packaging structures," *IEEE Trans. Microw. Theory & Techn.*, Vol. 48, No. 2, pp. 281-287, Feb. 2000.

[64] S. A. Teo, B. L. Ooi, S. T. Chew and M. S. Leong, "A fast PEEC technique for full-wave parameters extraction of distributed elements," *IEEE Microw. & Wireless Components Letters*, Vol. 11, No. 5, pp. 226-228, May 2001.

[65] K. M. Coperich, A. E. Ruehli and A. Cangellaris, "Enhanced skin effect for partial element equivalent circuit (PEEC) models," *IEEE Electrical Performance of Electronic Packaging*, pp. 189-192, Oct. 1999.

[66] A. E. Ruehli, G. Antonini, J. Esch, J. Ekman, A. Mayo and A. Orlandi, "Nonorthogonal PEEC formulation for time- and frequency-domain EM circuit modeling," *IEEE Trans. Electromagnetic Compatibility*, Vol. 45, No. 2, pp. 167-176, May 2003.

[67] G. Antonini, A. E. Ruehli and A. Haridass, "Including dispersive dielectric in PEEC models," *IEEE Electrical Performance of Electronic Packaging*, pp. 349-252, Oct. 2003.

[68] D. Gope, A. E. Ruehli, C. Yang and V. Jandhyala, "(S) PEEC: Time- and frequency-domain surface formulation for modeling conductors and

dielectric in combined circuit electromagnetic simulations," *IEEE Trans. Microw. Theory & Techn.*, Vol. 54, No. 6, pp. 2453-2464, Jun. 2006.

[69] M.-J. Tsai, F. De Flaviis, O. Fordham and N. G. Alexopoulos, "Modeling planar arbitrarily shaped microstrip elements in multilayered media," *IEEE Trans. Microw. Theory & Techn.*, Vol. 45, No. 3, pp. 330-337, Mar. 1997.

[70] G. Dural and M. I. Aksun, "Closed-form Green's functions for general sources and stratified media," *IEEE Trans. Microw. Theory & Techn.*, Vol. 43, No. 7, pp. 1545-1552, Jul. 1995.

[71] Y. L. Chow, J. J. Yang, D. G. Fang and G. E. Howard, "A closed-form spatial Green's function for the thick microstrip substrate," *IEEE Trans. Microw. Theory & Techn.*, Vol. 39, No. 3, pp. 588-592, Mar. 1991.

[72] J. R. Mosig, "Arbitrary shaped microstrip structures and their analysis with a mixed potential integral equation," *IEEE Trans. Microw. Theory & Techn.*, Vol. 36, No. 2, pp. 314-323, Feb. 1988.

[73] I. Park, R. Mittra and M. I. Aksun, "Numerically efficient analysis of planar microstrip configurations using closed-form Green's functions," *IEEE Trans. Microw. Theory & Techn.*, Vol. 43, No. 2, pp. 394-400, Feb. 1995.

[74] F. Ling, D. Jiao and J.-M. Jin, "Efficient electromagnetic modeling of microstrip structures in multilayer media," *IEEE Trans. Microw. Theory & Techn.*, Vol. 47, No. 9, pp. 1810-1818, Sep. 1999.

[75] M. I. Aksun, "A robust approach for the derivation of closed-form Green's functions," *IEEE Trans. Microw. Theory & Techn.*, Vol. 44, No. 5, pp. 651-658, May 1996.

[76] K. Y. See and E. M. Freeman, "Rigorous approach to modeling electromagnetic radiation from finite-size printed circuit structures," *IEE Proc., Microw. Antennas Propag.*, Vol. 146, No. 1, pp. 29-34, Feb. 1999.

[77] K. Y. See, "Modelling electromagnetic radiation from finite-size printed circuit boards", *Thesis submitted for the Degree of Doctor of Philosophy of the University of London and for the Diploma of Imperial College*. Oct. 1997.

[78] R. F. Harrington, *Time-harmonic electromagnetic field*. McGraw-Hill, 1961.

[79] C. A. Balanis, *Advanced engineering electromagnetics*. John Wiley & Sons, 1989.

[80] E. K. Miller, *Computational electromagnetics: frequency-domain method of moments*. IEEE Press, 1992.

[81] A. R. Hall, *Generalized method of moments*. Oxford University Press, 2005.

[82] A. F. Peterson, S. L. Ray and R. Mittra, *Computational methods for electromagnetics*. IEEE Press, 1998.

[83] J. Yeo and R. Mittra, "An algorithm for interpolating the frequency variations of method-of-moments matrices arising in the analysis of planar microstrip structures," *IEEE Trans. Microw. Theory & Techn.*, Vol. 51, No. 3, pp. 1018-1025, Mar. 2003.

[84] K. L. Virga, and R.-S. Yahya, "Efficient wide-band evaluation of mobile communications antennas using [Z] or [Y] matrix interpolation with the method of moments," *IEEE Trans. Antennas Propag.*, Vol. 47, No. 1, pp. 65-76, Jan. 1999.

[85] B. J. Fasenfest, F. Capolino, D. R. Wilton, D. R. Jackson and N. J. Champagne, "A fast MoM solution for large arrays: Green's function

interpolation with FFT," *IEEE Antennas and Wireless Propag. Letter*, Vol. 3, pp. 161-164, 2004.

[86] E. A. Soliman, "Rapid frequency sweep technique for MoM planar solvers," *IEE Proc. Microw. Antennas Propag.*, Vol. 151, No. 4, pp. 277-282, Aug. 2004.

[87] E. A. Soliman, A. K. Abdelmageed and M. A. EL-Gamal, "Neural computation of the MoM matrix elements for planar configurations," *Int. J. of Electronics and Communications*, Vol. 56, No. 3, pp. 155-162, 2002.

[88] Y. Xiong, D. G. Fang and Q. J. Zhang, "Application of two-dimensional AWE algorithm in training neural networks," *3rd Int. Conf. On Microw. And Millimeter wave Tech. Proc.*, pp. 879-882, 2002.

[89] E. A. Soliman, H. B. Mohamed and K. N. Natalia, "Neural networks-method of moments (NN-MoM) for the efficient filling of the coupling matrix," *IEEE Trans. Antennas Propag.*, Vol. 52, No. 6, pp. 1521-1529, Jun. 2004.

[90] L. Tarricone, M. Mongiardo and F. Cervelli, "A quasi one-dimensional integration technique for the analysis of planar microstrip circuits via MPIE/MoM," *IEEE Trans. Microw. Theory & Techn.*, Vol. 49, No. 3, pp. 517-523, Mar. 2001.

[91] J. R. Smith and M. S. Mirotznik, "Analytical simplification of the 2-D method of moments impedance integral," *IEEE Trans. Antennas Propag.*, Vol. 52, No. 12, pp. 3288-3294, Dec. 2004.

[92] J. R. Smith and M. S. Mirotznik, "Moments via integral transform method for 2-D dielectric materials," *IEEE Trans. Antennas Propag.*, Vol. 53, No. 1, pp. 560-563, Jan. 2005.

[93] K. Mahadevan and H. A. Auda, "Electromagnetic field of a rectangular patch of uniform and linear distributions of current," *IEEE Trans. Antennas Propag.*, Vol. 37, No. 12, pp. 1503-1509, Dec. 1989.

[94] L. Alatan, M. I. Aksun, K. Mahadevan and M. T. Birand, "Analytical evaluation of the MoM matrix elements," *IEEE Trans. Microw. Theory & Techn.*, Vol. 44, No. 4, pp. 519-525, Apr. 1996.

[95] F. Andrew and T. A. Arlon, "Matrix methods for microstrip three-dimensional problems," *IEEE Trans. Microw. Theory & Techn.*, Vol. 20, No. 8, pp. 497-504, Aug. 1972.

[96] A.W. Glisson and D. R. Wilton, "Simple and efficient numerical methods for problems of electromagnetic radiation and scattering from surfaces," *IEEE Trans. Antennas Propag.*, Vol. 28, No. 5, pp. 593-603, Sep. 1980.

[97] B. J. Rubin and S. Daijavad, "Radiation and scattering from structures involving finite-size dielectric regions," *IEEE Trans. Antennas Propag.*, Vol. 38, No. 11, pp. 1863-1873, Nov. 1990.

[98] P. Petre, M. Swaminathan, L. Zombory, T. K. Sarkar and S. Daijavad, "Volume/surface formulation for analyzing scattering from coated periodic strips," *IEEE Trans. Antennas Propag.*, Vol. 42, No. 1, pp. 119-122, Jan. 1994.

[99] R. L. Burden and J. D. Faires, *Numerical analysis*, 4th ed., PWS-Kent, 1989.

[100] S. C. Chapra and R. P. Canale, *Numerical methods for engineers with programming and software applications*, 3rd ed., McGraw-Hill, 1998.

[101] J. N. Shadid and R. S. Tuminaro, "A comparison of preconditioned nonsymmetric Krylov methods on a large-scale MIMD machine," *SIAM J. Sci. Comput.*, Vol. 15, No. 2, pp. 440-459, Mar. 1994.

[102] P. Sonneveld, "CGS, A fast Lanczos-type solver for nonsymmetric linear systems," *SIAM J. Sci. Stat. Comput.*, Vol. 10, No. 1, pp. 36-52, Jan. 1989.

[103] H. A. V. D. Vorst, "Bi-CGSTAB - A fast and smoothly converging variant of Bi-CG for the solution of nonsymmetric linear systems," *SIAM J. Sci. Stat. Comput.*, Vol. 13, No. 2, pp. 631-644, Mar. 1992.

[104] Y. Saad and M. H. Schultz, "GMRES - A generalized minimal residual algorithm for solving nonsymmetric linear systems," *SIAM J. Sci. Stat. Comput.*, Vol. 7, No. 3, pp. 856-869, Jul. 1986.

[105] http://www.ansoft.com/